Particle image velocimetry/ tracking in turbulent flow over riblet surfaces with superhydrophobic coating

by

Jianfeng Hou

A thesis submitted in partial fulfillment of the requirements for the degree of

Master of Science

Department of Mechanical Engineering
University of Alberta

Abstract

Riblet surfaces have been introduced as of one successful technique to reduce skin-friction. Advanced particle image velocimetry (PIV) and particle tracking velocimetry (PTV) are employed to investigate turbulent structures over riblet surfaces by several researchers including Suzuki and Kasagi (1994), Lee and Lee (2001) and Sasamori et al. (2014). However, a complete characterization of turbulent statistics including mean velocity, and three components of turbulence intensities and vorticities over riblet surfaces is still missing due to difficulties in measurement of small-scale near-wall turbulence.

The capabilities of the planar and volumetric PIV and PTV in capturing three dimensional structures of the turbulent flow over a riblet surface with the groove spacing of 750 μm ($s^+ = 11$) has been investigated at $Re_\tau = 147$. The two-dimensional measurements are carried out using the planar PIV and high-magnification long-range micro-PTV. The three-dimensional techniques include tomographic-PIV (tomo-PIV) and 3D-PTV which were carried out at high tracer density of 0.02 particle per pixel (ppp). Measurements over the riblet surface are evaluated in comparison with the measurements over a smooth surface, direct numerical simulation (DNS) of the turbulent flow in a smooth channel at $Re_\tau = 150$, and previous investigations of turbulent statistics over riblet surfaces. Reduction of skin-friction is calculated to be 6.1% and 7.5% from the velocity profiles in the linear viscous sublayer from 2D-PTV and profiles of the Reynolds stress from 2D-PIV, respectively. Reductions of the maximum streamwise, wall-normal and spanwise turbulence intensity are characterized to be 5.9%, 9.4% and 9.4%, respectively, over the riblet surface from 2D-PIV and 3D-PTV compared to those on the smooth surface. Three components of the fluctuating vorticity over the riblet surface measured by a tomo-PIV are first shown in experimental riblet study but no changes are spotted compared to the vorticities in the

smooth surface case.

As a relatively new skin-friction reduction (SFR) technique, superhydrphobic surfaces (SHSs) are capable of reducing skin-friction by entrainment of air pockets in the surface. Improvement of SFR over riblet surfaces are expected when the surfaces with riblets are coated with superhydrophobic layers. However, with only two studies by Barbier, Jenner, and D'Urso (2012) and Prince, Maynes, and Crockett (2014) in the area, it needs more detailed investigation if the SHSs are able to help riblets achieve additional SFR.

The effect of riblets combined with superhydrophobic coating on skin-friction is studied by means of a planar PIV at $Re_\tau = 141$. The evaluation was acquired by comparing results between riblet surfaces with and without superhydrophobic coatings. The wall-normal turbulence intensities and the Reynolds shear stress over the coated smooth surface are both reduced by about 5% compared to the smooth surface, indicating the SFR. The analysis of the longevity of the SHS over the smooth surface reveals the loss of SHS in around 500 seconds. The riblet surfaces at $s^+ = 8.5$ and 17 are proven to reduce skin-friction while the riblet surface at $s^+ = 34$ increases skin-friction. After coating, the riblet surface show limited SFR benefit but the longevity analysis shows that SHSs survive longer as a result of being well protected by the riblets. No SFR is observed since negligible changes of Reynolds shear stresses and mean velocity profiles are noticed after coating the surfaces with riblet at $s^+ = 8.5$ and $s^+ = 17$. The riblet surface with $s^+ = 34$ shows suppression of Reynolds shear stress, reduction of streamwise turbulence intensities, and increase of mean velocity in the near wall region after being coated by a superhydrophobic layer, which indicate the occurrence of SFR in this case.

Preface

The work in this thesis was carried out by me under the supervision of Dr. Sina Ghaemi and Dr. Brian Fleck from Department of Mechanical Engineering, University of Alberta.

The experimental setup in section 3.1 was developed by Babak Vajdi Hokmabad (MSc student at the time). I developed the experimental setup in chapter 3.2. I carried out all the measurements over riblet surfaces in section 3.1 and 3.2.

In Chapter 4 and Chapter 5, PIV and PTV processing and data analysis were conceived by me under the supervision of Dr. Sina Ghaemi. The interpretation and discussion of the results was developed by me under supervision of Dr. Sina Ghaemi.

Acknowledgement

I would like to express my sincere gratitude to my supervisors Dr. Brain Fleck and Dr. Sina Ghaemi for their generous support and guidance during my study.

I am thankful to Dr. Fleck for giving me the valuable chance to start my career as a graduate student. He has been such a wonderful mentor not only because of his rich academic experiences but also his life wisdom.

I am grateful to Dr. Ghaemi for his thoughtful supervision. His passion for science and dedication to work deeply influence me. His outstanding skills and great patience guide me throughout my graduate study.

Many thanks to Jiaxin Zhu and Pallavi Bhambri for making my academic life enjoyable. Without the unconditional help of Babak Vajdi Hokmabad, Sina Rafati and Wagih Abu Rowin, I couldn't finish my thesis works smoothly. Thanks to everyone for making the groups warm families where I never feel alone.

In the end, I would like to express my great appreciation to my parents for their endless love and support. Their trust makes me confident in the walk of life.

Table of Contents

List of Figures

List of Tables

Chapter 1. Introduction

The wall-normal momentum transport in turbulent flows causes large skin-friction and results in more energy consumption in many applications including pipelines, marines and aerospace engineering. SFR techniques are of interest since they help increase energy efficiency and improve performance. Passive methods like polymer additives (Warholic, Massah, and Hanratty 1999; White and Mungal 2008), riblets (Walsh 1983; Walsh and Lindemann 1984), microbubbles (McCormick and Bhattacharyya 1973), and superhydrophobic surfaces Daniello, Waterhouse, and Rothstein (2009) have been explored and proved to provide SFR under certain conditions.

Riblets are microgrooves aligned in the streamwise direction (Walsh and Weinstein 1978; Walsh 1983) and were reported to reduce skin-friction in turbulent flows by Walsh (1983). In addition to the investigations on optimization of the riblet geometry, the effect of riblets on turbulent structures is of fundamental interest. The investigations have been aided by different measurement techniques over the last few decades. Park and Wallace (1994) observed a decrease of wall shear stress over riblet surfaces and recorded reduced root-mean-square streamwise turbulence intensity in the riblet valley using hot-wire anemometry. With laser Doppler anemometry, Djenidi and Antonia (1996) noticed weaker motions of quasi-streamwise vortices over riblet surface. However, limited by the single-point measurement, these two techniques were not able to fully characterize the instantaneous flow field.

Numerical investigations have generated detailed information about the characteristics of the flow fields over riblets that can rarely be obtained from experiments. For example, the DNS of Choi, Moin, and Kim (1993), Goldstein, Handler, and Sirovich (1995) and El-Samni, Chun, and Yoon (2007) have provided detailed descriptions of mechanisms of SFR over riblets based on near wall turbulent statistics and on the characterization of coherent structures. It is still challenging to extend the numerical simulations to higher Reynolds numbers and to surfaces with micro-size or random texture. Investigation of turbulent flows over these surfaces still relies on experimental techniques.

Advanced PIV and PTV allow access to instantaneous three-dimensional turbulent flow fields. However, even with PIV and PTV, measurement of three-dimensional near-wall turbulent statistics over riblets is challenging due to several factors including large velocity gradients, presence of the solid surface, and the relatively small size of the riblets and flow structures. Lee and Lee (2001), Lee and Choi (2008) and Sasamori et al. (2014) have characterized changes over riblets with 2D-PIV, but the focuses were on the ability of riblets to reduce skin-friction. Though a relatively complete set of turbulent analysis are available in 3D-PTV work by Suzuki and Kasagi (1994), the evaluation of the measurement accuracy was not investigated and the vorticity information were absent. This thesis will evaluate the performance of two-dimensional and three-dimensional PIV and PTV in characterization of turbulent structures over millimeter-size riblets by comparing the observations with the literature.

Recent investigations have aimed at improvement of the SFR performance of riblets by combining this technique with superhydrophobicity. SHSs are inspired by the water repellent properties of the lotus leaf (Barthlott and Neinhuis 1997). They are coated with micro and nano structures with which the surface contact angle is larger than 150°. The air pockets trapped between the rough tips of the SHS generate shear free regions at the air-water-interface and slip condition for the liquid (Rothstein 2010). Many experimental (Woolford et al. 2009), numerical (Min and Kim 2004), and theoretical Fukagata, Kasagi, and Koumoutsakos (2006) studies over SHSs have reported that skin-friction and turbulence intensities reduce with streamwise slip. Barbier, Jenner, and D'Urso (2012) and Prince, Maynes, and Crockett (2014) fabricated surfaces with riblets and superhydrophobic layers. They measured the SFR by recording the change of torque on a cone-and-plate rheometer (Barbier, Jenner, and D'Urso 2012) and change of pressure drop (Prince, Maynes, and Crockett 2014), but the studies are not able to shed light on the reasons behind the changes. This thesis contains experimental investigation of surfaces containing both riblets and superhyophobicity to evaluate how the SHS can benefit the SFR ability of riblets.

The thesis is organized as following:

Chapter 2: Basic concepts and background are provided in this chapter. It starts with introducing the fundamental equations governing turbulent channel flows and coherent structures that are in close relation with skin-friction. Several SFR techniques are introduced, with focuses on riblet

and SHS. The last section presents the principle of measurement techniques including two-dimensional and three-dimensional PIV and PTV.

Chapter 3: The chapter describes experimental setups including the flow facility, fabrication of the test surfaces, and details of the applied measurement methodology for the two measurement campaigns of this thesis.

Chapter 4: The capabilities of planar and volumetric PIV and PTV are evaluated by investigating the turbulent flow over a riblet surface in this chapter. The evaluation is mainly based on the velocity profiles in the linear sublayer, Reynolds stresses and three components of fluctuating vorticity.

Chapter 5: The turbulent structures over riblet surfaces and riblet surfaces coated with SHS are investigated. The variations in Reynolds shear stress are used to observe the SFR performances. Two-point correlations, quadrant analysis and convergence plots of turbulence intensities are employed to scrutinize the mechanism behind the changes.

Chapter 6: This chapter provides conclusions for the studies explained before and recommendations for future works.

Chapter 2. Literature review

2.1 Turbulent Channel flow

Channel flow is a prevalent category of turbulent wall flows. Because of the geometric simplicity of channel flow, many experimental and numerical studies are carried out over it to investigate complex near-wall turbulent interactions (Kim, Moin, and Moser 1987).

2.1.1 Fundamentals

The basic principles of turbulent channel flow are introduced here based on (Pope 2000). The channel is a long rectangular duct with dimension of L, H (= 2δ), and W for length, height and width, respectively. Cartesian coordinate systems are defined as x (streamwise), y (wall-normal) and z (spanwise), as shown in Figure 2.1. Instantaneous velocities along x, y, and z are U, V and W, respectively. Taking the Reynolds decomposition, velocity fluctuations u, v and w are defined as

$$u = U - \langle U \rangle, \tag{2.1}$$

where $\langle U \rangle$ is the ensemble average velocity.

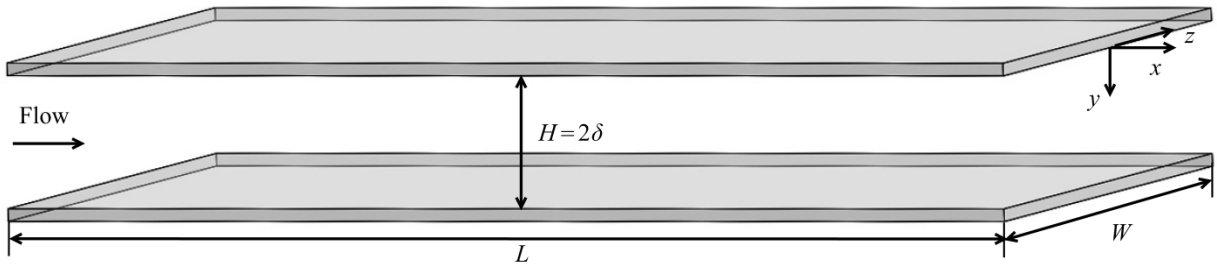

Figure 2.1. Configuration of the turbulent channel flow showing the main dimensions and the coordinate system.

The channel is long (L / H >> 1) with the fluid flow primarily in the axial direction. The aspect ratio is also large (W / H >> 1) so the flow is statistically independent of z. In the fully developed region, flow is considered to be statistically one dimensional, which means velocity statistics no longer change with x. The characteristic Reynolds number of the flow is

$$Re = \frac{\rho U_b H}{\mu}, \tag{2.2}$$

where U_b is the average velocity across the channel, ρ is the fluid density, and μ the dynamic viscosity. Turbulent flow free of transitional effect occurs when $Re \sim 3000$.

The mass conservation equation for an incompressible fluid is given by

$$\frac{\partial <U>}{\partial x} + \frac{\partial <V>}{\partial y} + \frac{\partial <W>}{\partial z} = 0. \tag{2.3}$$

By considering that

$$\frac{\partial <U>}{\partial x} = 0 \text{ and } <W> = 0 \tag{2.4}$$

in the channel, the mean continuity equation becomes

$$<V> = 0. \tag{2.5}$$

The wall-normal momentum equation is adopted as

$$\begin{aligned} &\rho\left(\frac{\partial <V>}{\partial t} + <U>\frac{\partial <V>}{\partial x} + <V>\frac{\partial <V>}{\partial y} + <W>\frac{\partial <V>}{\partial z}\right) \\ &= -\frac{\partial <P>}{\partial y} - \rho\frac{\partial <uv>}{\partial x} - \rho\frac{\partial <v^2>}{\partial y} - \rho\frac{\partial <vw>}{\partial z} + \mu\left(\frac{\partial^2 <V>}{\partial x^2} + \frac{\partial^2 <V>}{\partial y^2} + \frac{\partial^2 <V>}{\partial z^2}\right), \end{aligned} \tag{2.6}$$

where P is the local pressure. In a fully developed turbulent channel flow, it can be reduced to

$$-\rho\frac{\partial <v^2>}{\partial y} - \frac{\partial <P>}{\partial y} = 0. \tag{2.7}$$

After integration with the boundary condition of $<v^2>_{y=0} = 0$, Equation (2.7) transfers to

$$<v^2> + \frac{<P>}{\rho} = \frac{P_w(x)}{\rho} \text{ and} \tag{2.8}$$

$$\frac{\partial <P>}{\partial x} = \frac{dP_w}{dx}, \tag{2.9}$$

where P_w is the mean pressure on the wall.

At the same time, the streamwise momentum equation is

$$\rho\left(\frac{\partial \langle U \rangle}{\partial t} + \langle U \rangle \frac{\partial \langle U \rangle}{\partial x} + \langle V \rangle \frac{\partial \langle U \rangle}{\partial y} + \langle W \rangle \frac{\partial \langle U \rangle}{\partial z}\right)$$
$$= -\frac{\partial \langle P \rangle}{\partial x} - \rho \frac{\partial \langle u^2 \rangle}{\partial x} - \rho \frac{\partial \langle uv \rangle}{\partial y} - \rho \frac{\partial \langle uw \rangle}{\partial z} + \mu\left(\frac{\partial^2 \langle U \rangle}{\partial x^2} + \frac{\partial^2 \langle U \rangle}{\partial y^2} + \frac{\partial^2 \langle U \rangle}{\partial z^2}\right), \tag{2.10}$$

which simplifies to

$$-\frac{\partial \langle P \rangle}{\partial x} - \rho \frac{\partial \langle uv \rangle}{\partial y} + \mu \frac{\partial^2 \langle U \rangle}{\partial y^2} = 0. \tag{2.11}$$

If the total shear stress is defined as the sum of viscous stress and Reynolds shear stress

$$\tau = \mu \frac{d\langle U \rangle}{dy} - \rho \langle uv \rangle, \tag{2.12}$$

then the momentum equation can further be written as

$$\frac{d\tau}{dy} = \frac{dP_w}{dx}. \tag{2.13}$$

At the wall, $\rho\langle uv \rangle = 0$ so only the viscous stress exists as wall shear stress

$$\tau_w = \mu \frac{d\langle U \rangle}{dy}. \tag{2.14}$$

The fractional contribution of viscous stress to the total shear stress is 100% at the wall and drops to 50% at $y^+ = 12$ then less than 10% above $y^+ = 50$ (Pope 2000). The Reynolds shear stress is shown in Figure 2.2, with the straight line denoting the ratio between the total shear stress and the wall shear stress. Reynolds shear stress is zero at the wall but its contribution increases relative to the total shear stress away from the wall.

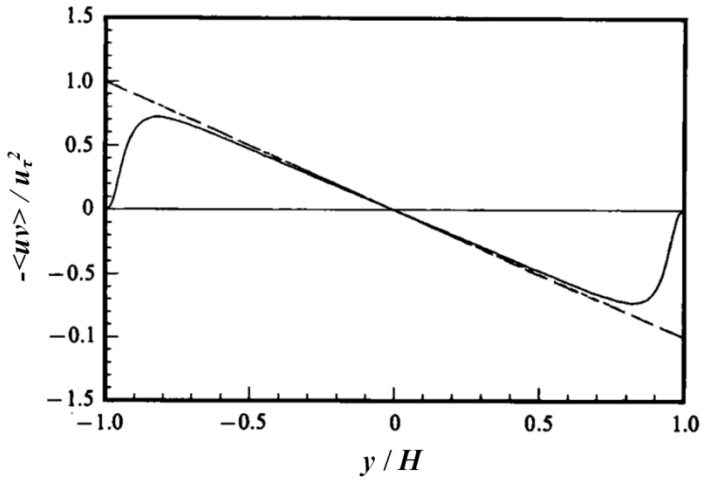

Figure 2.2. — Reynolds shear stress normalized by the wall shear velocity, ---- total shear stress for fully developed channel normalized by the wall shear velocity at Re = 6,600 (Kim, Moin, and Moser 1987).

According to such shear stress distribution profile, turbulent channel flow is divided into a viscous wall region ($y^+ < 50$) and an outer layer ($y^+ > 50$).

At the region very close to the wall, viscosity and wall shear stress are important parameters. Friction velocity and wall units are defined based on these two parameters, to represent the inner scales in this region as

$$u_\tau = \sqrt{\frac{\tau_w}{\rho}} \text{ and} \tag{2.15}$$

$$\delta_v = \frac{v}{u_\tau}, \tag{2.16}$$

where v is kinematic viscosity.

With these two scales, the velocity and the distance from the wall are expressed as dimensionless parameters of

$$u^+ = \frac{\langle U \rangle}{u_\tau} \text{ and} \tag{2.17}$$

$$y^+ = \frac{y}{\delta_v}, \tag{2.18}$$

respectively. Based on the inner scales, friction Reynolds number is given by:

$$Re_\tau = \frac{u_\tau \delta}{\nu}, \tag{2.19}$$

where δ is half channel height.

$\frac{d<U>}{dy}$ is a dynamically important parameter that determines both the viscous stress and turbulent production. Therefore, it is chosen to describe the mean velocity profile. $\frac{d<U>}{dy}$ is a function of the characteristic scales of different regions expressed to be

$$\frac{d<U>}{dy} = \frac{u_\tau}{y} F(\frac{y}{\delta_v}, \frac{y}{\delta}), \tag{2.20}$$

in which F is a universal non-dimensional function consisting of the length scale in either viscous wall region or outer layer.

At high Reynolds number, there is an inner layer ($y / \delta < 0.1$) close to the wall where the mean velocity profile is dominated by the viscous scale, thus Equation (2.20) can be simplified as

$$\frac{d<U>}{dy} = \frac{u_\tau}{y} F_1(\frac{y}{\delta_v}). \tag{2.21}$$

where F_1 is the part of F that is applicable to region dominated by the viscous scale.

Replaced with u^+ and y^+, the integral of Equation (2.21) is

$$u^+ = \int_0^{y^+} \frac{1}{y'} F_1(y')\, dy'. \tag{2.22}$$

where y' is the dummy variable of y^+. The no-slip condition at wall gives

$$f_w(0) = 0. \tag{2.23}$$

Also from the wall shear stress equation, there are

$$\tau_w = \rho\nu \left(\frac{d<U>}{dy}\right)|_{y=0} = \rho u_\tau^2 \text{ and} \tag{2.24}$$

$$\frac{d<U>/u_\tau}{u_\tau dy/\nu} = \frac{du^+}{dy^+} = 1. \tag{2.25}$$

At $y^+ < 5$, a departure of u^+ from the linear relation in Equation (2.25) is negligible. As a result, $y^+ < 5$ is defined as linear viscous sublayer governed by

$$u^+ = y^+. \tag{2.26}$$

Away from the inner layer, viscosity has little influence on the velocity profile, therefore

$$\frac{d<U>}{dy} = \frac{u_\tau}{y} F\left(\frac{y}{\delta}\right) = \frac{u_\tau}{y}\frac{1}{\kappa}, \tag{2.27}$$

where κ is a constant value named von Karman constant and is a geometric structural parameter depicting the angle of the ejection events in the log-layer.

After substitution by the inner scales and integration, Equation (2.27) will be

$$u^+ = \frac{1}{\kappa} ln y^+ + B, \tag{2.28}$$

where B is a constant. The κ and B are in 5% variation of

$$\kappa = 0.41,\ B = 5.2. \tag{2.29}$$

Equation 2.28 is the logarithmic law of the wall applied to the log-law region usually in the range of $y^+ > 30$ and $y / \delta < 0.3$. Between the viscous sublayer and log-law region, buffer layer as the transitional layer exists and is important in terms of turbulent energy production and dissipation.

Root-mean-square of turbulence intensities $<u^2>$, $<v^2>$ and $<w^2>$ are shown in Figure 2.3.

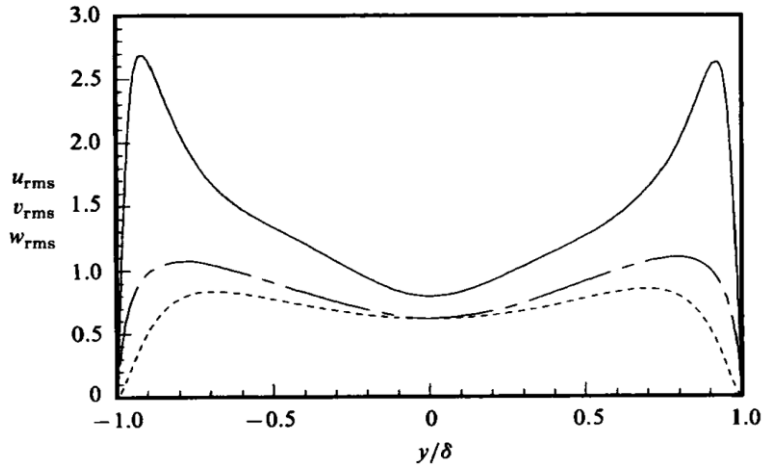

Figure 2.3. Root-mean-square velocity fluctuations normalized by the wall shear velocity: — u_{rms}, ---- v_{rms}, — - — w_{rms} (Kim, Moin, and Moser 1987).

2.1.2 Coherent structures

Coherent structures are three dimensional regions of space showing specific correlations between flow variables over a range of space or time (Fiedler 1988; Robinson 1991). These structures are responsible for maintaining production of turbulence with the cost of mean flow motions (Robinson 1991). Robinson (1991) suggested three major motivations for exploring coherent structures: (a) to help with development of turbulent modeling; (b) to explore new flow control strategies; (c) to learn about the phenomena behind the statistical properties of turbulence. Researchers are interested in kinematic properties of coherent structures such as size, shape and vorticity, and dynamic properties such as origin, stability and growth. At the very beginning, coherent structures were studied by experimental flow visualization studies and later explored in numerical simulations (Fazle Hussain 1986). In the literature, the most commonly discussed coherent motions of turbulent wall flows are high and low speed streaks, ejections and sweeps, and vortical structures including hairpin vortices and quasi-streamwise vortices.

High and low speed streak

The instantaneous velocity distribution in a turbulent wall flow is constituted of intermittent high and low speed streamwise streaks in the viscous sublayer up to log region (Smith and Metzler 1983). Low speed and high speed streaks are relative terms representing streamwise elongated meandering regions of positive ($u > 0$) or negative ($u < 0$) velocity fluctuations. Using the hydrogen bubble technique, Kline et al. (1967) observed the structure of low speed streaks in a turbulent boundary layer, as shown in Figure 2.4. With the same technique, Smith and Metzler (1983) noticed the mean spanwise distance between low speed streaks in low Reynolds number cases is constant and approximately 100 viscous lengths.

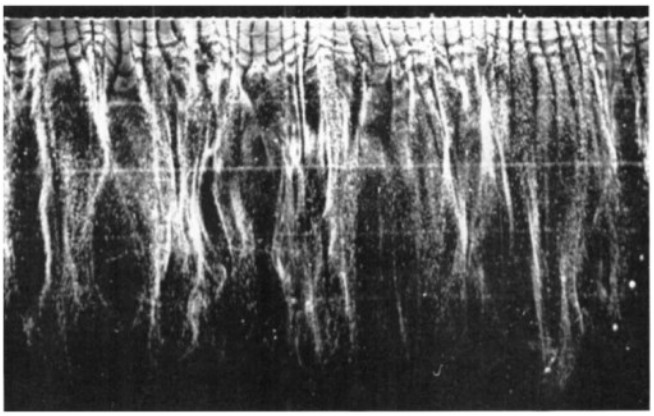

Figure 2.4. Photograph of the structure of a flat plate turbulent boundary layer at $y^+ = 2.7$ (Kline et al. 1967).

Ejection and sweep

Quadrant analysis provides detailed information of turbulence production sources from combination of positive and negative u and v fluctuations (Willmarth and Lu 1972). According to the sign, it is divided into four quadrants: Q1 ($u > 0$ and $v > 0$), Q2 ejection ($u < 0$ and $v > 0$), Q3 ($u < 0$ and $v < 0$) and Q4 sweep ($u > 0$ and $v < 0$). Parts of the low speed streaks lift up from the wall in the ejection phase, and then oscillate and breakdown. Following the ejection events, large scale high speed fluids flow towards the wall at small angles in sweep phase (Blackwelder and Eckelmann 1979). These two processes are taken as bursting phenomena associated with most of the turbulent energy production (Blackwelder and Eckelmann 1979). Ejection and sweep are major contributors to the Reynolds shear stress away from the wall and near the wall, respectively (Kim, Moin, and Moser 1987).

Vortical structures

Robinson (1991) defined a vortex as a circular or spiral pattern when viewed from a reference frame moving with the center of the vortex core. A quasi-streamwise vortex includes any vortical structure with predominantly streamwise direction (Robinson 1991). Their typical diameter is about 30 wall units (Kim, Moin, and Moser 1987). Jimenez (1992) analytically showed that skin-friction drag is proportional to the square of streamwise vorticity fluctuations at the wall. Geometries of horseshoe and hairpin vortices are shown in Figure 2.5. Horseshoe vortices are elongated at high Reynolds number and stretched to form hairpin vortices. Robinson (1991) introduced a model for low Reynolds number boundary layers where quasi-streamwise vortices dominate the buffer region and horseshoe vortices frequently show up in wake region. Quasi-streamwise vortices do not often appear as a pair but individually

(Guezennec, Piomelli, and Kim 1989). Arch or horseshoe vortices are not necessarily symmetric but may be one sided (Moin and Kim 1985). The generation mechanism of streamwise vortices is still an unsolved question. Mainly two categories have been considered: (a) production of new vortices by the induction of existing vortices; (b) formation of new vortices by instability of low speed streaks (Schoppa and Hussain 2002).

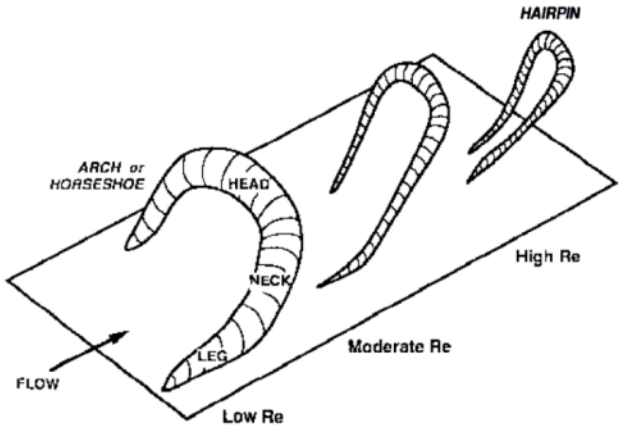

Figure 2.5. Geometry and nomenclature for arch- and hairpin-shaped vortical structures (Robinson 1991).

2.1.3 Means for reduction of skin-friction drag

Fluid drag includes pressure drag and skin-friction drag. Pressure or form drag arises because of the shape of the object and is related to moving fluids in front of an object to its back, e.g., most of the resistance felt when walking through a pool of water is pressure drag. To decrease pressure drag, the shape of the body needs to be streamlined. Skin-friction or viscous drag is from the friction between the object surface and the adjacent fluid layers. It is a function of fluid viscosity, velocity gradient, and surface area. Pressure drag is important for separated flows while skin-friction drag is essential to attached wall flows. Higher skin-friction in turbulence equates to more energy expenditure in transportation. For example, due to high skin-friction drag, flows in pipelines for the oil industry will require a large amount of pumping energy. Since Toms' (1948) accidental discovery of the skin-friction deduction with adding polymers in pipe and Savins' (1964) first use of the term drag reduction, extensive research has bloomed to uncover SFR techniques for the purpose of saving energy. In turbulent channel flow, SFR is usually expressed as SFR = $(\tau - \tau_0) / \tau_0$ in which τ is the skin-friction on surface with modified

texture aimed for SFR and τ_0 is the friction on the smooth surface exposed to the same flow condition. The basic ideas of the most popular SFR techniques are discussed below.

Polymer additives

The fact that skin-friction drag for turbulent flow in pipes and channels can be reduced by adding a certain amount of polymer has been known for about half a century (Den Toonder et al. 1997). Up to 70% SFR was observed by Warholic, Massah, and Hanratty (1999). The most plausible mechanism behind the phenomenon is that polymers possess the ability to store the elastic energy from the near wall region. When the relaxation time is long enough, the energy will be transported away from the buffer layer and released in the log layer, resulting in SFR (Min et al. 2003). There exists a threshold polymer concentration to trigger SFR. Once the value is reached, SFR will increase with the increase of polymer concentration until it reaches a maximum (Min et al. 2003).

Microbubbles

Microbubbles are usually produced by electrolysis and injected into the flow through porous medium to reduce skin-friction (Abdulbari et al. 2013). About 65% SFR was obtained by McCormick and Bhattacharyya (1973) with the use of hydrogen bubbles. Deutsch et al. (2004) achieved about 80% SFR with carbon dioxide bubbles. Due to the low cost and easy access, microbubble injection is popular in practical applications such as on ship hulls (Deutsch et al. 2004). Its SFR effect is determined by many characteristics including flow properties, bubble geometry, and bubble generating method. For example, it is proved that bubbles larger than 200 wall units provides no noticeable SFR (Pal, Merkle, and Deutsch 1988). The detailed mechanism of SFR using bubbles is still under investigation.

Riblets

Riblet surfaces were inspired by the texture of the shark skin. The scales of the shark skin have been replicated with surface microgrooves aligned in the streamwise direction (Walsh 1983). Riblets of different shapes lead to varied SFR. The SFR is also a function of the Reynolds number and riblet spacing. Traditional two dimensional riblets can bring up to 10% SFR (Bechert et al. 1997) and some novel three dimensional ones are able to produce about 20% reduction (Chen et al. 2014). Riblets impede the transverse motions near the wall

(Bechert and Bartenwerfer 1989). Especially, riblets alter the behavior of streamwise vortices so the vortices shift upward and enter regions with low shear (Jimenez 1992).

Dimples

Dimples on a surface is well known as a method for enforcing heat transfer but has also been investigated for SFR (Lienhart, Breuer, and Köksoy 2008; Abdulbari et al. 2013). Similar to riblets, dimples are surface modifications, but they are distributed discretely instead of continuously following the streamwise directions; dimples are shallow indentations rather than small protrusions above the wall (Abdulbari et al. 2013). Among dimple studies, there is much debate on whether dimples are able to reduce skin-friction because the outcome depends heavily on their shapes, arrangements and flow conditions. For example, (Kim, Moon, and Kim 2011) observed reduction of pressure loss while (Isaev, Leontiev, and Kudryavtsev 2005) noticed skin-friction increase.

Superhydrophobic surfaces

The idea of SHSs for SFR was inspired by the water repellent properties of the lotus leaf as a result of the hierarchical micro and nano structures on the leaf (Latthe et al. 2014). The air-water shear-free interface on SHS has the potential to reduce skin-friction drag (Daniello, Waterhouse, and Rothstein 2009). Tests in laminar channel flows over SHSs with ordered patterns have demonstrated significant slip velocity and pressure drop reductions (Ou and Rothstein 2005; Byun et al. 2008; Joseph et al. 2006). However, in the turbulent regime, inconsistent results from zero to about 75% SFR have been observed (Peguero and Breuer 2009, Woolford et al. 2009, Park, Sun, and Kim 2014). Such contradictions may be caused by depleted air pockets during tests, undocumented scale of surface roughness to the flow scale, and measurement uncertainties (Vajdi Hokmabad and Ghaemi 2016).

2.2 Riblet surfaces

Among the methods investigated for SFR, only a few have the potential to be applied in practice. Riblets are one of the simple passive SFR techniques that possess reliable performance. They are microgrooves etched on the wall surface aligned in streamwise directions to alter the structure of near wall turbulence (Walsh 1983; Bechert and Bartenwerfer 1989). Riblets have been proven to successfully reduce overall skin-friction of airfoils and pipelines. Sareen et al. (2014) conducted an experiment on a DU 96-W-180 airfoil covered by a riblet film at various Reynolds numbers. The optimum configuration produced up to 5% SFR. Weiss (1997) recorded the development of "scriblets" in the surface of high pressure natural gas pipeline surfaces in NOVA Gas Transmission. Scriblets share the same working mechanism with riblets though they are coarser and more irregular. A laboratory test by Weiss (1997) using the new pipes with scriblets gave at least 5% pressure drop reduction.

2.2.1 Reduction of skin-friction using riblets

Many investigations of riblet effects have suggested there is no SFR in laminar regimes (Choi, Moin, and Kim 1991, Chu and Karniadakis 1993). In turbulent flows, riblets are known to provide repeatable SFR. The performance of a riblet surface depends on the groove spacing relative to the scale of the near wall turbulence. According to Walsh and Lindemann (1984), the riblet SFR at different Reynolds numbers can be expressed in terms of dimensionless riblet spacing, $s^+ = s / (u_\tau / v)$ in which s is the lateral riblet tip spacing, v is the kinematic viscosity and u_τ is the friction velocity over the smooth surface. One of the earliest experimental works by Walsh (1979) indicated that SFR occurs only for $s^+ < 30$ and the maximum reduction is observed at $s^+ = 15$-20 for riblets with both sharp and curved shapes. Bechert et al. (1997) provided a thorough set of SFR measurements for riblets of various shapes, as shown in Figure 2.6. For sawtooth riblets, about 5% SFR was obtained when $s^+ \approx 17$ and tip angle $\alpha = 60^\circ$. Semi-circular scalloped riblets also reached 5% SFR when $h / s = 0.5$ and $s^+ \approx 17$. A record of 9.9% SFR was achieved by blade riblets with $t / s = 0.2$, $h / s = 0.5$ and $s^+ \approx 17$. Trapezoidal groove riblets are more durable compared to thin blade riblets and able to provide high SFR of 8.2% at $h / s = 0.5$, $\alpha = 60^\circ$ and $s^+ \approx 17$.

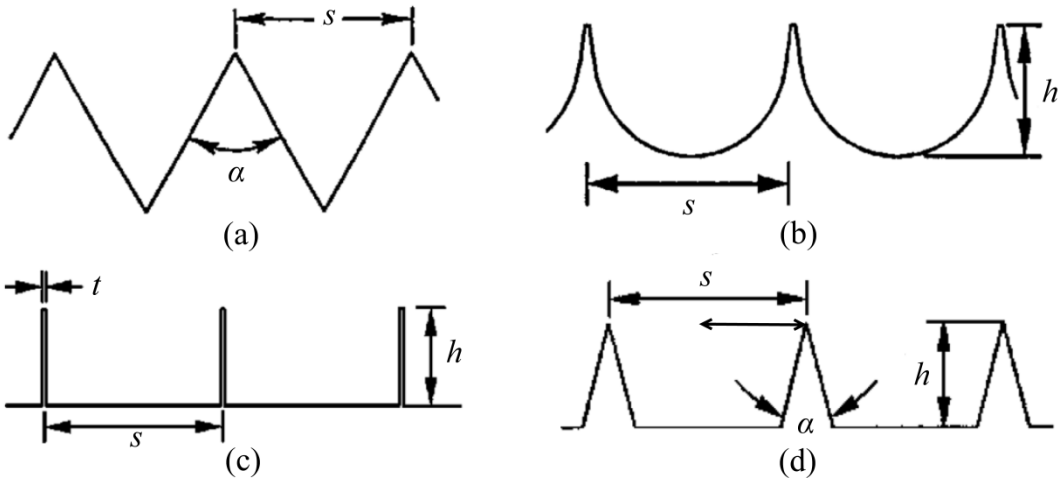

Figure 2.6. Typical shapes of riblet. (a) sawtooth, (b) semi-circular scalloped, (c) blade, (d) trapezoidal (Reproduced from Bechert et al. 1997).

Other than the optimum performances of each riblet, Bechert et al. (1997) concluded the general trends of SFR curve for any kind of riblets, as shown in Figure 2.7. The curve first follows a viscous regime where riblet protrusion is immersed in the viscous sublayer and the outer layer behaves the same as on smooth wall (Garcia-Mayoral and Jimenez 2011). Up to $s^+ \approx 17$, SFR monotonically increases (Bechert et al. 1997). At this optimal riblet spacing of $s^+ \approx 17$, SFR reaches maximum and the viscous regime starts to break down (Bechert et al. 1997, Jimenez 2004). As a consequence, SFR gradually diminishes and a drag increase regime with *k*-type roughness behavior forms (Jimenez 2004).

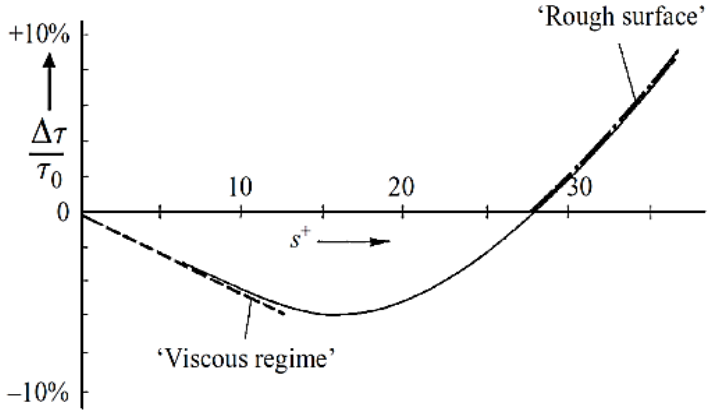

Figure 2.7. General structure of skin-friction reduction over riblet surface (Bechert et al. 1997).

2.2.2 Effect of riblet surface on turbulent structure

A summary of how the statistics of the turbulent flow fields are modified over riblet surfaces in both SFR and skin-friction increase (SFI) cases are present to help understand the mechanism that drives the changes.

Mean velocity profile

A semi-logarithmic plot of mean velocity profiles on riblet and smooth surfaces from hot wire measurement and DNS (Choi 1989; Choi, Moin, and Kim 1993) are shown in Figure 2.8. The mean velocities are normalized by friction velocities of the corresponding surface. In SFR case (Figure 2.8 (a)), it is seen that the slope of the log law over the riblet wall is the same as that of the smooth wall. However, the interception point of the log-law is increased from 5.45 for a smooth wall to 6.89 for the wall with riblets. Similar trends have been observed by Hooshmand et al. (1983) and Lee and Choi (2008) in riblet studies. Such a shift is also common with drag-reduced long-chain polymers (Lumley 1973; Virk 1975) and the slope of the log-law also increases in this situation. In SFI case (Figure 2.8 (b)), the location of interception over riblets is reduced as the log-law shifts downward. Lumley (1973) interpreted the upward and downward shift as the change of viscous sublayer thickness. It has been observed that the viscous sublayer becomes thicker in the SFR case while thinner in the SFI situation.

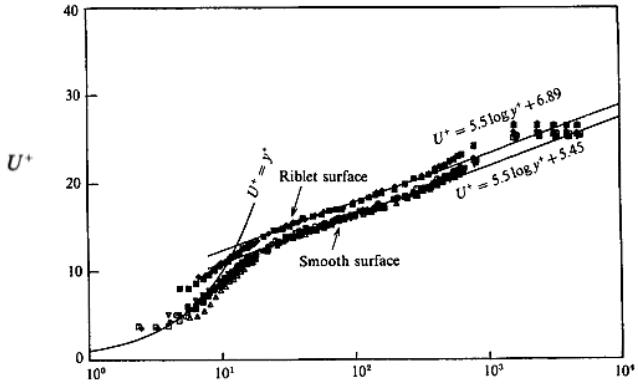

(a)

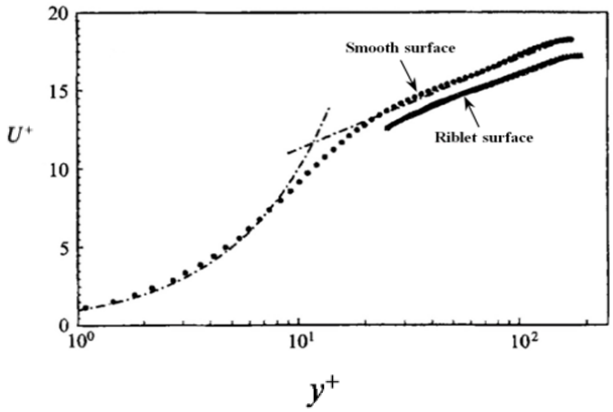

(b)

Figure 2.8. Semi-log plot of mean velocity profiles over smooth and riblet surfaces. (a): drag reduction data from (Choi 1989), (b): drag increase data of Choi, Moin, and Kim (1993).

The evidence to support the change of viscous sublayer thickness is provided from 3D particle tracking velocimetry measurement by Suzuki and Kasagi (1994). The velocity gradients almost vanish in the valley of drag-reducing riblets but become much larger in the riblet valley in the SFI case. As a result, the turbulent boundary layer is pushed up in the SFR case, giving rise to a thicker viscous sublayer, whereas the turbulent layer moves down in the SFI case, leading to a thinner viscous sublayer.

Turbulence intensities

The turbulence intensities shown in this section are obtained from DNS study of Choi, Moin, and Kim (1993) with the riblet wall located at $y / \delta = -1.0$ and a counterpart smooth wall at $y / \delta = 1.0$. Root-mean-square turbulence intensity at various spanwise locations from the

riblet valley to tip is shown in Figure 2.9. For the SFR case in Figure 2.9 (a), spanwise variation of turbulence intensities is small and limited only in regions near the riblet. All three components of turbulence intensities are attenuated over the riblet wall. For the SFI condition in Figure 2.9 (b), the spanwise variation turns larger, especially for the streamwise component. The effect of the riblets penetrates further towards the center of the channel and leads to an increase of turbulence intensities. The spanwise variation of wall-normal and spanwise components extends to regions without a noticeable spanwise variation of the streamwise component, showing that cross-flows are more sensitive to the existence of riblets. Yamaguchi et al. (2014) recorded reductions of the velocity fluctuations by riblets in a drag-reducing configuration. In addition, results by Suzuki and Kasagi (1994) showed the same trends of velocity fluctuation components in the SFR and in the SFI cases.

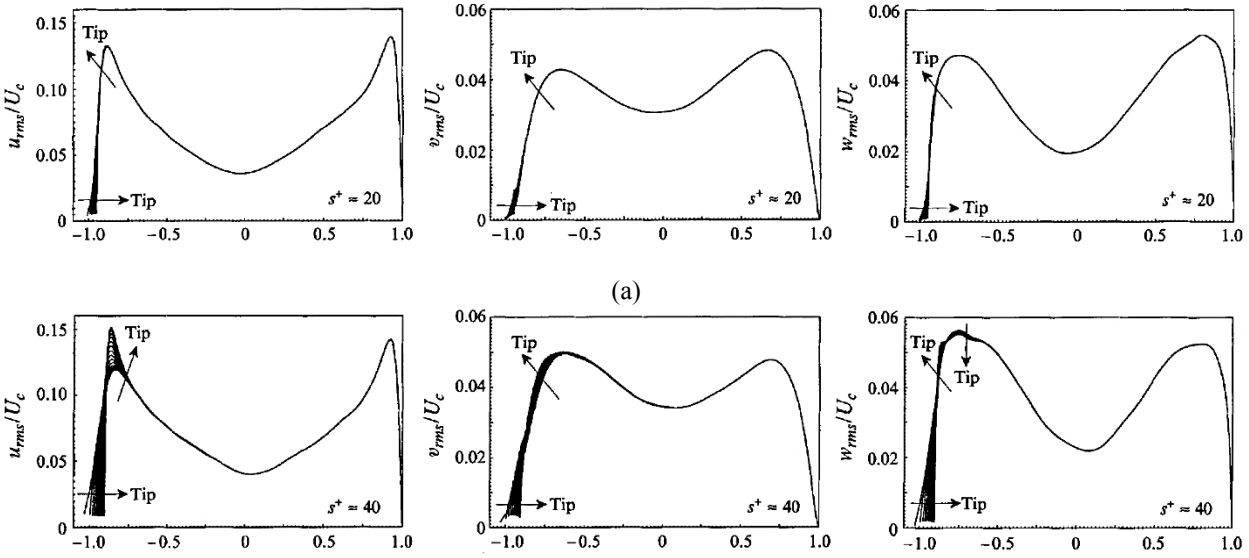

Figure 2.9. Root-mean-square velocity fluctuations normalized by mean centerline velocity U_c and channel half width δ. (a): drag reduction case, (b): drag increase case (Choi, Moin, and Kim 1993).

Normalized Reynolds shear stress is shown in Figure 2.10 from Choi, Moin, and Kim (1993). In drag-reducing situations (Figure 2.10 (a)), the maximum Reynolds stress is decreased by 12% over the riblet relative to the smooth side. In the case of SFI (Figure 2.10 (b)), the Reynolds shear stress continually increases from the valley to the tip, indicating spanwise variation. However, neither of the plots refers to differences in the slope of Reynolds stress between the riblet and the smooth wall, which should actually appear as an indication of drag change. It is

valid that the zero value of Reynolds shear stress no longer is located at the channel center, but shifts toward the riblet wall in the SFR case or towards the smooth wall in the SFI case in both Choi, Moin, and Kim (1993) and El-Samni, Chun, and Yoon (2007). In Figure 2.10 (a), a flipped Reynolds shear stress profile is attached to the original profile to investigate the effect of riblets. Only a shift of the zero value is spotted without showing the differences in the slopes near the riblet surface and near the smooth surface. The slope change or shift of the zero value is not discernable from 3D particle tracking velocimetry measurements by Suzuki and Kasagi (1994).

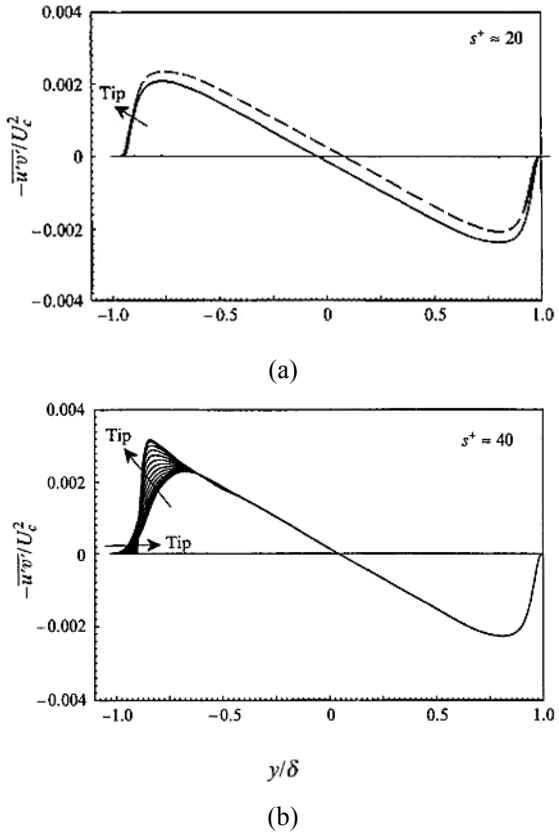

Figure 2.10. Reynolds shear stress normalized by mean centerline velocity U_c. (a): — original data in drag reduction case (Choi, Moin, and Kim 1993), ---- a 180 counter-clockwise degree rotation of the original data, (b): drag increase case (Choi, Moin, and Kim 1993).

To have a better understanding of the turbulent production sources, quadrant analysis of the normalized Reynolds shear stress with mean centerline velocity is shown in Figure 2.11. The four quadrants are defined in section 2.1.2. For all situations in Figure 2.11, a sweep has a little more contribution in the near wall region at around y / δ = -1.00 to -0.9 and later ejection grows to be dominant. First and third quadrant events persist nearly to be the same no matter the

condition, and they are of small scale. As turbulence producers, ejections and sweeps are adjusted with respect to the SFR and the SFI case. In the SFR configuration shown in Figure 2.11 (a), ejection and sweep events in any riblet regions are attenuated without noticeable spanwise variation. For the SFI case shown in Figure 2.11 (b), ejections and sweeps are strengthened above the riblet tip but decrease above the valley. Yamaguchi et al. (2014) reached similar conclusions in the SFR case.

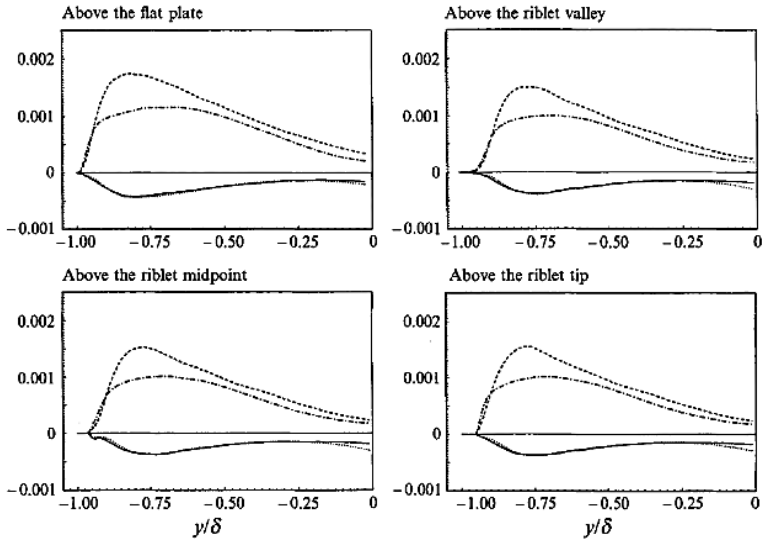

(a)

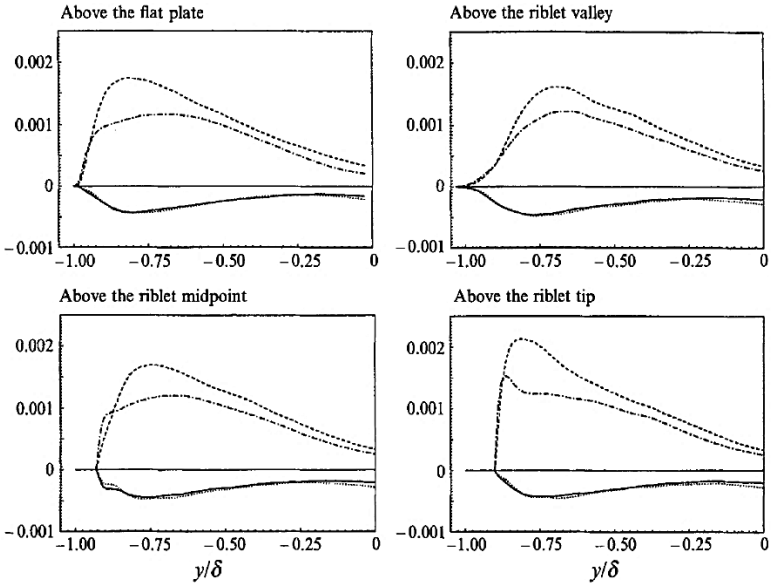

(b)

Figure 2.11. Reynolds shear stress from each quadrant normalized by the mean centerline velocity in drag reduction case, ---- first, - - - - second, ····· third, ·-·-· fourth quadrant. (a): drag reduction case, (b): drag increase case (Choi, Moin, and Kim 1993).

Vorticity

Normalized root-mean-square vorticity fluctuations with friction velocities and kinematic viscosity from DNS results (El-Samni, Chun, and Yoon 2007) are shown in Figure 2.12. Near the riblet region, all three vorticity components at the riblet valley are decreased and ω_x^+ and ω_z^+ are greatly increased near the riblet tip. The wall-normal vorticity component ω_y^+ remains zero both in the SFR and in the SFI cases. For ω_x^+, the peak location is almost identical for tip and valley in the drag-reducing condition, but is shifted in the SFI situation. Choi, Moin, and Kim (1993) also noted such change for ω_x^+. Different from the results from El-Samni, Chun, and Yoon (2007), Choi, Moin, and Kim (1993) have shown a larger value of ω_y^+ of the same level of ω_x^+ and ω_z^+ near the riblet. Due to the measurement difficulty, only Sasamori et al. (2014) have shown a reduced ω_z^+ over the riblet surface in the SFR case, and no other experimental data are available describing all three components of vorticity fluctuation, to the author's knowledge.

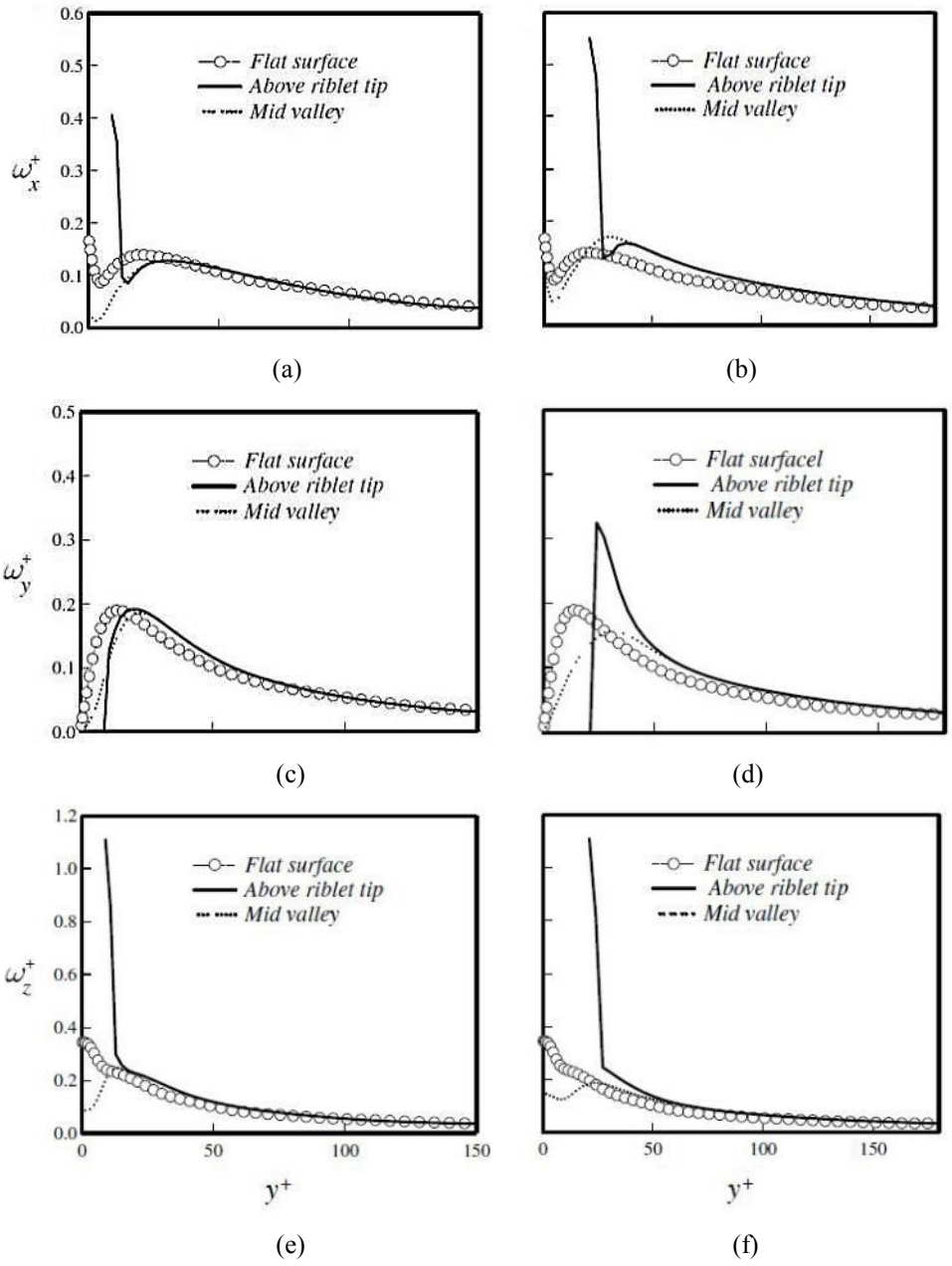

Figure 2.12. Root-mean-square vorticity fluctuations. (a), (c), (e): drag reduction case, (b), (d), (f): drag increase case (El-Samni, Chun, and Yoon 2007).

2.2.3 Skin-friction drag reduction mechanism

Wall shear stress over a riblet surface is redistributed, with higher values around the protruded tip regions, but low values are observed in the riblet valleys. Vukoslavcevic, Wallace, and Balint (1992) conjectured that the decrease of wall shear stress in the valleys is sufficient to overcome the increase over the tips. However, this does not provide a

satisfactory explanation for the changes of SFR as a universal function of s^+, as shown in Figure 2.7, for riblets with different shapes. The mechanism is also investigated in association with the near-wall coherent structures of turbulent wall flows. Chu and Karniadakis (1993) reported more anchored spanwise locations of streaky structures over riblets, indicating the inhibited spanwise motions of these streaks in their DNS study. Choi, Moin, and Kim (1993) reported a reduction of ejection and sweep motions but nearly unchanged first and third quadrant events over riblets, as it was shown in Figure 2.11 (a). They assumed riblets modify skin-friction through restricting motions of streamwise vortices. Later, Suzuki and Kasagi (1994) also mentioned that SFR is closely related to the limited motion of streamwise vortices.

Figure 2.13 from Lee and Lee (2001) shows the smoke-wire pictures of streamwise vortices near the riblets. The typical diameter of near wall streamwise vortices is around 30 wall units (Kim, Moin, and Moser 1987). In the SFR situation, a streamwise vortex stays above the riblets because its diameter is larger than the riblet tip spacing. Compared to the smooth surface case, the vortical motion is damped over the riblet surface and only a limited area of the riblet tips is exposed to their motion, resulting in a net SFR.

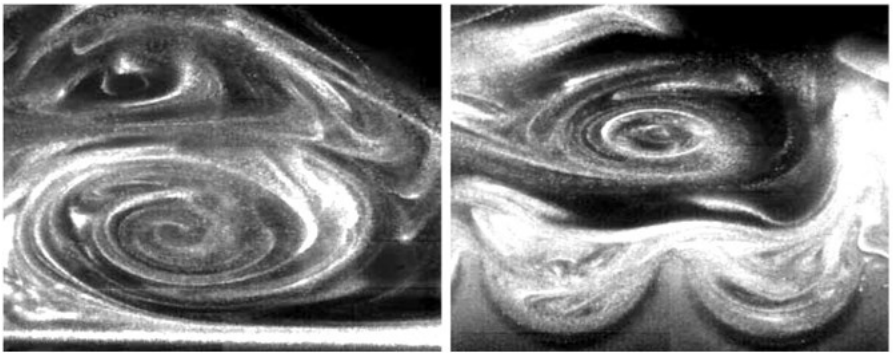

(a) (b)

Figure 2.13. Flow visualization images of streamwise vortices in the wall-normal spanwise plane. (a): smooth surface, (b): riblets surfaces (Lee and Lee 2001).

2.2.4 Novel riblets

A few recent investigations have focused on the improvement of riblet SFR ability by introducing new features beyond the two-dimensional traditional riblets. Three dimensional riblets inspired by active control that produce larger SFR (Sasamori et al. 2014) and riblets combined with superhydrophobicity have been explored. Instead of straight grooves in the

streamwise direction, wavy riblets studied by Kramer et al. (2010) have a sinusoidal pattern, while the riblet tip spacing s is kept constant, as shown in Figure 2.14. These riblets combine the effect of two dimensional riblets and spanwise wall oscillation. The wavelength and amplitude of sinusoidal patterns varied in their investigation. However, they concluded that the uncertainties in the experiments, including statistical errors and limited number of tests, made it difficult to demonstrate a clear benefit of wavy riblets over two dimensional ones. Sasamori et al. (2014) investigated the SFR ability of sinudoidal riblets with the riblet tip spacing s varying as a sine wave in the streamwise direction. The results from the pressure drop measurements showed that the sinusoidal riblets bring only a small improvement in SFR. Chen et al. (2014) were inspired by bird flight feather and introduced two herringbone-type riblets: plane 3D (p-3D) and spatial 3D (s-3D) herringbone riblets, as shown in Figure 2.15. The p-3D and s-3D riblets achieved 17% and 20% SFR, respectively. Such a breakthrough is possibly from the generation of spanwise vortices over the riblets. These spanwise vortices may damp bursting of the streamwise vortices, thus reducing skin-friction.

Streamwise slip on a SHS can reduce skin-friction but spanwise slip on the surface causes SFI (detailed in section 2.3.2). To improve the performance of SHS, Barbier, Jenner, and D'Urso (2012) fabricated SHSs over riblet grooves to align the flow along the streamwise direction and minimize the flow in the spanwise direction. The depth of the sawtooth grooves varied from 10 μm to 1000 μm. The SHSs were created by a combination of anodized nanopores and a hydrophobic polymer coating. The measurement results in the transitional and turbulent regimes in a cone-and-plate rheometer showed that up to 20% SFR is reached over 100 μm deep grooves coated with SHS. On the coated grooves with 10μm and 1000μm in depth, SFR is decreased but still present. Prince, Maynes, and Crockett (2014) manufactured surfaces combined with riblets and superhydrophobic micro-ribs using photolithography. They obtained higher SFR in low Reynolds numbers ($5{,}000 < \mathrm{Re} < 9000$) compared to SFR with riblet surfaces. However, with increase of Reynolds numbers ($11{,}000 < \mathrm{Re} < 15{,}000$), limited SFR was observed which possibly resulted from the lost air pockets in the SHS. If the results are expressed as a function of s^+, when riblets were at low s^+ (< 15), the SFR increases over the coated riblets. But at high s^+, SFR over coated riblets is similar to that over the bare riblets.

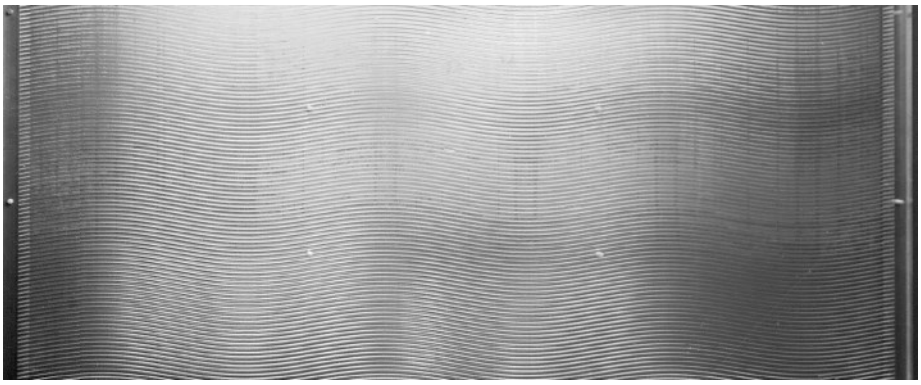

Figure 2.14. Part of the test plate with wavy riblets (Kramer et al. 2010).

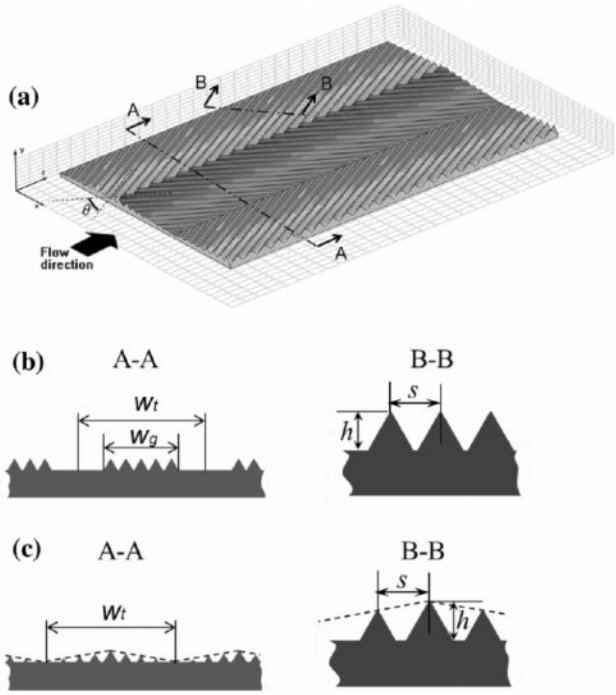

Figure 2.15. Bio-inspired 3D herringbone riblets. (a): Schematic of fluid flowing upon herringbone riblets, (b): the plane-3D herringbone riblet, (c): the spatial-3D herringbone riblet (Chen et al. 2014).

2.3 Superhydrophobic surfaces

2.3.1 Fundamentals

Fabrication of a SHS is inspired by water expelling properties in nature, such as lotus leaves, duck feathers and water-strider legs. Take the lotus leaf as an example: air is enclosed in the cavities of the hieratical surface structures built by convex cells, so the wetting of the surface is minimized (Yan, Gao, and Barthlott 2011). SHSs are synthesized mainly through roughening hydrophobic materials (e.g., plasma etching fluorinated polymers, poly surfaces processed with laser abrasion), making rough structures followed by hydrophobic treatments (e.g., photo-lithography, anodization), or depositing hydrophobic materials with rough textures (e.g., plasma polymerization, electron spinning) (Kim 2008).

Wetting phenomena

Heterogeneous and homogeneous states exist when a water droplet is on a SHS: as shown in Figure 2.16.

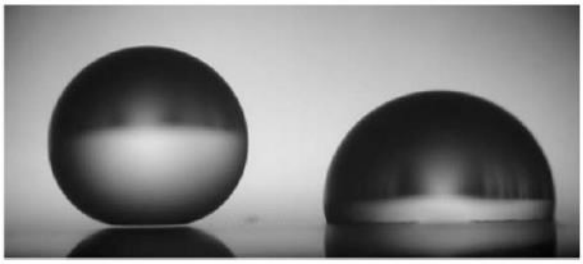

Figure 2.16. Water drops deposited on a superhydrophobic substrate. Left: heterogeneous state, right: homogeneous state (Yan, Gao, and Barthlott 2011).

In the heterogeneous state, water stays above the air layer entrapped in the groove structures. The Cassie-Baxter equation describes the state as

$$\cos\theta^* = -1 + \varphi_s(\cos\theta + 1), \tag{2.30}$$

where θ^* is the Cassie-Baxter contact angle, φ_s is the fraction of solid protrusion wetted by the liquid and θ is the contact angle on the solid surface. The definition of θ is shown in Figure 2.17. The homogeneous state corresponds to the liquid drop filling up the rough grooves and the Wenzel equation applies to the state as

$$\cos\theta = \frac{\gamma_{SV} - \gamma_{SL}}{\gamma_{LV}}, \tag{2.31}$$

where γ is the surface tension. Also definitions of SV, SL and LV are given in Figure 2.17.

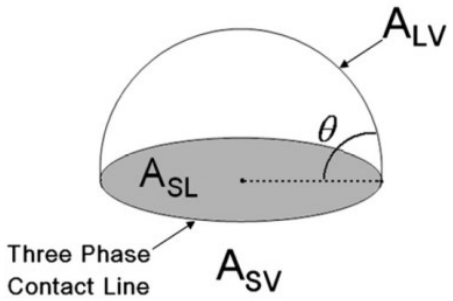

Figure 2.17. A liquid drop showing contact angle θ balanced by three interfaces. The letter 'A' indicates the interfaces as well as their contact areas. SV, SL and LV correspond to the interfaces between solid, liquid and vapor, respectively (Yan, Gao, and Barthlott 2011).

According to Yan, Gao, and Barthlott (2011), the occurrence of the homogeneous or of the heterogeneous state also depends on how the droplet is delivered and formed on the surface.

Contact angle and contact angle hysteresis

Contact angle hysteresis is defined as

$$\Delta\theta_H = \theta_A - \theta_R, \tag{2.32}$$

where θ_A is the advancing angle and θ_R is the receding angle shown in Figure 2.18. Contact angle and contact angle hysteresis are characterization measures to compare the surface superhydrophobicity. A surface is considered superhydrophobic when its contact angle is higher than 150°. The contact angle hysteresis is lower, usually less than 5°, this permits the free rolling of water droplets on the surface.

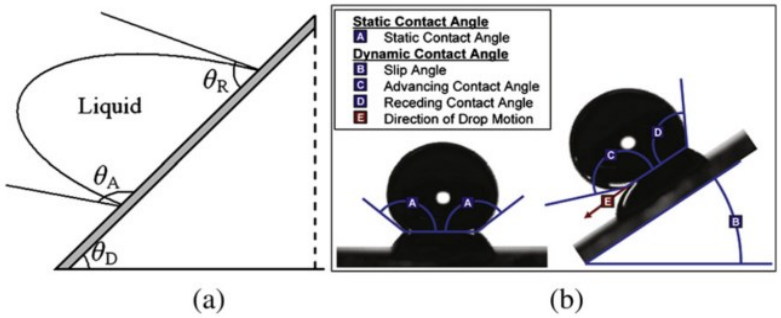

Figure 2.18. (a): A liquid drop theoretically sliding on a declination of θ_D without acceleration. θ_A is the advancing angle, and θ_R is the receding angle, (b): The schematic of static contact angle and dynamic contact angles (Yan, Gao, and Barthlott 2011).

Slip length

Another important criterion of superhydrophobicity is slip length l_s or slip velocity u_s. Slip velocity, as shown in Figure 2.19, is an averaged effect of the no-slip region over solid and slip-free (or sheer free) region over the gas pockets (Lam et al. 2014). Slip length is the distance inside the solid surface where the velocity extrapolation goes to zero. Large slip lengths generate low friction between flowing liquids and solid boundaries (Maali et al. 2012). The relationship between the slip length and the slip velocity is

$$u_s = l_s \frac{dU}{dy}\Big|_{y=0}. \tag{2.33}$$

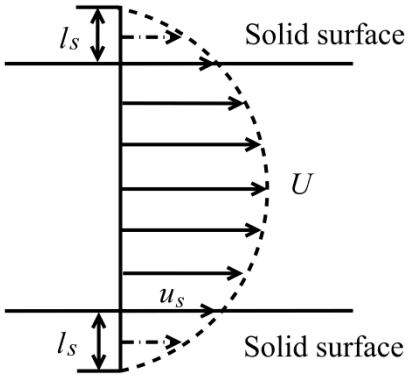

Figure 2.19. Slip length l_s and slip velocity u_s over superhydrophobic surface.

With a larger ratio of slip-free surface to no-slip solid surface, u_s will increase. Regarding the slip directions, isotropic slip represents identical slip length in both the streamwise and spanwise directions and anisotropic slip is the biased slip length in one direction.

2.3.2 Superhydrophobic surfaces in turbulent flows

SFR has been observed in laminar and turbulent flows over SHSs maintained in the Cassie state as a result of fluid slip on the surface (e.g., Davies et al. 2006; Maynes et al. 2007; Daniello, Waterhouse, and Rothstein 2009; Woolford et al. 2009). Experimental results by Ou, Perot, and Rothstein (2004), DNS by Davies et al. (2006) and theoretical analysis of Lauga and Stone (2003) in laminar flows are in agreement with the aspect of charactering the change of the slip length as a function of shear free fraction and channel height. However, the performance of SHSs in turbulent regimes is not well understood.

Min and Kim (2004) and Rastegari and Akhavan (2015) noticed SFR upon applying streamwise slip and SFI by applying spanwise slip in DNS studies. SFR up to 50% has been observed from particle image velocimetry or pressure drop measurements with longitudinal micro-grooves (Peguero and Breuer 2009, Woolford et al. 2009, Daniello, Waterhouse, and Rothstein 2009). Both Min and Kim (2004) and Jelly, Jung, and Zaki (2014) reported an upward shift of mean velocity profile and a reduction of turbulence intensities and streamwise vortices in DNS over SHSs with streamwise slip. However, the particle image velocimetry experiments by Woolford et al. (2009) and Vajdi Hokmabad and Ghaemi (2016) only showed negligible change of the mean velocity profile. Rastegari and Akhavan (2015) analytically and numerically obtained a downshift of the log layer and explained that the phenomenon was resulted from a weaker near-wall velocity gradient over the slip-free wall, and consequently resulted in a thinner sublayer.

2.4 Measurement techniques

2.4.1 Particle image velocimetry

The hot-wire anemometer was popular in the earlier years of turbulence research, even though it is an intrusive single-point measurement. As an advanced technology, laser Doppler anemometry overcomes the flow field intrusion problem by employing laser beams. However, it still cannot capture a large area in the flow field. PIV is a planar flow measurement technique that has been practiced for the last three decades and is capable of obtaining instantaneous flow fields with high accuracy.

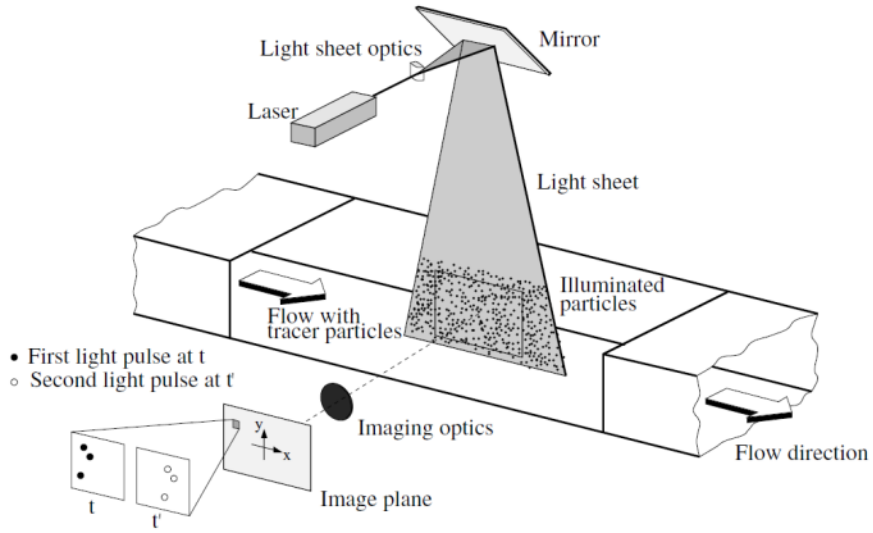

Figure 2.20. Experimental arrangement for particle image velocimetry in a wind tunnel (Raffel et al. 2007).

The principle of PIV can be simply depicted in Figure 2.20 (Raffel et al. 2007). The flow field is seeded with particles that are assumed to follow the fluid motions and have been homogeneously distributed in the flow. A laser sheet illuminates a plane, which is the region of interest in the flow. Particle motions are frozen using two laser pulses with time delay Δt which depends on the mean flow velocity and the image magnification. A camera collects two images of the scattered light of the seeded particles with Δt time separation. The images are divided into small sub sections called interrogation windows to be processed. It is assumed that all particles within an interrogation window share a uniform displacement. The interrogation areas in two images are cross-correlated and a peak detection algorithm is used to find the maximum peak to generate a displacement vector Δx. The velocity vector is then calculated to be $V = \Delta x / \Delta t$. PIV requires four basic components: (1) an optically transparent test section with seeding particles, (2) a light

source that illuminates the region of interest, (3) recording equipment such as a CCD or CMOS camera, (4) a computer with image processing software to obtain velocity vectors Prasad (2000a).

Seeding

Two requirements need to be taken into account in choosing particles: (1) particles should faithfully follow the fluid in order to characterize flow patterns (2) sufficient scattering of the illumination laser should be reflected to the recording hardware (Prasad 2000a).

For the first criterion, the influence of gravitational forces will appear if the densities of the fluid ρ_f and the seeding particles ρ_p do not match. Assuming spherical particles in viscous fluids at a very low Reynolds number, Stokes' equation can be used to derive U_g, the gravitationally induced velocity as

$$U_g = d_p^2 \frac{(\rho_p - \rho_f)}{18\mu} g, \tag{2.34}$$

where g is the acceleration due to gravity, μ the dynamic viscosity of the fluid and d_p the diameter of the particle (Raffel et al. 2007). Particles are suitable only when U_g is negligible compared to the actual flow velocities (Prasad 2000a).

For the second condition, the particles must be able to reflect a sufficient amount of light for camera detection. In general, the amount of scattered light of small particles depends on the ratio of the refractive index of particles over the surrounding medium, particle size, shape and orientation as well as polarization and observation angle (Raffel et al. 2007). Consider particles with a diameter of d_p larger than the laser wavelength λ as an example, Mie's scattering theory can be applied (Raffel et al. 2007). Figure 2.21 shows the normalized polar distribution of scattered light intensity from a 10 μm glass particle in water illuminated at $\lambda = 532$ nm. As is seen, the light spreads in all the directions. In order to avoid massive multi-scattering from a heavily seeded flow, the best shooting angle is 90˚ since the intensity is much smaller than the forward scattering angles (90˚ to 180˚) (Raffel et al. 2007).

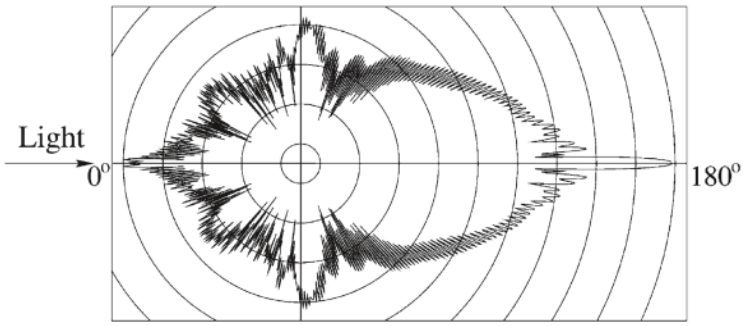

Figure 2.21. Light scattering by a 10 μm glass particle in water (Raffel et al. 2007).

In order to increase sub-pixel accuracy in particle position calculations, the particles must be large enough to be represented on the camera by multiple pixels, for eample 2 pixels for a given field of view and magnification (Norconk 2011).

Particle number density on the image is another important parameter. Strong cross-correlation can be obtained if there are around 15 particles for each interrogation window on the raw PIV images (Norconk 2011).

Light sources

Lasers are monochromatic and possess a high energy density. As the widely used light source in PIV, laser light can be easily formed into a thin light sheet to illuminate and freeze the motion of seeding particles (Raffel et al. 2007). Prasad (2000a) has provided a detailed analysis of the characteristics of both pulsed and continuous wave lasers in PIV.

A pulsed laser has short pulse duration of typically a few to several nanoseconds. Usually the motion of a particle traveling at very high speed can be frozen in this time duration without severely blurring the image. Pulsed lasers applied for PIV are typically Nd:YAG lasers with repetition rates of tens of Hz.

There are four main factors determining the performance of lasers: energy, timing, beam thickness and alignment. To allow for maximum signal strength, the laser pulse energy should be set as high as possible but below the saturation point of the equipped camera (Norconk 2011).

By accurately controlling the time separation between two identical lasers that are delivered consecutively based on the flow velocity and magnification, the displacement of particles can be

controlled. With a trigger signal, all the hardware can be synchronized so PIV data can be obtained with a frame-rate equal to the repetition rate of the lasers (Prasad 2000a).

Regarding the laser sheet thickness, it should be noted that the depth of focus of the imaging system should be larger than the thickness of the laser sheet.

Proper alignment of lasers is critical, ensuring that the light sheet is at the center of the depth of focus, beam profiles of the two lasers are kept the similar, and the two laser pulses overlap to illuminate the same sets of particles (Norconk 2011).

Image detectors

Particle images are collected by charge coupled device (CCD) cameras. The basic working principle of a CCD is to convert light to electric charge and the individual element in a CCD sensor is called a pixel (Raffel et al. 2007). Three of the key parameters to compare the performance between CCD are: resolution, exposure time, and quantum efficiency (Jahanmiri 2011). A camera with higher resolution provides more detailed information of the objects. Exposure time should be short enough to tolerate flows with high velocity so the camera is able to take two images within a short time delay. A camera with higher quantum efficiency, which means higher number of photons translating to electrons, is more desirable especially when particles are small or the laser light intensity is low.

The relations between object distance d_o and image distance d_i, and magnification M and focal length f are:

$$M = d_i / d_o, \tag{2.35}$$

$$d_o = (1 + \frac{1}{M}) f, \text{ and} \tag{2.36}$$

$$d_i = (1 + M) f. \tag{2.37}$$

Particle image diameter is a function of both the geometric and the diffraction effects. The geometric effect alone gives the particle image diameter d to be

$$d = M d_p, \tag{2.38}$$

where d_p is the particle diameter.

Due to the diffraction effect, a point source in the object plane will be spread out in the image. The diffraction limited spot size d_s is governed by the lens aperture D, the wavelength of the illuminating laser λ and the focal length f as

$$d_s = 2.44\,(1 + M)\frac{f}{D}\,\lambda. \tag{2.39}$$

The effective diameter d_e can be obtained by incorporating these two effects in one equation

$$d_e = (M^2\, d_p^2 + d_s^2)^{1/2}. \tag{2.40}$$

The depth of field (DOF) is the thickness of the region where the particles are in acceptable focus. It is written as

$$\mathrm{DOF} = 4(1 + \frac{1}{M})^2 f\#^2\lambda, \tag{2.41}$$

where $f\#$ is the aperture setting defined as f / D.

DOF will increase rapidly with the increase of $1/M$ and $f\#$. As referred before, to avoid out of plane particle images, DOF should be slightly larger than the thickness of the laser sheet.

Image processing

Image processing is needed to extract the particle displacement. Factors such as non-uniform illumination and image sensor noise will degrade the performance of cross-correlation algorithms for double-frame images. Since brighter particles in an interrogation window will contribute more to the cross-correlation signal, the velocity vector is biased to their displacements. One solution to this problem is enhancing image contrast and bringing particle image intensity to a similar signal level before carrying out cross-correlation (Raffel et al. 2007).

Background subtraction helps reduce the effect of laser flare and stationary image sensor noise (Raffel et al. 2007). Such a background can be computed from the minimum intensity image using a large set of raw PIV images.

For the cross-correlation algorithms, a fast Fourier transform (FFT) computes the correlation matrix in the frequency domain. Shift between the interrogation windows is represented with the highest peak value of the correlation map, which is estimated by applying sub-pixel peak fitting.

Dividing the shift values by the time interval between the double frames yields the velocity vectors, as shown in Figure 2.22.

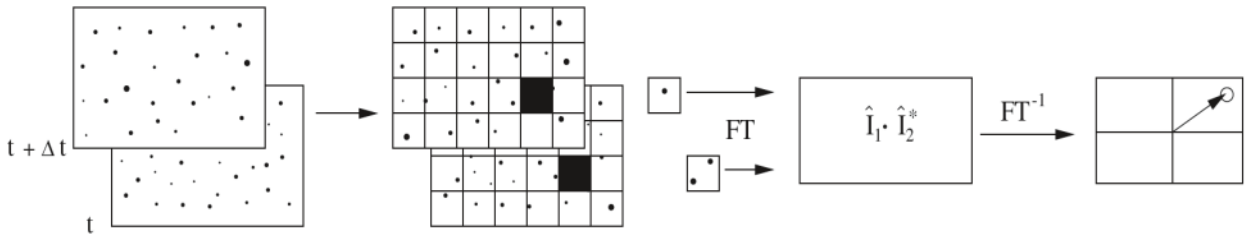

Figure 2.22. Analysis of double frame/single exposure recordings: the digital cross-correlation method (Raffel et al. 2007).

Post-processing is critical as the last step is to eliminate inappropriate outliers due to the background noise, window offset and accidently matched particles. One of the effective ways to filter outliers is by limiting the velocity range manually. After rejecting spurious vectors, data interpolation can be applied to replace the missing vectors and obtain a continuous velocity field.

Error analysis

During the whole process of acquiring particle images and image processing, many errors will be caused which affect the velocity calculation. Different types of error sources have been explained by Harris (2012), Prasad (2000a) and Raffel et al. (2007). Some of the dominant ones will be discussed below.

(1) Calibration: calibration aims to obtain a scale factor that converts pixel dimension to physical dimension. Due to the camera resolution limit, the image will be discretized. Error will occur when the user chooses two centers of points with a known distance apart in the image of the calibration target. Such error can be lower by repeating the calibrations for a few times and averaging the scale factors.

(2) Perspective: any out of plane particle motions will add error to the in plane velocities. Large perspective error happens when the viewing angle is wide or if magnification is high and in particular affects particles in the corners of the image.

(3) Algorithm: peak detection in the cross correlation algorithm works to find the most possible displacement in the interrogation windows. The location of the peak, however, can be influenced by random correlations between accidently matched particle pairs. It is also biased to the nearest

pixel, which is called the peak-locking effect. These two phenomena cause errors and such errors become larger when the particle image diameter is small (≈ 1 pixel).

(4) Gradient: in a turbulent flow, the rotation and deformation of fluids lead to loss of correlation information which then lowers the peak detection accuracy.

2.4.2 Tomographic PIV

Tomographic PIV measures the particle motions in a three-dimensional domain based on the simultaneous views of several cameras oriented in different observation directions. In this way, the three dimensional structure of complex flows can be revealed, such as the coherent structures in turbulent boundary layers (Raffel et al. 2007). The working principle of tomo-PIV is shown in Figure 2.23: a 3D region seeded with tracer particles is illuminated by light source; particle images are recorded by cameras viewing at different angles in double-frame mode; reconstruction of 3D particle positions are based on the mapping function extracted from the calibration procedure; 3D spatial cross correlation is applied to the reconstructed volumes to yield particle displacements (Raffel et al. 2007). The main components of tomo-PIV adopted from Scarano (2013) are introduced in this section.

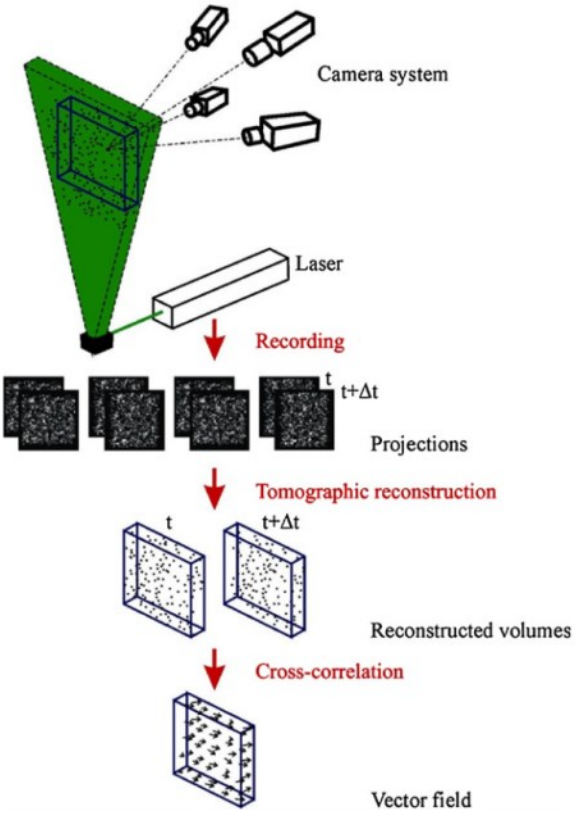

Figure 2.23. Working principle of tomographic PIV (Elsinga et al. 2006).

Volume illumination

The measurement volume is formed by an expanded light sheet to a depth that is typically one-quarter the width or length of the field of view. For a particular field of view, the light intensity is inversely proportional to the thickness of the measurement volume. In order to guarantee sufficient light intensity and in-focus particles collected by the imaging systems, a large amount of light is required to scale up the large measurement volume. Some special arrangements such as multi-pass light amplification are applied to distribute the laser light over a larger region. A knife-edge filter is used to cut the light beyond the thickness of the measurement volume, thus any out of volume motion will not be recorded in the images.

Seeding

The concentration of tracer particles should be controlled properly in a way that it is enough to permit a robust cross-correlation analysis but below the maximum image source density to satisfy accurate reconstruction procedures. For the former one, it is recommended to have 5-10

particles within an interrogation volume. For the latter, Elsinga et al. (2006) showed that a seeding density of 0.05 ppp (particles per pixel) is needed to obtain accurate reconstruction for a four-camera system. This criterion can be translated to $N_s = 0.3$ where N_s is the source density, defined as the fraction of the digital image occupied by the particle images.

Imaging systems

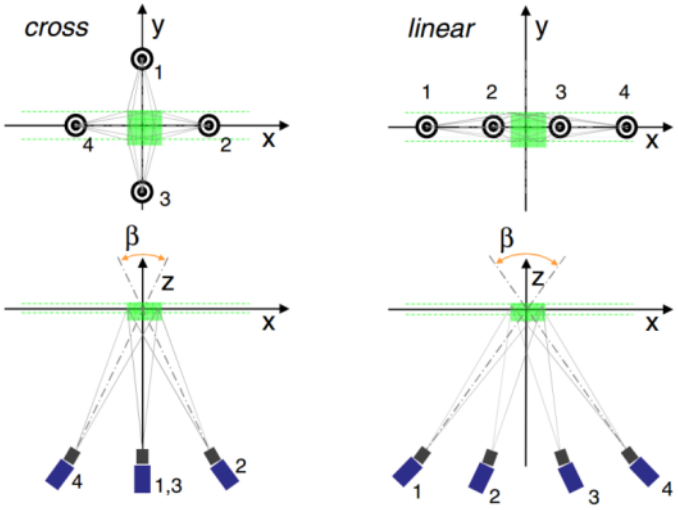

(a) (b)

Figure 2.24. Imaging configurations of tomographic PIV systems based on four cameras. (a): cross-like, (b): linear (Scarano 2013).

The imaging system usually consists of a small number of cameras placed along non-collinear viewing directions. Parameters such as camera specifications, the relative angle between the illumination and imaging direction, and alignment between the focal plane and the mid-plane of the measurement volume would affect the performance of the imaging system. The depth of field of cameras should be chosen to be larger or equal to the depth of the illuminated volume to have sharp particle images. The maximum planar angle β determines the depth resolution of tracer particles. Definitions of β in a cross-like and in a linear array of camera configurations are shown in Figure 2.24. Elsinga et al. (2006) reported for a suggested β ranging from 40˚ to 80˚ to reach the maximized accuracy of reconstruction. Higher value leads to longer lines of sight across the measurement volume while smaller values cause elongated particle images. In either situation, the reconstruction quality will be decreased.

Calibration

Calibration refers to the determination of a mapping function which provides an algorithm to relate the 3D physical space to an image space (Willert 1997, Prasad 2000b). A calibration plate with signs labelled on a pre-known regular grid is placed at several positions in the measurement volume to record images at different views. The third order polynomial and the pinhole model are the most adopted for mapping function calculation. Self-calibration developed by Wieneke (2008) is then performed to reduce large misalignment error to below 0.1 pixels based on triangulation of detected particles in the individual image. The disparity vectors are applied to correct the mapping function.

3D intensity reconstruction

Reconstruction of the light scattering field from images is on the basis of the mapping function. Figure 2.25 schematically shows the projection configuration. Relation between the 3D light intensity distribution of the j^{th} voxel $E(x_j, y_j, z_j)$ in the physical space and the intensity $I(x_i, y_i)$ of the i^{th} pixel in the image is established as

$$\sum_{j \in N_i} w_{i,j} E(x_j, y_j, z_j) = I(x_i, y_i), \tag{2.42}$$

in which N_i is the neighborhood of the voxel in the line of sight of the i^{th} pixel (x_i, y_i) (named weighted cross section in Figure 2.25). $w_{i,j}$ is the weighted coefficient describing the contribution of the $E(x_j, y_j, z_j)$ to $I(x_i, y_i)$. The distribution of $E(x_j, y_j, z_j)$ can be computed using the iterative multiplicative algebraic reconstruction technique (MART).

Reconstruction accuracy can be evaluated through the signal to noise ratio (SNR) determined from the ratio of light intensity in reconstructed region and outside the region. SNR ≥ 2 is taken as the minimal condition for an accurate reconstruction. After reconstruction with good quality, the 3D motions of particles are extracted by cross correlation over interrogation volumes and locations of maximum displacement are estimated with sub-pixel accuracy.

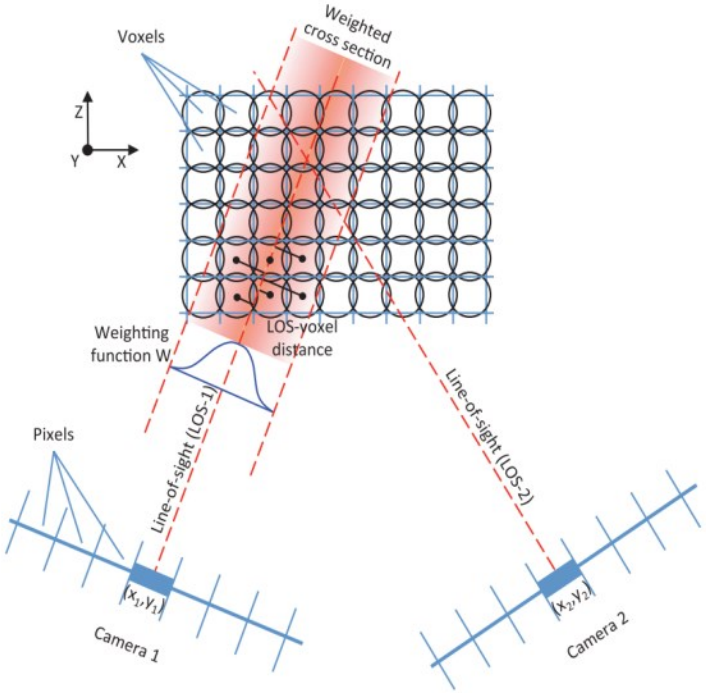

Figure 2.25. Object discretization and imaging model used for tomographic reconstruction. The voxels falling within the shaded stripe (weighted cross section) have nonzero value of the weighting coefficient $w_{i,j}$. Spherical shape for voxels is commonly assumed that simplifies the calculation of the weighting coefficient (Scarano 2013).

2.4.3 Particle tracking velocimetry

Particle tracking velocimetry (PTV) is a technique consisting of similar imaging equipment as PIV. In two dimensional PTV measurements, a plane in the flow field is illuminated and two images of particles passing by are taken. A three-dimensional PTV set-up includes several cameras looking through different views and synchronously recording the particle displacements. However, PTV tracks the motion of individual particles in consecutive image frames and computes the velocity vector of each particle (Baek and Lee 1996). In this way, it is essential to identify and link particles from one image to the next correctly which requires an algorithm sophisticated enough (Maas, Gruen, and Papantoniou 1993; Prasad 2000a). Ideas behind a PTV algorithm include: noise is eliminated by setting a threshold for the raw images; fragmented but bright particles can be picked up by setting distortion ratios; overlap of particles is decreased by lower particle concentration in the flow fields; limiting the search volume within the candidate area for particles at dispersed locations; computing centroids of bright pixels as particle centers; grid (window) generation to calculate the vectors (Maas, Gruen, and Papantoniou 1993; Prasad 2000a). Compared to large cross correlation window size in PIV, PTV has the advantage

of smaller averaging bin size. At the same time, PTV is able to provide information such as number of particles and particle size (Kolehmainen et al. 2014).

Chapter 3. Experimental setup

Two experiments with different objectives are described in this chapter. In the first experiment (detailed in 3.1), performance of two dimensional and three dimensional PIV and PTV systems are evaluated on a riblet surface and compared with a smooth surface. Skin-friction obtained from the mean velocity and turbulent statistics over these surfaces are compared to the literature in order to evaluate the measurement accuracy. The second experiment (detailed in 3.2) employs a two dimensional PIV to investigate the turbulent flow over riblet surfaces and surfaces combining riblets with superhydrophobicity. Flow measurement on a smooth surface and smooth surface coated with superhydrophobic layer are also carried out as well to serve as a reference. The flow setup is also improved in the second experiment to reduce the effect of free surface on the channel flow.

3.1 Evaluation of 2D/3D PIV/PTV on a riblet surface

3.1.1 Flow facility

The experiments were carried out in a closed-loop, free-surface water channel with a 5.2 m long and 0.68 m wide test section partially filled to a height of 0.23 m to increase the flow velocity. A 2D channel flow with 3 m length (L) in the streamwise (x) direction as shown in Figure 3.1 was formed using a bottom glass plate and an upper cast acrylic plate inside the water channel. The cross section of the formed channel was 20 mm high (H) and 540 mm wide (W), corresponding to y (wall-normal) and z (spanwise) directions, respectively. A honeycomb flow straightener was placed at the entrance to break down the large vortices and to increase the uniformity at the entrance. The bottom glass plate was kept 30 mm above the water channel bottom wall to prevent the boundary layer from entering the 2D-channel. This ensures formation of new boundary layers on both lower and upper walls and a symmetric profile. There is a 570 mm long and 320 mm wide interchangeable module 1.8 m (90H) downstream of the entrance where the turbulent channel flow is expected to be fully developed. The relatively large flow facility allows larger turbulent length scales to prevent the need for extremely miniaturized riblets and to allow increased manufacturing and assembly tolerances.

The instantaneous velocity components in the x, y and z directions are specified by U, V and W while the fluctuations are denoted by u, v, and w. The average velocity across the channel along the y direction was $U_b = 0.24$ m/s. The Reynolds number based on the full channel height was $Re_H = 4780$ with kinematic viscosity of $\upsilon = 1.004 \times 10^{-6}$ m^2/s. The wall unit was $\lambda = 67.9$ μm and the friction velocity was $u_\tau = 0.0148$ m/s over the smooth wall, measured using the PTV system as detailed in section 4.2.2. Reynolds number based on friction velocity and half channel height was $Re_\tau = 147$.

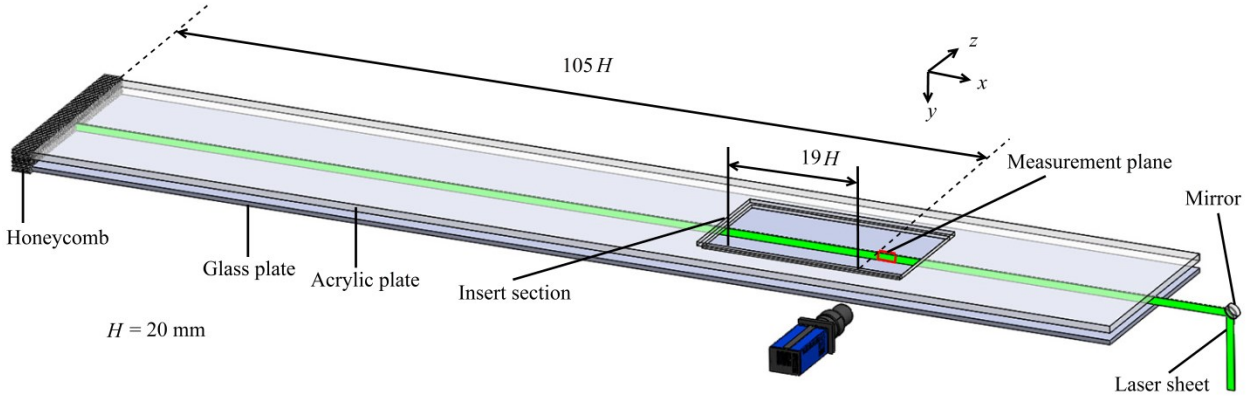

Figure 3.1. A schematic of the experimental setup showing the 2D-channel, the insert module to place the riblet or smooth surface, and the PIV measurement setup.

3.1.2 Riblet and smooth surface

The riblet surface consists of trapezoidal grooves with $s = 750$ μm, $h = 375$ μm and $\alpha = 30^\circ$ as shown in Figure 3.2 was manufactured by CNC milling (with machine tolerance: 12.7 μm) on a cast aluminum block. The dimensions correspond to $s^+ = 11$, $h / s = 0.5$. The reference smooth plate was also made of cast aluminum. Both surfaces were 430 mm long, 280 mm wide and 6.35 mm thick. The surfaces could be placed inside the interchangeable module. The riblet plate was positioned so that two fifths of the height (i.e., $h_{p0} = 150$ μm) of the riblet tip protrude into the channel wall flow. This protrusion maintains the same outer layer velocity profile for both smooth and riblet experiments (Grüneberger and Hage 2011; Duan and Choudhari 2012) and will be explicitly explained in section 4.2.1.

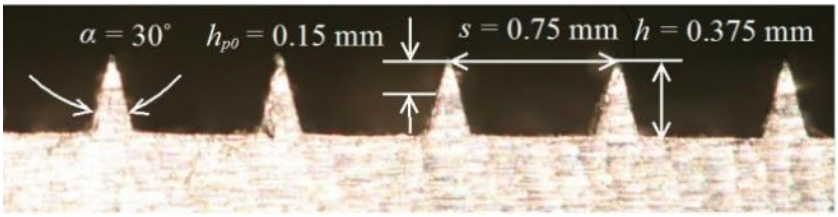

Figure 3.2. An image of the cross-section of the riblet plate machined on cast aluminum.

3.1.3 Particle image velocimetry

PIV measurement was carried out at magnification of $M = 0.37$ to cover the turbulent flow across the full channel height. The system consisted of an Nd:YAG laser (Spectra-Physics, PIV400) with 532 nm wave length, maximum output of 400 mJ per pulse, and maximum repetition rate of 10 Hz. A combination of cylindrical and spherical lenses was used to reshape the laser beam into a collimated laser sheer with 1 mm thickness. The laser sheet in this thickness was able to cover a full riblet from tip to tip ($s = 0.75$mm). The collimated laser sheet was directed in the streamwise direction parallel to the channel walls by a mirror sealed inside an acrylic column downstream of the measurement region, as shown in Figure 3.1. The wall parallel laser sheet reduced the wall reflection issues in the PIV and PTV images.

Silver-coated glass spheres (Potters Industries Conduct-O-Fil® SG02S40) with 2 μm diameter and density of 4 g/cm^3 were added to the water flow as the tracer particles. The scattered light from the tracer particles was captured by a 2048×2048 pixel (7.4 μm×7.4 μm) 14 bit CCD camera (Imager proX, LaVision GmbH) equipped with 105 mm SLR objective at aperture opening of f/11. The field of view (FOV) was 40.5 mm×40.5 mm extended to 5 mm upstream of the test plate end (110H from the entrance and 20H from the beginning of the test plate). The digital resolution was 52 pixel/mm and the DOF was estimated to be 3.5 mm. The Nd:YAG laser and the CCD camera were synchronized using a pulse generator (LaVision Programmable Timing Unit) controlled by DaVis 8.2 (LaVision, GmbH). An ensemble of 10,000 pairs of double-frame images was recorded for each case with laser pulse separation of $\Delta t = 1000$ μs.

The signal-to-noise ratio of the images was improved by subtracting minimum intensity of the ensemble from individual images, followed by normalizing each image using the average of the ensemble. The images were processed both with an ensemble of the correlation method (EC method) (Meinhart, Wereley, and Santiago 2000) and the cross-correlation technique. The final

window size in the EC method was 16×16 pixels (0.31 mm×0.31 mm, 0.015H×0.015H, 4.5λ×4.5λ) with 75% overlap. Multi-pass cross-correlation was performed for each double-frame image with final interrogation window of 48×48 pixels (0.92 mm×0.92 mm, 0.046H×0.046H, 13.5λ×13.5λ) with 75% overlap to obtain instantaneous velocity vectors. Vector fields were post processed by applying an allowable vector range for both the streamwise (0 to 18 pixels) and the wall-normal (-3 to 3 pixels) velocity components, and also applying the universal outlier detection (Westerweel and Scarano 2005). All the processes were executed in DaVis 8.2 (LaVision GmbH). A summary of measurement parameters is available in Table 3.1 and sample images over the smooth and riblet walls are shown in Table 3.2.

3.1.4 Long-range micro-PTV

The PTV system at magnification of $M = 1.84$ was applied for high spatial-resolution measurements in the near wall region. The same laser, camera and programming time unit, and tracer particles as those in the PIV measurement were applied. The camera was equipped with a long-range microscope 12× zoom lens (Navitar) to obtain a FOV of 8.2 mm×8.2 mm with a digital resolution of 248 pixel/mm. The numerical aperture (NA) was estimated to be about 0.025 based on the magnification from the zoom lens performance datasheet (Navitar 2016). The DOF was approximately 1.02 mm (Young et al. 1993). An ensemble of 15,000 pairs of images was taken with $\Delta t = 190$ μs in double-frame mode. The images were improved by subtracting minimum intensity of the ensemble from individual images and normalizing each image by the average of the ensemble. In order to eliminate the peak locking effect, a 3×3 Gaussian smoothing filter was applied.

A MATLAB script was applied to detect particle pairs and obtain the velocity of individual particles based on their displacements. The algorithm first detected particles with intensity beyond a preliminary intensity of 100 counts. The local maximum within a kernel of 21 pixels was selected for pair detection. The analysis of Kähler, Scharnowski, and Cierpka (2012) showed that particles smaller than 3 pixels cause peak locking and result in biased error. Meanwhile, very large particles are typically aspherical due to astigmatism or out-of-focus effects. Therefore, an area filter was used to select particle pairs with 3-7 pixels in diameter. Further particle filtering was applied using ratios of the particles area (0.8-1.2), major over minor axis (0.7-1.3), and peak intensity (0.3-1.8) in the two image frames to reject erroneous particles and reduce

peak detection errors. A Gaussian filter with kernel of 7×7 pixels was applied to the selected particles for peak detection with sub-pixel accuracy.

A mean velocity field was obtained using the EC method (Meinhart, Wereley, and Santiago 2000) with a window size of 16×16 pixels and 75% overlap using the PTV images. This velocity field was used as a predictor for detection of particle pairs in the second frame followed by a search radius of 5 pixels. The vector field was post processed by limiting the wall normal velocity fluctuation to be smaller than 20% of the streamwise counterparts. Finally, the results were averaged over windows of 1910×8 pixels (7650 μm×32 μm, 0.38H×0.0016H, 112λ×0.47λ) in the wall-normal and in the streamwise directions, respectively, to obtain a mean velocity profile with high wall-normal spatial resolution. Turbulence intensity was obtained from larger windows of 1910×36 pixels (7.65 mm×0.145 mm, 0.38H×0.007H, 112λ×2.1λ) for statistical convergence. Table 3.1 provides all the measurement details and Table 3.2 shows sample images for smooth and riblet cases.

3.1.5 Tomographic particle image velcoimetry

Tomo-PIV measures the three components of flow velocity in a volumetric domain illuminated by an expanded laser sheet. The measurements are potentially suitable for characterization of three-dimensional structures of turbulence, in particular the three-dimensional vorticity field due to a structured data grid. The same laser and camera as the PIV system were used in the tomo-PIV. The collimated laser sheet was expanded to 3 mm in the spanwise direction. The imaging system consisted of four cameras at different angles imaging through a prism filled with water. The prism had four glass windows while each window was parallel to the front surface of the camera objective lens as shown in Figure 3.3. The solid angle between the two outer cameras was set to 80° while the angle between the inner cameras was set to 35°. The cameras were equipped with Scheimpflug adapters and a 105 mm SLR lens with its aperture set at f/16. Magnification and digital resolution were 0.31 and 42.9 voxel/mm, respectively. The measurement volume was 39×20×2.7 mm^3 (1674×859×117 voxel) in the x, y and z directions, respectively. The flow field was seeded with particles at a concentration of approximately 12 particles/mm^3, which was equivalent to a particle density of 0.0175 ppp. The initial mapping function for the tomographic system was carried out using the pin-hole model applied to the images of a two-dimensional target with 0.3 mm dots spaced 2 mm apart in x-y plane. The target

was traversed in the z direction with steps of 1 mm. The rms of the pointing accuracy disparity was reduced by volume-self-calibration technique from an intial value of 1-2 pixels to less than 0.06 pixels in the domain of interest (Wieneke 2008). An ensemble of 4,000 double frame images has been collected for each case with Δt = 1200 μs.

Signal to noise ratio of the images was improved by subtracting minimum intensity of the whole set from individual images followed by normalization using the average of the ensemble. The image quality was further improved using local minimum subtraction with a kernel of 3 pixels, normalization of the intensity using a local average over a kernel of 300 pixels, and a 3×3 pixel Gaussian filter to reduce the peak-locking effect. Finally, a constant value of 20 counts was subtracted from the images to decrease the background noise level to zero. Three-dimensional locations of the particles in 1000 double-frame images were reconstructed using the fast multiplicative algebraic reconstruction (MART) algorithm. The reconstruction volume was 45×27×7 mm^3 (1674×859×117 voxel) in the x, y and z coordinates, respectively. The light intensity distribution across the spanwise depth of the reconstructed volume was used to evaluate the quality of reconstructions. The ratio of the light intensity within the illuminated region to the light intensity outside of the reconstruction was about 3. The relatively high signal to noise ratio was associated with subtraction of 20 counts from the image before reconstruction. The spanwise depth of the illuminated volume based on the reconstructed light intensity was 2.7 mm, compatible with the thickness of the laser sheet. The accuracy of the three-dimensional velocity field against the local mass conservation was shown by estimation of divergence of the velocity field $\nabla \cdot \vec{V}$ about 0.04 voxel/voxel (Scarano et al. 2006). Volumetric cross correlation was performed in multi-pass with the final interrogation volumes of 40×40×40 voxel (0.93×0.93×0.93 mm^3, 0.047H×0.047H×0.047H, 13.7λ×13.7λ×13.7λ) with 75% overlap. Universal outlier detection was used as a post processing step for vector fields (Westerweel and Scarano 2005). Measurement specifications can be found in Table 3.1 and sample images are available in Table 3.2.

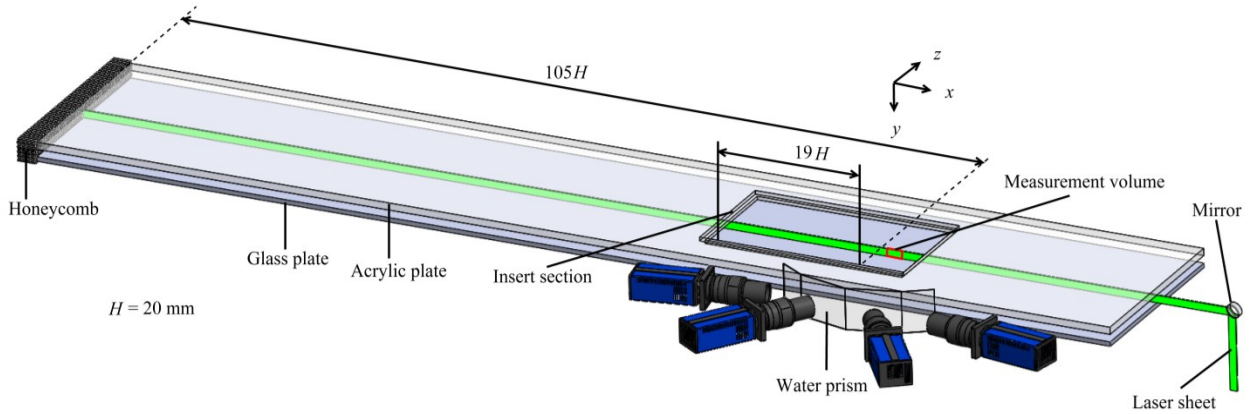

Figure 3.3. A schematic of the experimental setup showing the 2D-channel, the insert module to place the riblet or smooth surface, and tomo-PIV/3D-PTV setup.

3.1.6 Three dimensional particle tracking velocimetry

The 3D-PTV was applied as an alternative of tomo-PIV to obtain the three velocity fluctuaitons with higher spatial-resolution. The drawback of the 3D-PTV relative to tomo-PIV is an unstructured instantaneous data grid which makes it challenging to estimate spatial-gradient based statistics such as vorticity and dissipation. The applied 3D-PTV algorithm (DaVis 8.2, LaVision GmbH) detected and tracked particles based on the triangulation of particles (Wieneke 2008). The algorithm was applied to the same 4,000 double-frame images recorded for tomo-PIV systems using the same mapping function and the self-calibration. The number of detected particles and the noise level were controlled by the particle intensity threshold and allowed triangulation error. The optimum setting for statistical convergence and accuracy was obtained using a maximum triangulation error of 1 pixel and a particle intensity threshold of 300 counts. The detected particle velocities were averaged over bins of 1760×20×12 pixels (41×0.47×0.28 mm^3, 2.0H×0.0235H×0.014H, 600λ×7.0λ×4.1λ) in the x, y and z direction, respectively. Table 3.1 summarizes the specifications of the measurement system.

Table 3.1. System specifications of the measurement setups.

	PIV		Planar PTV		Tomo-PIV	3D-PTV
Ensemble	10,000		15,000		1000	4,000
Magnifi-cation	0.37		1.84		0.31	
Digital resolution	52 pix mm^{-1}		248 pix mm^{-1}		42.9 pix mm^{-1}	
Time interval Δt	1000 μs		190 μs		1200 μs	
Measure-ment field	2023×1224 pix 40.5×23.5 mm^2 $596^+ \times 346^+$		2048×2048 pix 8.2×8.2 mm^2 $121^+ \times 121^+$		1674×859×117 vox 39×20×2.7 mm^3 $574^+ \times 294^+ \times 39.7^+$	1760×859×117 vox 41×20×2.7 mm^3 $603^+ \times 294^+ \times 39.7^+$
Velocity vector	Individual correlation	Ensemble of correlations	Averaged vector field		Individual correlation	Averaged vector field
Interro-gation region (IR)	48×48 pix 0.92×0.92 mm^2 $13.5^+ \times 13.5^+$	16×16 pix 0.31×0.31 mm^2 $4.5^+ \times 4.5^+$	1910×8 pix 7650×32 μm^2 $112^+ \times 0.47^+$	1910×36 pix 7.65×0.145 mm^2 $112^+ \times 2.1^+$	40×40×40 vox 0.93×0.93×0.93 mm^3 $13.7^+ \times 13.7^+ \times 13.7^+$	1760×20×12 vox 41×0.47×0.28 mm^3 $600^+ \times 7.0^+ \times 4.1^+$
IR overlap	75%		0%		75%	0%
Vectors per field	168×102	505×306	256	56	167×85×11	42×9

Table 3.2. Sample images for smooth and riblet wall from each measurement system.

PIV over smooth wall	PIV over riblet wall
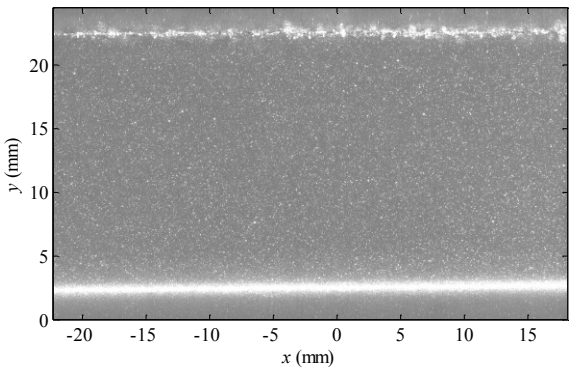	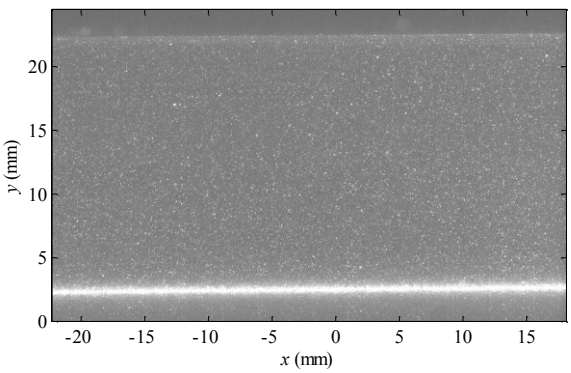
PTV over smooth wall	PTV over riblet wall
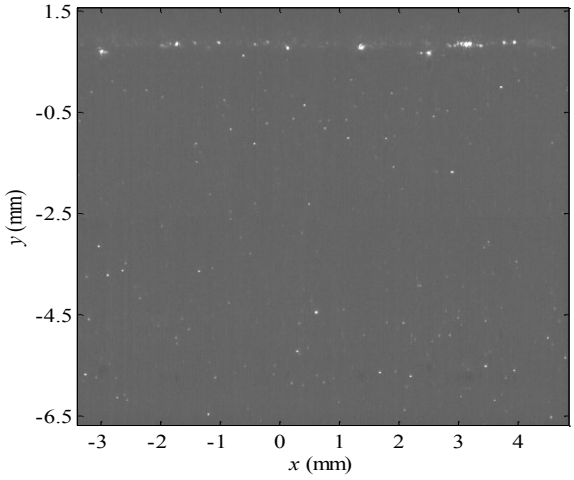	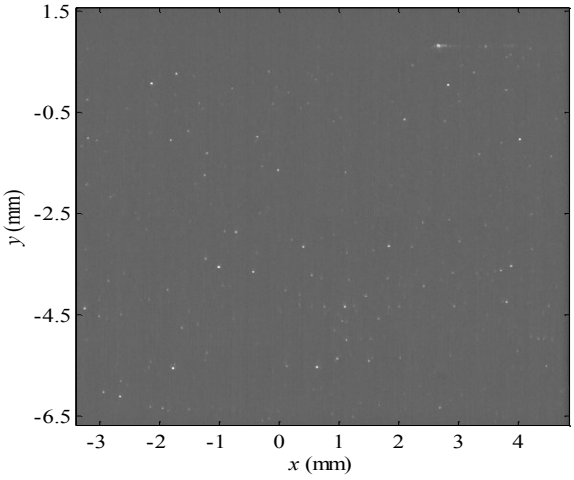
Tomo PIV/3D PTV over smooth wall	Tomo PIV/3D PTV over riblet wall
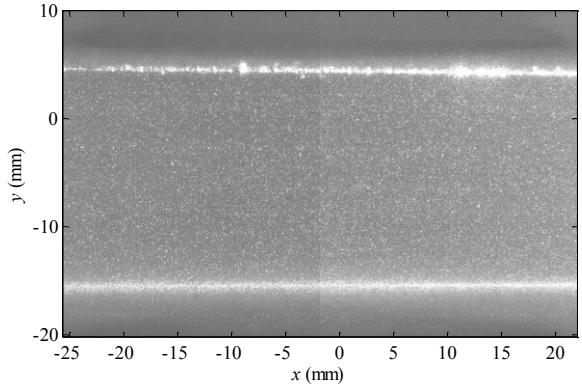	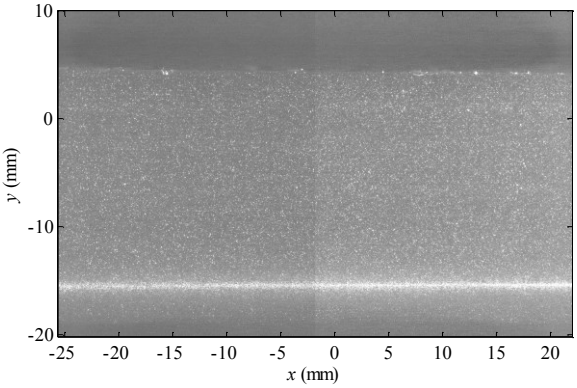

3.2 Planar PIV over riblet surfaces with superhydrophobic coating

3.2.1 Flow facility

The experiments were carried out in a closed-loop, free-surface water channel 5.2 m in length and 0.68 m in width. The test channel was built inside the water channel using a glass plate as the bottom wall and a cast acrylic surface as the top wall. The formed channel was 3 m long (L) in the streamwise direction (x) with a rectangular cross-section of 25 mm (H) in the wall-normal direction (y) and 540 mm (W) in the spanwise direction (z), as shown in Figure 3.4. To avoid the influence of the free surface and spanwise flow, the sides of the channel were sealed with foam. Only a 4 cm slot was kept at the measurement location to permit the access for PIV image capturing. At the entrance of the channel, a honeycomb was placed to break large vortices and straighten the flow. Measurements were performed over test surfaces inserted in the interchangeable module. The module with dimensions of 570 mm length and 320 mm width was located 1.9 m (76H) downstream of the channel entrance to ensure fully developed turbulent flow. Large turbulent length scales in this facility due to the low velocity and relatively large channel height, eased manufacturing of the riblets with required scaling. This also increased measurement accuracy in the near wall region. Instantaneous velocity and fluctuating velocity in the x, y and z directions are denoted as U, V, W and u, v, w, respectively. The bulk velocity across the channel in the y direction was $U_b = 0.176$ m/s corresponding to $Re_H = 4380$ based on a channel height H and a kinematic viscosity $\upsilon = 1.004\times10^{-6}$ m^2/s. Blasius' law for the friction coefficient c_f in a turbulent pipe flow is

$$c_f = 0.0791 \left(\frac{U_b d}{\nu}\right)^{-1/4}, \tag{3.1}$$

where d is the equivalent hydraulic diameter defined as

$$d = \frac{4a}{c}, \tag{3.2}$$

where a is the channel cross-section area and c is the wetted perimeter (Schlichting and Gersten 2000). For the cross-section in the current study, d was found to be $d = 0.048$ m. The friction coefficient was calculated using Equation (3.1). Friction velocity and wall units were estimated to be $u_\tau = 0.0113$ m/s and $\lambda = 88.7$ μm, respectively. The friction Reynolds number was $Re_\tau = 141$ based on friction velocity and half channel height.

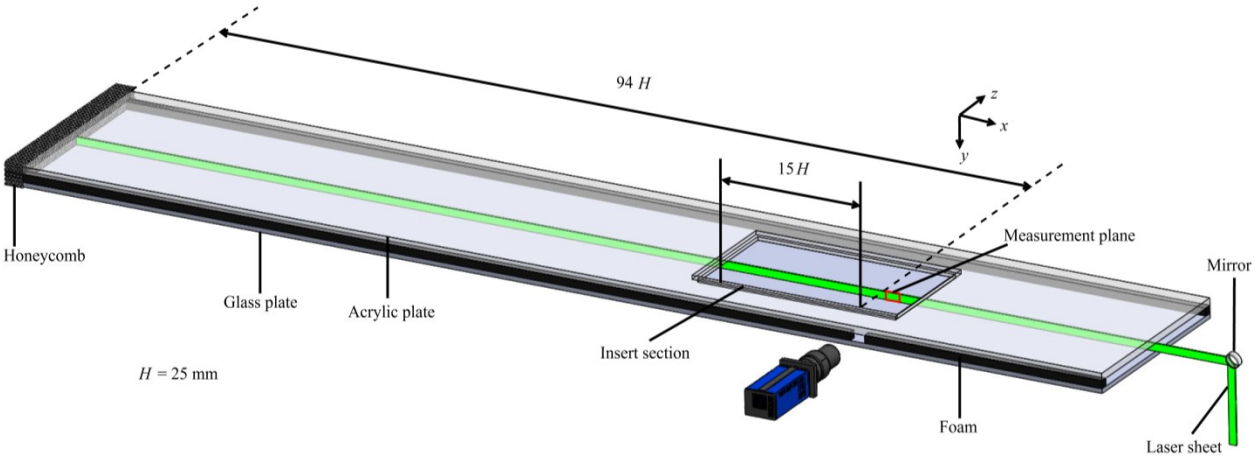

Figure 3.4. A schematic of the experimental setup showing the 2D-channel, the insert module to place the riblet or smooth surface, and the PIV measurement setup.

3.2.2 Non-coated smooth and riblet surfaces

Four test surfaces with dimensions of 430 mm long, 280 mm wide and 6.35 mm thick were made of cast aluminum. One surface was kept smooth to serve as reference. Trapezoidal riblets of three different sets of dimensions were machined on three test surfaces by CNC milling with 12.7 μm tolerance. Their dimensions are listed in Table 3.3 as well as the SFR performances predicted by Bechert et al. (1997). Test surfaces were inserted into the interchangeable module. Same as the methods in section 3.1.2, riblet surfaces were placed such that two fifths of the height of the riblet tip protruded in the channel flow

Table 3.3. Properties of the tested trapezoidal riblets.

	s^+	s	h	α	Expected SFR
1	8.5	750 μm	375 μm	30°	5%
2	17	1500 μm	750 μm	30°	8%
3	34	3000 μm	1500 μm	30°	-5%

3.2.3 Coated smooth and ribelt surfaces

The difficulty in fabrication of patterned SHSs has limited its application in large scale equipment. On the contrary, SHSs with random texture can be fabricated through spray coating easily. In the current study, SHSs comprised of a hierarchy of micro and nano-particle structures were prepared on the four plates with riblets (detailed in section 3.2.2) using spray coating (Rust-Oleum NeverWet). Bidkar et al. (2014) has shown SFR over SHSs when the surface roughness of a SHS is an order of magnitude smaller than the thickness of the viscous sublayer. In the present study, the thickness of the viscous sublayer was estimated to be 460 μm. Thus the

coating procedure was designed to generate the surface roughness to be around 40 μm. Before the two-step coating procedure, the surfaces were cleaned with ethanol for better adhesion of the coating (Vajdi Hokmabad and Ghaemi 2016). An acrylic–based polymer solution working as a binding layer on the aluminum substrate was formed over the surface by spraying 4 passes uniformly. Each pass refers to the spraying from either left to right or top to bottom of the test plate once. After leaving the solvent for about 30 min to evaporate, 3 passes of top coat containing nano-particles in ethanol was applied over the base coat. The surface was kept overnight for further drying before testing in the channel. The images of the riblets after coating are shown in Figure 3.5. The thickness of coating at the two sides of a riblet meets the requirement of a thickness of 40 μm but the coatings at the valley and the tip regions are a little thicker in the case of $s^+ = 8.5$.

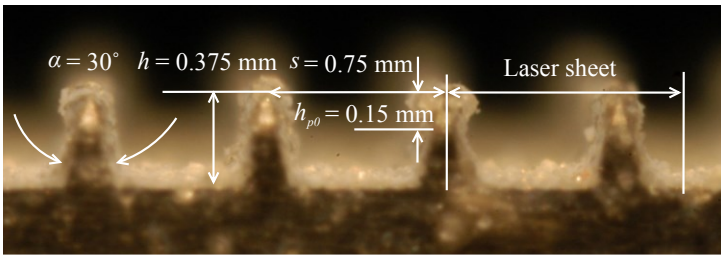

(a)

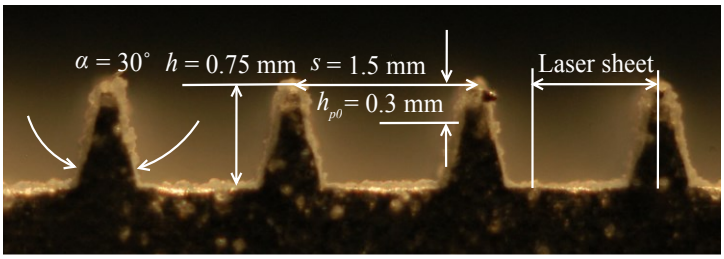

(b)

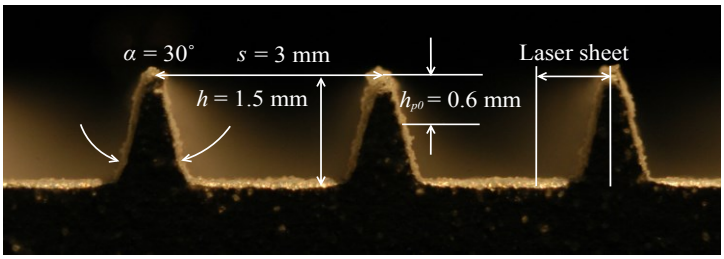

(c)

Figure 3.5. Images of the cross-section of the riblets with superhydrophobic coatings: (a) $s^+ = 8.5$, (b) $s^+ = 17$, (c) $s^+ = 34$.

3.2.4 Particle image velocimetry

A planar PIV system was applied to characterize turbulent flow fields across the whole channel height at a magnification of $M = 0.2$. Polyamide 12 fine powder (VESTOSINT 2070) with an average diameter of 5 μm and density of 1.016 g/cm^3 was added as tracer particles. The illumination was provided by an Nd:YAG laser (Spectra-Physics, PIV400) with 532 nm wave length, a maximum output of 400 mJ per pulse and a maximum repetition rate of 10 Hz. A collimated laser sheet of approximately 1 mm thickness was formed using a combination of spherical and cylindrical lenses and directed by a mirror sealed in an acrylic column downstream of the channel, to enter the channel in the streamwise direction, as shown in Figure 3.4. Such a wall-paralleled laser sheet could reduce wall reflection of the laser sheet in the PIV images. The thin laser sheet covers a full riblet from tip to tip over the riblet surface of $s^+ = 8.5$ ($s = 0.75$ mm). In the case of $s^+ = 17$ ($s = 1.5$ mm) and $s^+ = 34$ ($s = 3$ mm), the laser sheet was not wide enough

to cover the whole riblet region. The covered region of a riblet at $s^+ = 17$ was still able to provide an averaged effects of different riblet parts (for example, tip and valley) on the turbulent flows, since the covered region counted two thirds of the whole riblet region. However, in the case of $s^+ = 34$, the laser sheet covered only the area starting from the midpoint between the riblet tip and the valley and ending at the valley, as shown in Figure 3.5 (c). The scattered light from tracer particles was collected by a CCD camera (Imager Intense, LaVision GmbH) with sensor size of 1376×1040 pixel, a pixel size of 6.45×6.45 μm^2 and 12-bit resolution. The camera was equipped with a 105 mm Nikkor SLR lens at aperture size of *f*/8. The camera setup was shown in Figure 3.6. The digital resolution and depth of field (DOF) were 30 pix/mm and 4.9 mm, respectively. The field of view (FOV) was 45.6 mm×28.6 mm extended to 5 mm upstream of the end of the test surface (94*H* from the channel entrance and 15*H* from the leading-edge of test surface). The camera frames and laser pulses were synchronized by a programmable timing unit (LaVision GmbH) controlled by DaVis 7.4. An ensemble of 8,000 images over each test surface (both non-coated and coated) was recorded with a pulse separation of $\Delta t = 3300$ μs. Figure 3.6 shows the optical path of the laser along the streamwise direction of the channel during experiments.

The images were first improved by subtracting the minimum intensity of the ensemble from the individual image and further processed by normalizing each image with the ensemble average. A cross-correlation algorithm was performed over the double-frame images with a final window size of 48×48 pixels (1.6 mm×1.6 mm, 0.064*H*×0.064*H*, 17.3λ×17.3λ) with 75% overlap. The vector fields were post-processed by filtering vectors out of 0 to 26 pixels for the streamwise displacement and -4 to 4 pixels for the wall-normal velocity and by universal outlier detection (Westerweel and Scarano 2005). The double frame images were also processed with the ensemble of correlation method (EC method) (Meinhart, Wereley, and Santiago 2000). The final window size in the EC method was 24×24 pixels (0.8 mm×0.8 mm, 0.032*H*×0.032*H*, 9.0λ×9.0λ) with 75% overlap. All the processing was conducted in DaVis 8.2 (LaVision GmbH). The measurement configurations are summarized in Table 3.4 and sample images over different test surfaces are provided in Table 3.5.

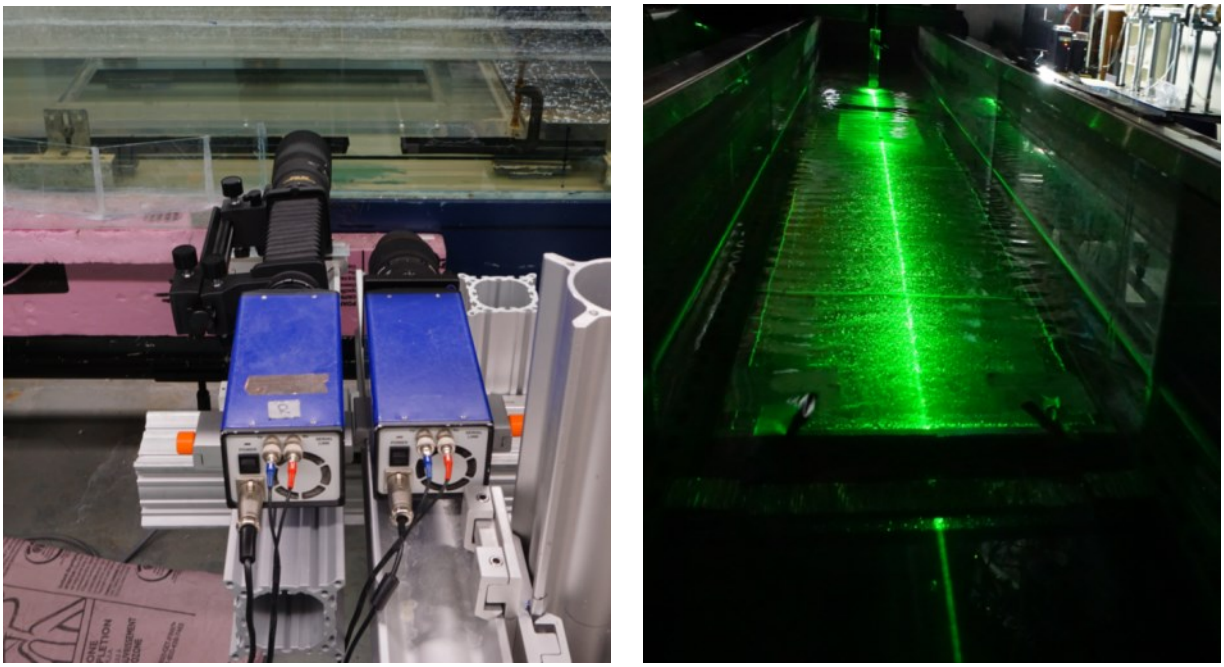

(a) (b)

Figure 3.6. (a): The imaging system showing the PIV camera on the right side, (b): The laser sheet along the channel during image capturing.

Table 3.4. System specifications for planar PIV measurement

	PIV	
Ensemble	8000	
Magnification	0.2	
Digital resolution	30 pix mm^{-1}	
Time interval	3300 μs	
Measurement field	1376×864 pix 45.6×28.6 mm^2 $494^+ \times 310^+$	
Velocity vector	Individual correlation	Ensemble of correlation
Interrogation region (IR)	48×48 pix 1.6×1.6 mm^2 $18.0^+ \times 18.0^+$	24×24 pix 0.8×0.8 mm^2 $9.0^+ \times 9.0^+$
IR overlap	75%	
Vectors per field	104×63	200×126

Table 3.5. Sample particle image velocimetry images over different test surfaces showing different level of wall reflection of the laser sheet

Smooth wall	Smooth wall coated with superhydrophobic layer
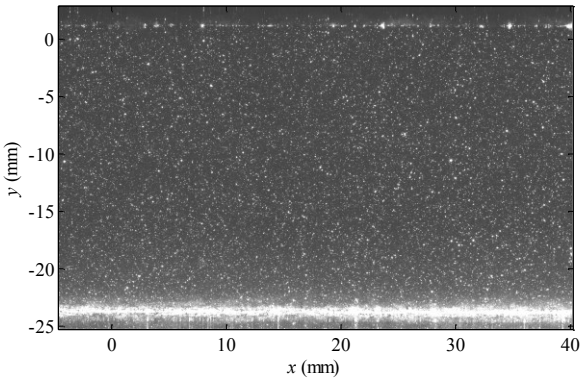	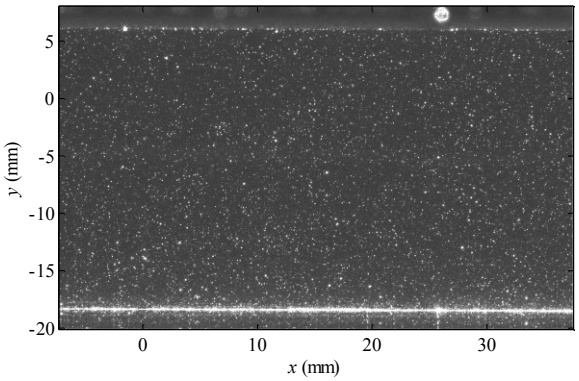
Riblet wall	Riblet wall coated with superhydrophobic layer
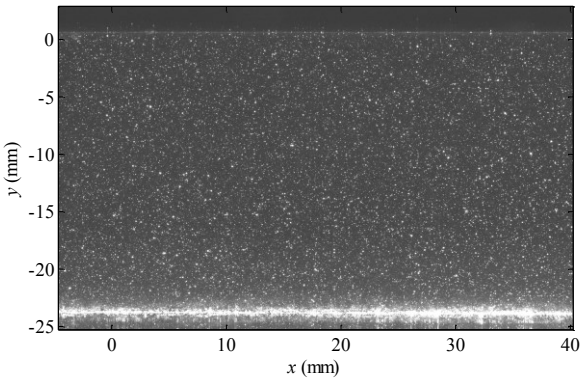	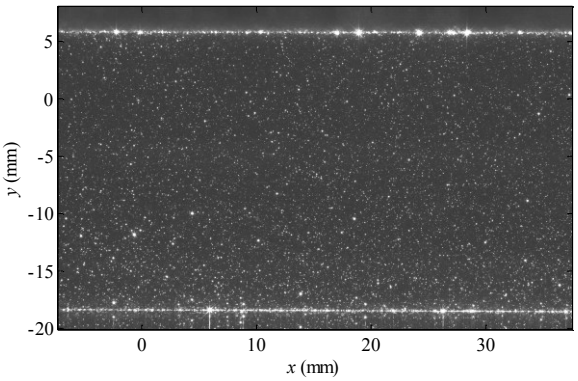

Chapter 4. Evaluation of 2D/3D particle image velocimetry and particle tracking velocimetry

4.1 Introduction

A limited amount of PIV/PTV investigations has been carried out in the literature to investigate the turbulent flows over surfaces with riblets by virtue of the challenges including capturing the turbulent changes of small scale precisely and heavy calibration and image processing procedures in three-dimensional measurements.

Roggenkamp et al. (2015) derived the SFR performance on a spanwise traveling surface by calculating the friction velocity from the mean velocity profile in the viscous sublayer measured by a micro-PTV. Yang et al. (2015) reported an increase of the boundary layer thickness over riblets with a time-resolved PIV. The attenuation of the velocity fluctuations have been characterized by Sasamori et al. (2014), Lee and Lee (2001) and Lee and Choi (2008) using planar PIV and by Suzuki and Kasagi (1994) with 3D-PTV. At the same time, Sasamori et al. (2014) with planar PIV and Suzuki and Kasagi (1994) with 3D-PTV have noticed the reduced Reynolds shear stress over riblet surfaces. Regarding the observations of the three-dimensional vortices over riblet surfaces, planar PIV has provided the profile of the spanwise vorticity in the streamwise and wall-normal measurement plane (Sasamori et al. 2014) and distribution of the streamwise vorticity in the wall-normal and spanwise measurement plane (Lee and Lee 2001).

In these studies, the effects of riblets on the skin-friction were investigated by a single measurement technique and the three-dimensional measurements were rare. They focused on acquiring the changes of the turbulent statistics without explicitly discussing about the measurement accuracy of the PIV/PTV systems in capturing turbulent flows over the millimeter-sized riblets.

The present work evaluates the capabilities of planar and volumetric PIV and PTV techniques in resolving the near-wall turbulent structure over riblet surface at $Re_\tau = 147$. 2D-PIV, long-range micro-PTV, tomo-PIV, and 3D-PTV are applied to measure mean velocity, Reynolds stresses, two-point correlation, and vorticity components. The evaluation of the measurement techniques is carried out in comparison with the previous experimental and numerical works over riblet

surfaces and also by carrying out measurements over a reference smooth surface. The smooth plate measurements are further validated using DNS over smooth wall channel flow by Tsukahara et al. (2005) at $Re_\tau = 150$.

4.2 Results and discussion

4.2.1 Virtual origin and protrusion height

The protrusion height (h_{p0}) of a riblet surface is defined as the wall-normal distance from the riblet tip to a virtual origin which is the wall-normal position where an imaginary smooth surface generates the same outer layer velocity profile as the riblet surface (Choi, Moin, and Kim 1993; Duan and Choudhari 2012). The virtual origin of riblets has been evaluated by several approaches in the literature. Perry and Joubert (1963) applied an extension of the Clauser's method to estimate the virtual origin and friction velocity over a rough wall (with SFI) by assuming a universal wake function in the outer edge of the velocity profile. Hooshmand et al. (1983) checked the feasibility of this method to a riblet surface (with SFR) and observed an erroneous virtual origin resulting in SFI relative to the smooth surface. Instead, they applied extrapolation of the velocity profile over the riblet valley in the linear region to find the virtual origin at $<U> = 0$. Their extrapolation showed a virtual origin almost at the midpoint between the tip and the valley of the riblet in the wall-normal direction. Choi, Moin, and Kim (1993) used the wall normal shift of the location of maximum streamwise velocity fluctuation to estimate the virtual origin in their DNS study. However, neither the method from Hooshmand et al. (1983) nor from Choi, Moin, and Kim (1993) is suitable to direct the design of riblets, as the virtual origin can only be calculated after acquiring the velocity profile. At the same time, it is difficult to access to the velocity profile in the riblet valley for the calculation. Bechert and Bartenwerfer (1989) applied a conformal mapping by assuming linear viscous region existing inside the viscous sublayer where riblets are immersed. The velocity profile at the riblet tip or valley was extrapolated linearly to reach zero at the virtual origin (see Figure 3 in Bechert and Bartenwerfer 1989). They analytically predicted virtual origins as a function of the shape and geometric height of riblets. Following the database they provided, Bechert et al. (1997) have managed SFR tests over riblets of various geometric parameters. Furthermore, locations of virtual origin calculated from conformal mapping and method of Choi, Moin, and Kim (1993) agree with each other (Duan and Choudhari 2012).

In the current investigation, the conformal mapping method is used to estimate the theoretical virtual origin and protrusion height h_{p0} of the riblets during design and mounting of riblet test surface. Bechert and Bartenwerfer (1989) showed the protrusion height to be $h_{p0} = 0.2s$, which means $h_{p0} = 0.15$ mm, two fifth of the riblet height, for the riblet geometry chosen.

Analysis of Bechert and Bartenwerfer (1989) were based on a number of complete riblets. In the current setup, the laser sheet with 1mm thickness covers about 1.3 riblets. Due to the random location of the extra 0.3 riblets, the real virtual origin and protrusion height h_p obtained by extrapolation of velocity profile above the riblet tip might differ from h_{p0}. Though such difference has been proven to not lead to a significant variation in the turbulent statistics when the value fluctuated around 30% (see Table 3 and Figure 8 in Choi, Moin, and Kim 1993), the real virtual origin will be calculated from the near wall velocity profile in Figure 4.2 and used as the start point for all the plots except Figure 4.2 for better comparison.

For the riblet case, the top wall ($y / H = 0$) corresponds to the riblet wall at the calculated real virtual origin while the bottom wall at $y / H = 1.0$ is always the smooth wall opposite to the interchangeable test section. Available DNS study of turbulent channel flow with $Re_\tau = 150$ by Tsukahara et al. (2005) is provided as references.

4.2.2 Mean velocity profile

The mean streamwise velocity normalized by the bulk streamwise velocity U_b of each individual case (smooth or riblet) across the channel measured using PIV (from EC method) is shown in Figure 4.1. The near wall data are difficult to be obtained due to the lower tracer particle density as well as the large velocity gradient in the vicinity of the wall. In the bottom section of the channel ($y / H > 0.5$), it is seen that the velocity profiles on both surfaces overlap with each other, showing the accuracy of the measurement and the flow setup. In the top section of the channel ($y / H < 0.5$), the velocity in the riblet case is larger.

Planar PTV fulfills the shortcoming of the PIV measurement by providing higher spatial-resolution in the near wall region, as shown in Figure 4.2. The velocity profile of each surface is normalized with the corresponding friction velocity. In order to calculate the intercept at $U^+ = 0$, which represents the location of the virtual origin, the origin of the riblet data ($y_t^+ = 0$) is set at the riblet tip. The intercept at $U^+ = 0$ is located at 0.12 mm, which is a 20% difference from 0.15 mm. For the smooth case, the velocity goes to zero at the wall because of the no-slip boundary condition. The black lines show a linear fit based on the velocity gradient $\frac{\partial \langle U \rangle}{\partial y} \frac{\nu}{u_\tau^2}$ in the range of $2 < y^+ < 5$. The coefficient of determination R^2 is larger than 0.995 when performing the fitting. The estimated friction velocity and wall units are $u_{\tau 0} = 0.0148$ m/s and $\lambda_0 = 67.9$ μm over

the smooth wall while $u_{\tau r} = 0.0139$ m/s and $\lambda_r = 72.3$ μm above the riblet surface. The friction velocity and the wall units are also calculated over the smooth wall using an empirical equation from Dean (1978) as a reference. The estimated values are $u_{\tau 0,Dean} = 0.0146$ m/s and $\lambda_{r,0Dean} = 68.5$ μm, in good agreement with the measured values. The slope of the lines show a 6.1% reduction of $\partial <U> / \partial y$ and consequently the wall shear stress (τ_w) above the riblet surface following

$$\tau_w = \rho \nu \frac{\partial <U>}{\partial y}, \tag{4.1}$$

SFR with riblets with the same geometry have been tested between $Re_H = 10000 \sim 33000$ by Bechert et al. (1997) and 6% SFR was observed at $s^+ = 11$ with weak dependence on Reynolds number. The estimated reduction of τ_w is close to the value of 6% measured by them. The same method has been used to estimate friction velocity over the riblet surface by Park and Wallace (1994) with hot wire data and Roggenkamp et al. (2015) with micro-PTV data.

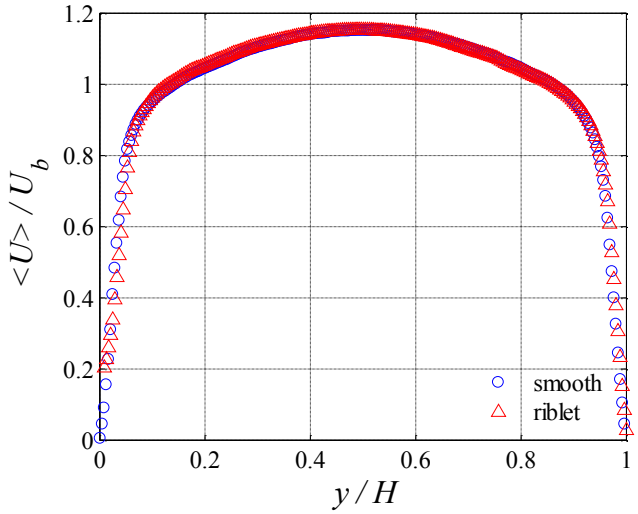

Figure 4.1. Normalized velocity with U_b from PIV measurement processed using ensemble of correlation method with 16 × 16 window size and 75% overlap.

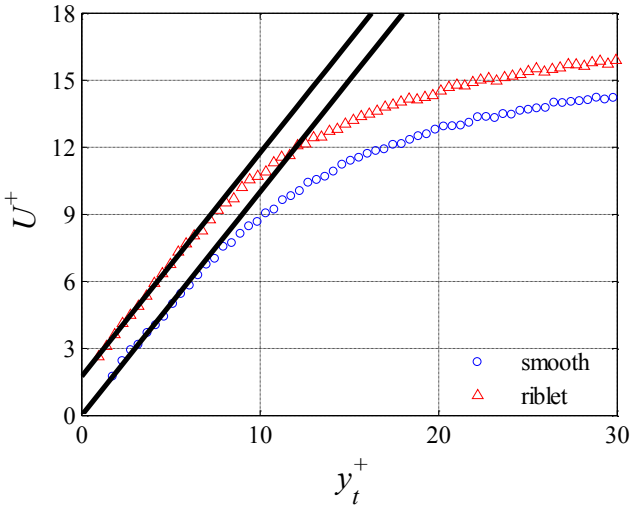

Figure 4.2. Velocity profile measured using long range microscopic PTV normalized by the friction velocity of the corresponding surface.

A semilog plot of the mean velocity versus the wall-normal distance normalized by inner scaling of the corresponding surface is shown in Figure 4.3. In the linear viscous sublayer, both velocity profiles follow the law of the wall $y^+ = u^+$. The data of the smooth wall overlaps with the logarithmic law with $\kappa = 2.5$ And $B = 5.5$. The slope of the log law (κ) over the riblet wall is the same as that of the smooth wall. However, the intercept (B) over the riblet surface is larger and equal to 7.2. A similar trend has been observed by Hooshmand et al. (1983), Choi, Moin, and Kim (1993) and Lee and Choi (2008) over riblet surfaces. Lumley (1973) interpreted the upward shift of the log law as the symbol of a thicker viscous sublayer.

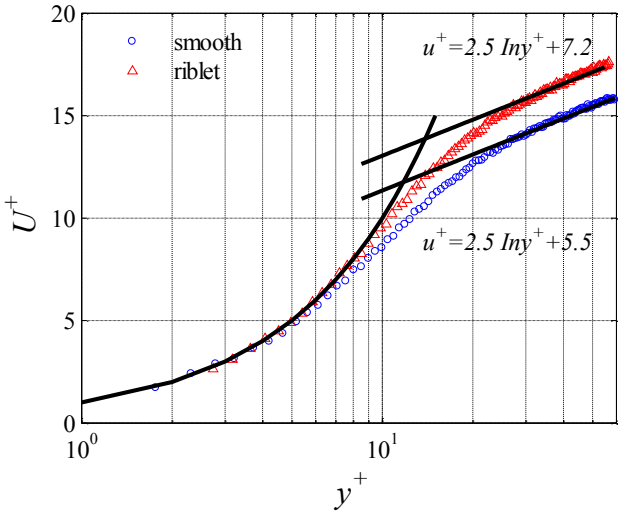

Figure 4.3. Semi-logarithmic plot of mean velocity using long-range microscopic PTV. The data over each surface is normalized using the corresponding inner scaling.

4.2.3 Turbulence intensities

The normalized streamwise velocity fluctuation from PIV is provided in Figure 4.4. The lack of spatial-resolution brings about significant errors in the first few near-wall vectors. The PIV system is not able to capture the $<u^2>$ peak over the smooth surface. The monotonic increase in $<u^2>$ in the vicinity of the wall over the smooth surface is associated with the mirrored image of the particles due to a smaller level of light reflection in the vicinity of the smooth wall ($y / H < 0.05$). However, the riblet surface has a stronger wall reflection, which imposes an artificial no-slip boundary condition for the PIV correlation. The result is a near-wall reduction of velocity and the appearance of a $<u^2>$ peak over the riblet surface. Away from the peak, $<u^2>$ profiles of the smooth surfaces agree well with the DNS. The intensities over the bottom smooth wall ($y / H > 0.5$) for the two cases overlap. In the top half channel from $y / H = 0$ to $y / H = 0.5$, the value of $<u^2>$ has been attenuated over the riblet wall. Such attenuation up to the channel center is also observed in the data from Choi, Moin, and Kim (1993) and Suzuki and Kasagi (1994), although not explicitly discussed. The near-wall measurement of $<u^2>$ with higher spatial-resolution is available using PTV in Figure 4.5. The normalized peak value of $<u^2>$ is about 8.1, and located at $y^+ = 13$ over the smooth wall. It has a 12.5% discrepancy with respect to the DNS of Tsukahara et al. (2005) with a normalized peak of 7.2. The PTV results show a 5.9 % reduction of the $<u^2>$ peak and a slight shift of the peak away from the wall to

$y^+ = 15$, over the riblet surface. This indicates a thicker viscous sublayer. This slight shift in the peak location also helped PIV to capture the peak in Figure 4.4.

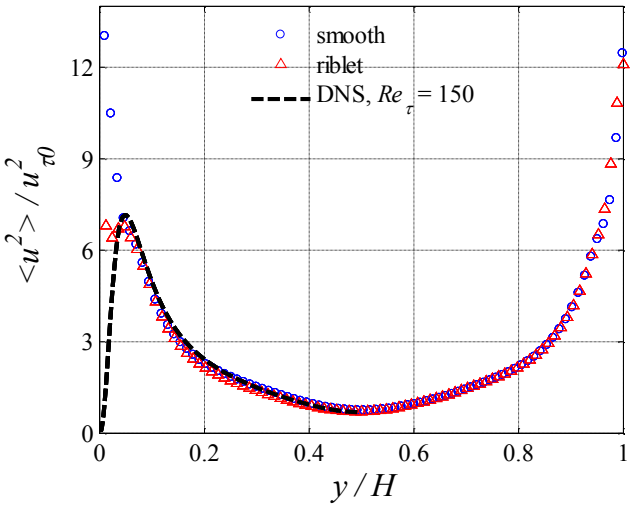

Figure 4.4. Streamwise velocity fluctuation ($<u^2>$) from PIV measurement normalized using $u_{\tau 0}$ of the smooth wall.

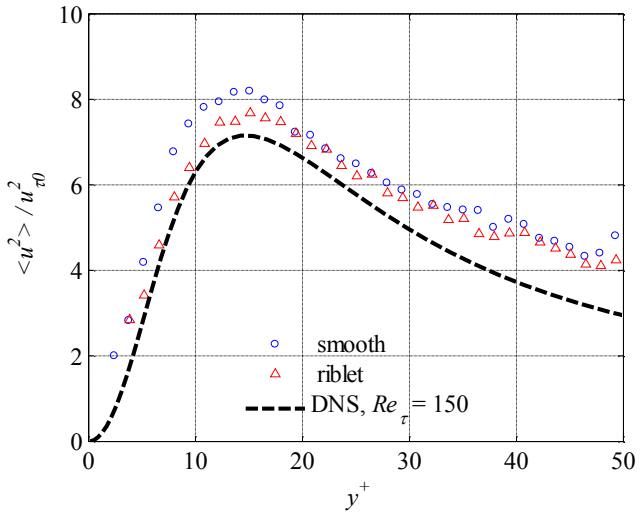

Figure 4.5. Streamwise velocity fluctuation ($<u^2>$) from planar PTV measurement normalized using $u_{\tau 0}$ of the smooth wall.

The normalized wall-normal velocity fluctuation from PIV results is shown in Figure 4.6. The peak value of $<v^2>$ over the smooth surface at $y^+ = 47$ is higher than that of DNS, which reduces towards the channel centerline. The largest measurement errors occur in the near wall region, are calculated to be 0.24 pixels. The profile for the smooth case in the present experiment is symmetric with less than a 2% difference in peak values, showing the reliability of the data.

There is a 9.4% reduction of $<v^2>$ peaks over the riblet wall and the peak location is shifted away from the wall to $y^+ = 49$ similar to the $<u^2>$ peak. Note the difference between the peaks near the bottom wall ($y / H = 1$) could be a result of flow development in the channel as a result of the $<v^2>$ reduction over the riblet wall.

The spanwise velocity fluctuation from 3D-PTV measurements is provided in Figure 4.7. 3D-PTV is applied for this measurement due to its higher spatial-resolution relative to tomo-PIV. The measurement over the smooth wall is symmetric and overlaps with the bottom wall profile ($y / H > 0.5$) of the riblet case. The measured $<w^2>$ is higher than in the DNS, with the largest error estimated to be about 0.34 pixels. The peak location from the 3D-PTV is at $y / H = 0.1$ (equivalent to $y^+ = 31$) which is slightly different from the $<w^2>$ peak of DNS. The peak value reduces by 9.4% over the riblet surface according to the 3D-PTV measurement.

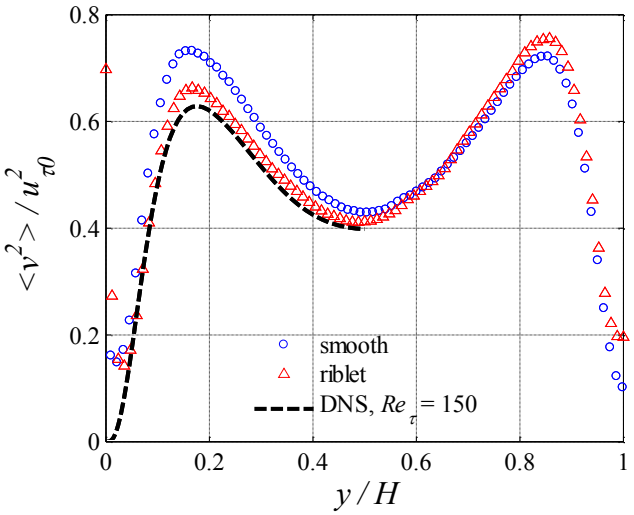

Figure 4.6. Wall-normal velocity fluctuation ($<v^2>$) from PIV measurement normalized using $u_{\tau 0}$ of the smooth wall.

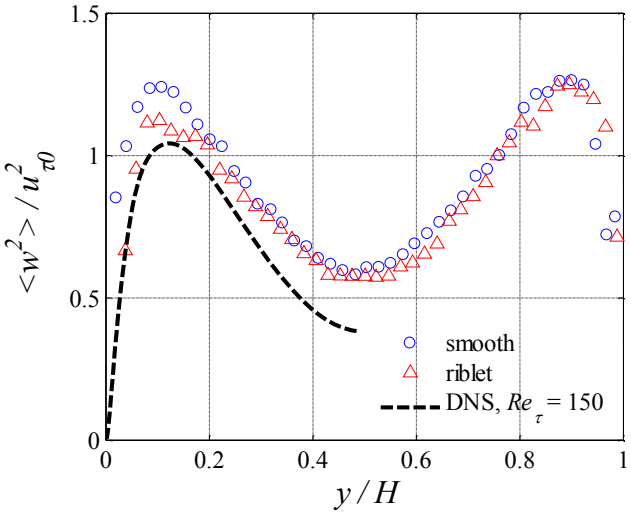

Figure 4.7. Spanwise velocity fluctuation ($<w^2>$) from 3D-PTV measurement normalized using $u_{\tau 0}$ of the smooth wall.

Peaks of all components of turbulence intensities over the smooth wall, from current study at $Re_\tau = 147$ are higher compared to the DNS of Tsukahara et al. (2005) at $Re_\tau = 150$. This is a consequence of measurement noise. Choi, Moin, and Kim (1993) and Suzuki and Kasagi (1994) have recorded reductions of three components of velocity fluctuations by riblets in the DNS and the 3D-PTV study, respectively. Choi, Moin, and Kim (1993) calculated the reduction of $<u^2>$, $<v^2>$ and $<w^2>$ to be 5%, 10% and 10%, respectively.

The normalized Reynolds shear stress from the PIV measurements is presented in Figure 4.8. The intercept of the $<uv>$ data with $y / H = 0$, based on extrapolation of linear fit on $0.2 < y / H < 0.5$ data, is used to estimate the wall shear stress. The results show a 7.4% reduction of wall shear stress over the riblet surface, which is in good agreement with the result of a 6% reduction observed by Bechert et al. (1997) and also with a 6.1% reduction estimated using the slope of the linear viscous sublayer from Figure 4.2. For the change of peak values, an 11% reduction is noticed in the present study. Choi, Moin, and Kim (1993) reported a 12% reduction and Suzuki and Kasagi (1994) showed the reduction to be 15%.

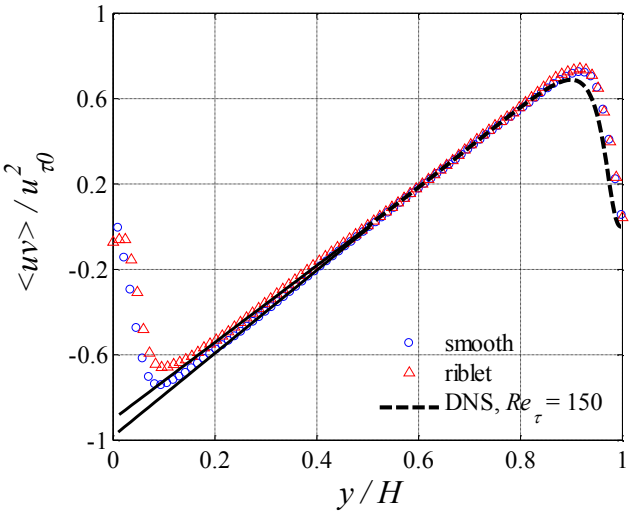

Figure 4.8. Reynolds shear stress (<*uv*>) from PIV measurement normalized using $u_{\tau 0}$ of the smooth wall. The solid lines show linear fit over the data with the range of $0.2 < y / H < 0.5$.

4.2.4 Quadrant analysis

The riblet surface alters the rate of energy transfer in the near wall region (Kasagi et al. 1995). The quadrant analysis provides detailed information on positive and negative *u* and *v* fluctuations and their correlation for turbulent production Willmarth and Lu (1972). The four quadrants are defined as Q1 ($u > 0$ and $v > 0$), Q2 ejection ($u < 0$ and $v > 0$), Q3 ($u < 0$ and $v < 0$) and Q4 sweep ($u > 0$ and $v < 0$). The Reynolds shear stress is conditionally averaged based on the quadrant of the fluctuations following

$$uv_{con} = <uv>|_{Q1,\ Q2,\ Q3,Q4} \tag{4.2}$$

The normalized conditional averaged Reynolds shear stress is given in Figure 4.9. The magnitude of the sweep and ejection reaches the same level at about $y^+ = 16$ over the smooth case. This is in accordance with the conclusion of Wallace, Eckelmann, and Brodkey (1972) that the sweep and ejection have the same contribution to the Reynolds shear stress at $y^+ \sim 15$. In addition, the trends of sweep and ejection are in agreement with the description that the ejection and sweep are major contributors to the Reynolds shear stress away from the wall and near the wall, respectively (Kim, Moin, and Moser 1987). The first and third events stay nearly the same over the two surfaces and make a small negative contribution to turbulent production, which coincide with the observations of Choi, Moin, and Kim (1993). The ejection and sweep events

over the riblet surface are attenuated, in association with the dampening of the strength of the streamwise vortices present in the near-wall region (Robinson 1991; Choi, Moin, and Kim 1993). The all four events have been shifted slightly away from the wall in riblet case. The suppression of the sweep and ejection events is also valid in Choi, Moin, and Kim (1993) and Sasamori et al. (2014).

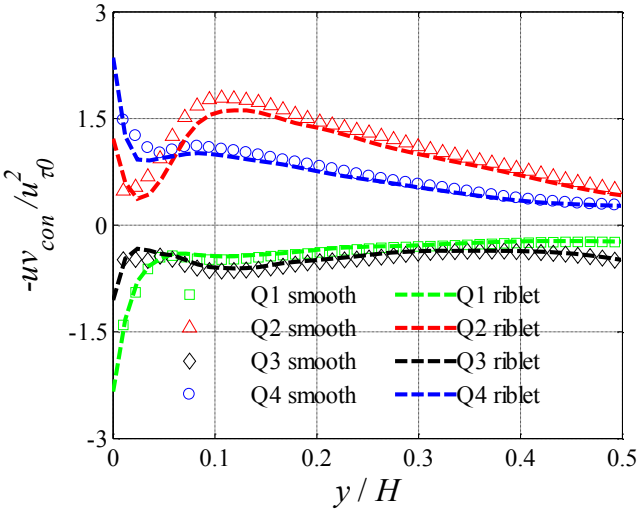

Figure 4.9. Amplitude of each quadrant of Reynolds shear stress from PIV measurement normalized using $u_{\tau 0}$ of the smooth wall.

The fact that riblet SFR is due to the suppression of streamwise vortices leads to new quadrant analysis ideas: a combination of positive and negative v and w. Compared to the streamwise velocity component, wall-normal and spanwise velocities are more related to the changes of streamwise vortices movements. Therefore the distributions of v and w should be altered by the riblets. The quadrant distribution of v and w at $y^+ = 6$ from 3D-PTV are presented in Figure 4.10. As is seen, the areas of contour in all three levels are reduced over the riblet surface, and the reduction is averaged in each quadrant. This indicates that both the strength of v and w over the riblet surface are much weaker. The observation is consistent with the damped motions of streamwise vortices. Note that the distribution of v and w is symmetric with respect to zero axis.

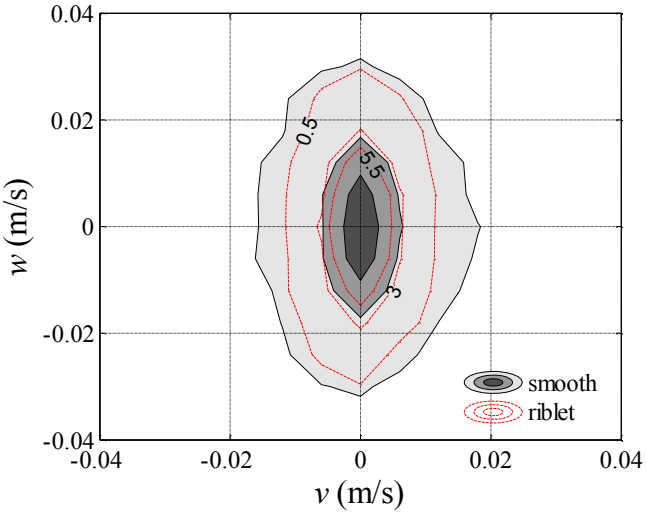

Figure 4.10. Probability density function of wall-normal (v) and spanwise (w) velocity fluctuation from 3D-PTV measurement at $y^+ \approx 6$. The filled contours in dark gray, medium gray and light gray, along with the red dash-line contours from inner circle to outer circle denote 5.5%, 3.0% and 0.5% probability density function values, respectively.

4.2.5 Vorticity

The normalized root-mean-square of vorticity fluctuation is defined as

$$\omega_i^+ = \sqrt{<\omega_i^2>} v / u_{\tau 0}^2. \tag{4.3}$$

Here, i refers to the vorticity components (i.e., ω_x, ω_y, and ω_z). PIV provides relatively accurate measurement of ω_z^+ using first order central difference scheme, as shown in Figure 4.11. ω_z^+ slightly decreases up to $y^+ = 100$ over the riblet wall and then is the same as ω_z^+ on the smooth wall. This trend agrees with the result of Sasamori et al. (2014). Near the channel center, ω_z^+ is overestimated compared to the DNS. In order to calculate the velocity gradient from tomo-PIV data, a second order regression is applied to reduce the measurement noise (Elsinga et al. 2010). The function

$$\begin{aligned} f_{reg}(r_x, r_y, r_z) = a_0 + a_1 r_x + a_2 r_y + a_3 r_z + a_4 r_x r_y + a_5 r_x r_z \\ + a_6 r_y r_z + a_7 r_x^2 + a_8 r_y^2 + a_9 r_z^2 \end{aligned} \tag{4.4}$$

is fit to each velocity fluctuation component in a 5×5×1 neighborhood of a point x, y, z, where r_x, r_y, r_z are the relative distances in the x, y and z direction to the point and coefficients a_i are the fit parameters with a_1, a_2, a_3 being the local gradients in the x, y and z direction, respectively (Elsinga et al. 2010). To keep the spatial frequency response of the cross-correlation (75%

overlap) and the regression the same, the kernel size 5×5 was applied in the *x*-*y* plane (Elsinga et al. 2010). However, limited by the amount of *z* plane data, the kernel size of 1 was taken in the z direction. Figure 4.12 shows the vorticities from the tomo-PIV results. No obvious differences between two cases are observed. The vorticities over riblet surface are even slightly larger than those over smooth surface. Choi, Moin, and Kim (1993) numerically showed a marginal reduction for vorticity fluctuations on the riblet wall, therefore it is reasonable to obtain the same level of vorticity in both cases. El-Samni, Chun, and Yoon (2007), on the contrary, reported an increase of ω_y^+ and ω_z^+ in the range of $20 < y^+ < 75$ on riblets. In the midsection of the channel, all three vorticity components should overlap as the DNS data shows. However, the tomo-PIV data show larger values for all components and in particular for ω_x^+ and ω_y^+, due to the higher measurement noise of the out-of-plane velocity components. Worth, Nickels, and Swaminathan (2010) simulated the measurements of tomo-PIV and showed at least 45% measurement uncertainty related to velocity gradient fields.

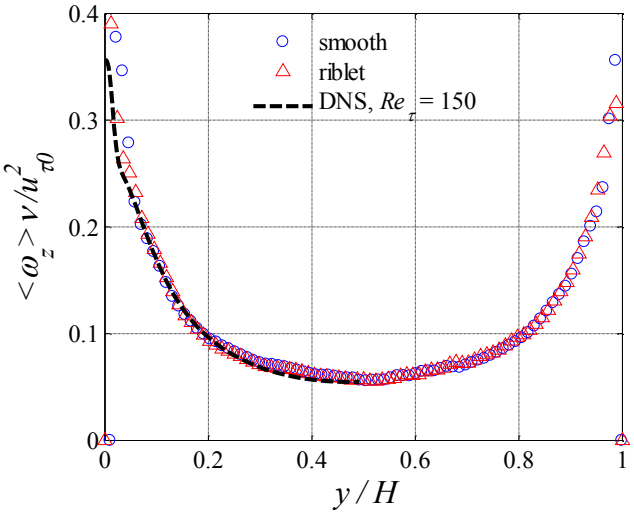

Figure 4.11. Spanwise root mean square vorticity fluctuation from PIV measurement normalized using $u_{\tau 0}$ of the smooth wall.

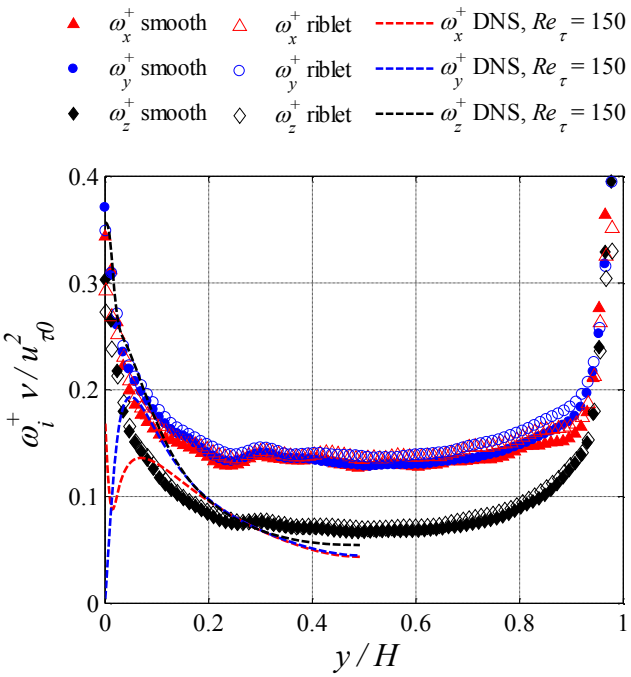

Figure 4.12. Root mean square vorticity fluctuations from tomo-PIV measurement with $u_{\tau 0}$ over smooth wall.

4.2.6 Length-scale of turbulent structures

The streamwise correlations of streamwise and wall-normal velocity fluctuations are defined as,

$$C'_{uu}(\delta x^+) = \frac{<u(x,y_0)u(x+\Delta x,y_0)>}{<u(x,y_0)^2>}, \tag{4.5}$$

and

$$C'_{vv}(\delta x^+) = \frac{<v(x,y_0)v(x+\Delta x,y_0)>}{<v(x,y_0)^2>}, \tag{4.6}$$

respectively, where δx^+ is the streamwise length scale. For the spanwise two points correlations C_{uu} (δz^+) and C_{ww} (δz^+), where δz^+ is the spanwise length scale, Kim, Moin, and Moser (1987) and Suzuki and Kasagi (1994) showed they both fall off to zero over the smooth wall at around $\delta z^+ = 60$ and $\delta z^+ = 40$, respectively. The measurement volume of tomo-PIV in the z direction at present is only 40 wall units, so the data are not able to provide with the spanwise length scales. Streamwise C_{uu} (δx^+) and C_{vv} (δx^+) can be resolved from PIV data, as shown in Figure 4.13. At y^+ around 11, C_{uu} (δx^+) increases over the riblet wall, indicating an increased low and high speed streak coherence in the streamwise direction. In the polymer SFR study by

White, Somandepalli, and Mungal (2004), the streaks are shown to be more organized in the SFR case which supports the observed change in $C_{uu}(\delta x^+)$. On the contrary, $C_{vv}(\delta x^+)$ decreases above the riblet wall, showing a shorter wall-normal extent of the ejection and sweep motions over the riblets. Suzuki and Kasagi (1994) noticed a reduction of $C_{vv}(\delta x^+)$ but they suggested $C_{uu}(\delta x^+)$ had not changed. At y^+ around 25, a location away from the influence of riblets, $C_{uu}(\delta x^+)$ and $C_{vv}(\delta x^+)$ overlap for both surfaces.

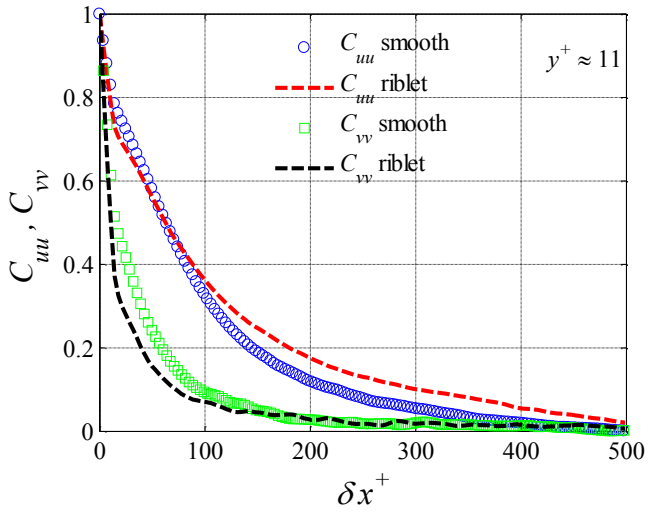

(a)

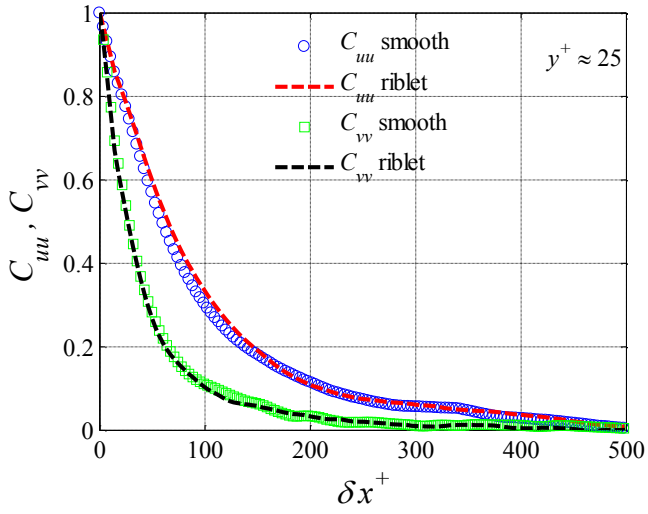

(b)

Figure 4.13. Two-point correlation in streamwise direction (a) $y^+ \approx 11$ (b) $y^+ \approx 25$ from 2D-PIV data.

4.3 Conclusion

The performances of two dimensional and three dimensional PIV and PTV in measuring the turbulent flows over a riblet surface have been evaluated. The SFR has been calculated to be 6.1% from the velocity measurement in the viscous sublayer and to be 7.4% from the profiles of the Reynolds shear stress for trapezoidal riblets of $s^+ = 11$, $h / s = 0.5$ and $\alpha = 30^\circ$. The reduction is compatible with the 6% SFR reported by Bechert et al. (1997) over the surface with same riblets. The attenuations of the turbulence intensities above the riblets are observed to be 5.9%, 9.4% and 9.4% for streamwise, wall-normal and spanwise components. The measurement errors are calculated to be 0.24 pixels for wall-normal velocity fluctuation by planar PIV and 0.34 pixels for spanwise velocity fluctuation by 3D-PTV. Three components of vorticity over the riblet surface are first shown with tomo-PIV measurement in the experimental riblet study, but no change is spotted compared to the vorticities over the smooth surface, due to the large measurement errors in the calculation of the velocity gradients fields. The divergence of the velocity field is calculated from tomo-PIV to be 0.04 voxel/voxel (Scarano et al. 2006). The detailed quadrant analysis from 2D-PIV is able to capture the attenuation of ejection and sweep. The streamwise two-point correlations are available from planar PIV showing the increased organization of the high speed and low speed streaks over the riblets wall.

Chapter 5. Skin friction reduction over riblet and superhydrophobic surfaces

5.1 Introduction

A higher SFR is expected when the SHSs and the riblets are combined together. These two SFR techniques are complementary to each other in some aspects: (1) riblets increase the surface area exposed to the flow due to the groove patterns, while SHSs decrease the effective area because of the shear-free air layers (2) the streamwise slip is preferred over SHSs but the spanwise slip harms its performance; riblets help align the flow in the streamwise direction and reduce the flow in the spanwise direction (3) high shear might cause depletion of the air layers on SHSs but the flow regions inside the riblets are relatively weaker (Barbier, Jenner, and D'Urso 2012; Prince, Maynes, and Crockett 2014).

Barbier, Jenner, and D'Urso (2012) made the first attempt to fabricate SHSs on the base of the riblet grooves. The depth of the sawtooth grooves varied from 10 μm to 1000 μm. The SHSs were created by a combination of the anodized nanopores and the hydrophobic polymer coatings. The measurement results in a cone-and-plate rheometer showed up to 20% SFR over the 100 μm deep grooves coated with SHSs, which is a great improvement compared to about 5% SFR over the none-coated 100 μm grooves. On the coated grooves with 10μm and 1000μm depth, the SFR is not increased as much as that on the 100 μm grooves, but it is still larger than the SFR over the none-coated riblet surfaces. They suggested that neither too small nor too large riblets with superhydrophobic coatings provide obvious benefits for SFR. However, the geometry of the grooves and the range of s^+ have not been explicitly explained in Barbier, Jenner, and D'Urso (2012), making it difficult to predict how the SHSs help improve the performances of riblets. Moreover, their flows were in transitional and turbulent regime. Investigations in the fully developed turbulent flows are still needed. Prince, Maynes, and Crockett (2014) manufactured surfaces containing riblets and superhydrophobic micro-ribs using photolithography. They tested the surfaces at the Reynolds numbers of 5,000 to 15,000. A 5% higher SFR at low Reynolds numbers ($5{,}000 < \mathrm{Re} < 9000$, corresponding to $8 < s^+ < 13$) compared to the SFR over the riblet surface was obtained. With the increase of Reynolds numbers ($11{,}000 < \mathrm{Re} < 15{,}000$, corresponding to $15 < s^+ < 20$), limited

improvement of SFR (~ 0%) was observed possibly resulted from the lost air pockets in SHSs. However, as indicated in the study by Prince, Maynes, and Crockett (2014), the uncertainty of their pressure drop measurements is large, leaving the conclusion questionable. Based on the results of Barbier, Jenner, and D'Urso (2012) and Prince, Maynes, and Crockett (2014), Golovin et al. (2016) doubted the feasibility of combining riblets and SHSs since the two techniques are not working in the same range of the optimal length scale.

If the surface roughness of SHSs is less than the viscous sublayer thickness, SHSs are hydrodynamically smooth after they are wetted by the fluids (Gad-el-Hak 2013, Vajdi Hokmabad and Ghaemi 2016). Therefore their existence should not affect the SFR performance of the riblets. Considering the working mechanism of the riblets (detailed in 2.2.3), the SFR over the surfaces containing both riblets and superhydrophobic coatings is presumed to improve when riblets are in the regime of SFI ($s^+ > 30$). Only in this situation, the streamwise vortices enter the riblet valleys and move around over the slip boundaries inside the coated valleys.

In view of the few studies and the confusion of the results regarding the riblets and SHSs, the current study performs measurements over riblet surfaces coated with SHSs at the Reynolds number of $Re_\tau = 141$. A two dimensional PIV is employed to observe the changes of turbulent statistics over the surfaces. The sizes of the riblets are distributed from small ($s^+ = 8.5$), medium ($s^+ = 17$) to large ($s^+ = 34$) in order to see when the SHSs will benefit the SFR of the riblets.

5.2 Results and discussion

The test surfaces are located at $y / H = 0$ and a smooth surface is kept in the bottom at $y / H = 1.0$. For cases with non-coated and coated riblet surfaces, $y / H = 0$ corresponds to the riblet tip locations. Turbulence intensities from DNS data at $Re_\tau = 150$ (Tsukahara et al. 2005) in a smooth channel are attached as reference.

5.2.1 Turbulent structure over the riblet surfaces

Due to the variations of the performance of the water channel pump, mean streamwise velocities in each case differ a little from each other. The normalization is performed over the mean streamwise velocities with individual bulk streamwise velocity across the channel height (U_b) in each case. The bulk velocities are in the range of 0.173 m/s to 0.184 m/s. The normalized mean streamwise velocity from EC methods is shown in Figure 5.1 (a). The non-zero velocity over the smooth surface is a result of the mirrored images outside the wall and difficulty in capturing large velocity gradients with finite window size. For the riblet case at $s^+ = 34$, the slip is much larger mainly because of the existence of the flow between the protruded riblet tip regions. If $y / H = 0$ is set at the virtual origin instead of the riblet tip, the differences between velocities at $y / H = 0$ in each case would be smaller. At the same time, shown in the magnified view in Figure 5.1 (b), the parabolic curve of velocities between $0 < y / H < 0.02$ indicate the erroneous measurements. Therefore all the turbulent statistics in this range are not considered in the following analysis. In Figure 5.1 (b), the velocities over riblets of $s^+ = 8.5$ and 17 are higher than that on the smooth surface, while the velocity over $s^+ = 34$ is slightly lower from $0.07 < y / H < 0.2$. Such trends agree with the change of the thickness of the viscous sublayer over riblet surfaces: the viscous sublayer become thinner in SFR conditions but turn thicker in SFI cases (Lumley 1973; Hooshmand et al. 1983; Choi, Moin, and Kim 1993). Therefore the velocity profile is uplifted in SFR cases and downshifted in SFI cases. Above $y / H > 0.2$ in Figure 5.1 (a), negligible difference is observed between cases.

Turbulence intensities are normalized by the individual theoretical friction velocity ($u_{\tau 0}$) estimated based on the bulk velocity of individual cases. The estimated friction velocity varies from 0.0111 m/s to 0.0117 m/s. The normalized streamwise velocity fluctuation is shown in Figure 5.1 (c). Limited with the resolution and influenced by the mirrorred particle images, $<u^2>$

increases near the wall and the peak values are not captured. In Figure 5.1 (d) the magnified view, it is shown that $<u^2>$ over the smooth wall is the same with the DNS result above $y / H > 0.07$. At the bottom channel ($y / H > 0.5$) in Figure 5.1 (c), $<u^2>$ from all cases overlap with each other. Compared to the smooth case, $<u^2>$ at the top half channel ($y / H < 0.3$) has been attenuated over the riblet surfaces and more reduction is observed with the increase of s^+. Suzuki and Kasagi (1994), Choi, Moin, and Kim (1993) and El-Samni, Chun, and Yoon (2007) have also reported same changes. Different from the other two studies, Choi, Moin, and Kim (1993) obtained increased $<u^2>$ near the riblet tip, as a result of the relatively sharp shape of the riblets. The $<u^2>$ is expected to reduce when the valley region accounts a large area of the riblet, which applies to the riblet shape in the current study. Note that the thickness of the laser sheet (about 1 mm) is not wide enough to cover a whole riblet region from tip to tip in the case of $s^+ = 34$ ($s = 3$ mm). It covers the area starting from the midpoint between the riblet tip and valley and ending at the valley, thus it is reasonable to obtain a reduced $<u^2>$.

The normalized wall-normal velocity fluctuation is presented in Figure 5.1 (e). For the smooth case, both peak values are the same and higher than that of the DNS result. The maximum difference is calculated as a measurement error to be 0.18 pixels by comparing maximum difference between the wall-normal velocity fluctuation in the current study and that in the DNS. As is observed in Figure 5.1 (f), the top peak of $<v^2>$ have been reduced 4.6% and 13.4% when $s^+ = 8.5$ and 17, respectively and is increased by 7.5% over riblet of $s^+ = 34$. In the bottom channel shown in Figure 5.1 (e), $<v^2>$ in all cases nearly match with each other and the slight differences come from either the measurement error or the flow development across the channel to adapt to the changes in the top channel. Choi, Moin, and Kim (1993) observed 10% reduction of maximum $<v^2>$ at $s^+ = 20$ and 5% increase when $s^+ = 40$ over sawtooth riblets.

The normalized Reynolds shear stress is shown in Figure 5.1 (g). The two peak values over the smooth wall are in 3% difference. The measurement error is estimate to be 0.22 pixels. At $y / H = 0.5$, the Reynolds shear stresses are nearly zero in all cases. Wall shear stresses at test surfaces in this situation are proportional to the slope of the Reynolds shear stress at $y^+ > 30$. The slopes are noticed to decrease at $s^+ = 8.5$ and 17 with more reduction at $s^+ = 17$ and to increase when $s^+ = 34$ relative to the slope over the smooth case. The top peak values can also be a

criterion of skin-friction change. It is reduced 4.1% and 9.8% and increased 6.5% over riblets at $s^+ = 8.5$, 17, 34, respectively, shown in Figure 5.1 (h). Near the channel center and in the bottom channel in Figure 5.1 (g), only the case of $s^+ = 34$ does not coincide with the others as a consequence of further penetration of riblet effect at SFI regime.

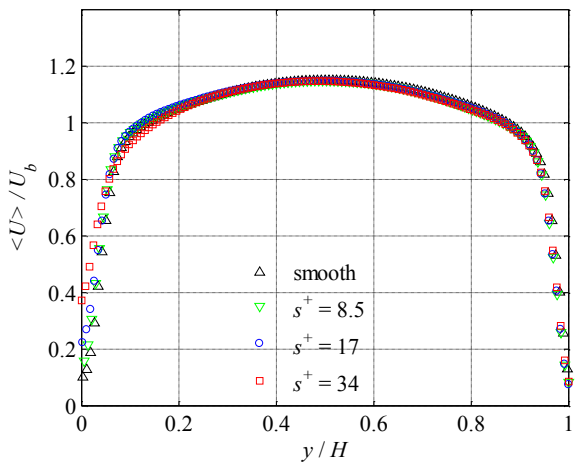
$<U> / U_b$
y / H
smooth
$s^+ = 8.5$
$s^+ = 17$
$s^+ = 34$

(a)

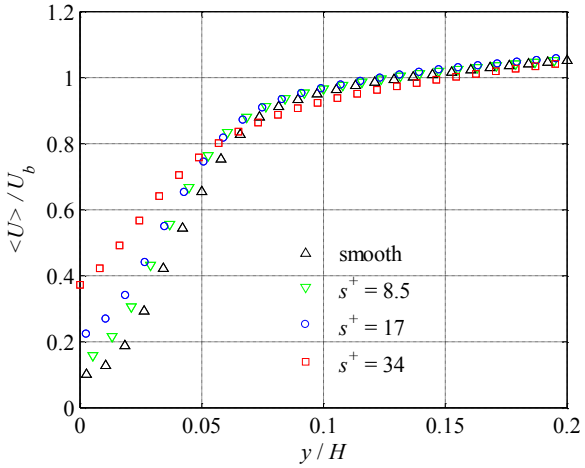
$<U> / U_b$
y / H
smooth
$s^+ = 8.5$
$s^+ = 17$
$s^+ = 34$

(b)

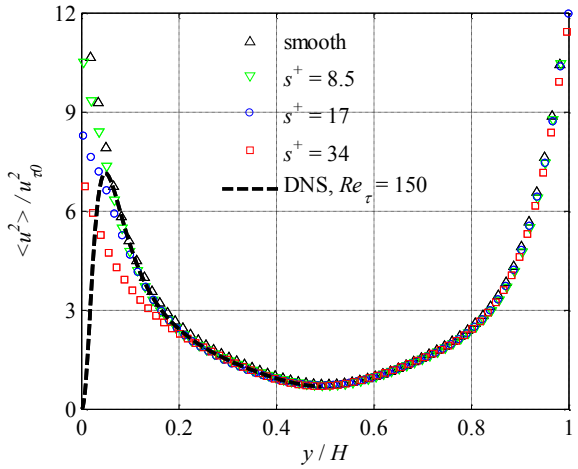
$<u^2> / u_{\tau 0}^2$
y / H
smooth
$s^+ = 8.5$
$s^+ = 17$
$s^+ = 34$
DNS, $Re_\tau = 150$

(c)

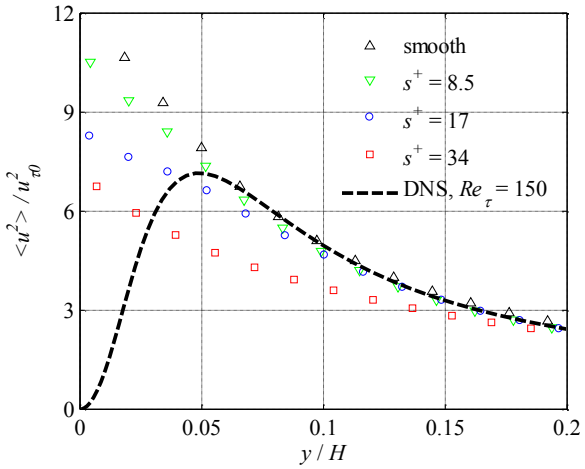
$<u^2> / u_{\tau 0}^2$
y / H
smooth
$s^+ = 8.5$
$s^+ = 17$
$s^+ = 34$
DNS, $Re_\tau = 150$

(d)

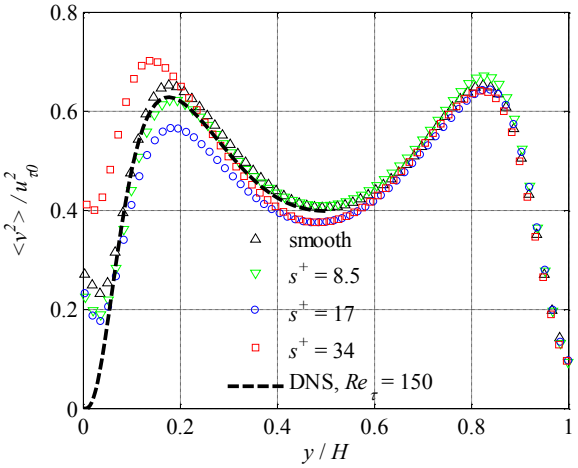
$<v^2> / u_{\tau 0}^2$
y / H
smooth
$s^+ = 8.5$
$s^+ = 17$
$s^+ = 34$
DNS, $Re_\tau = 150$

(e)

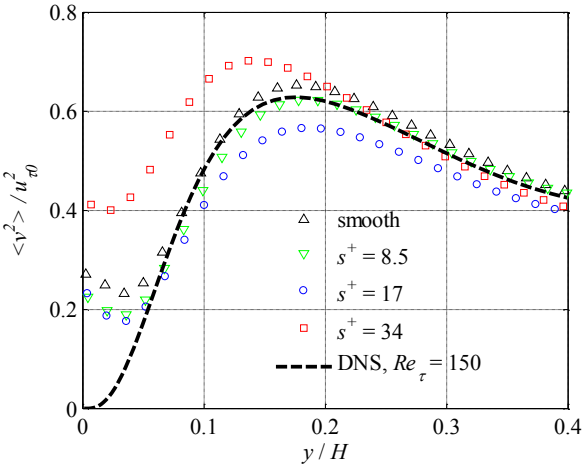
$<v^2> / u_{\tau 0}^2$
y / H
smooth
$s^+ = 8.5$
$s^+ = 17$
$s^+ = 34$
DNS, $Re_\tau = 150$

(f)

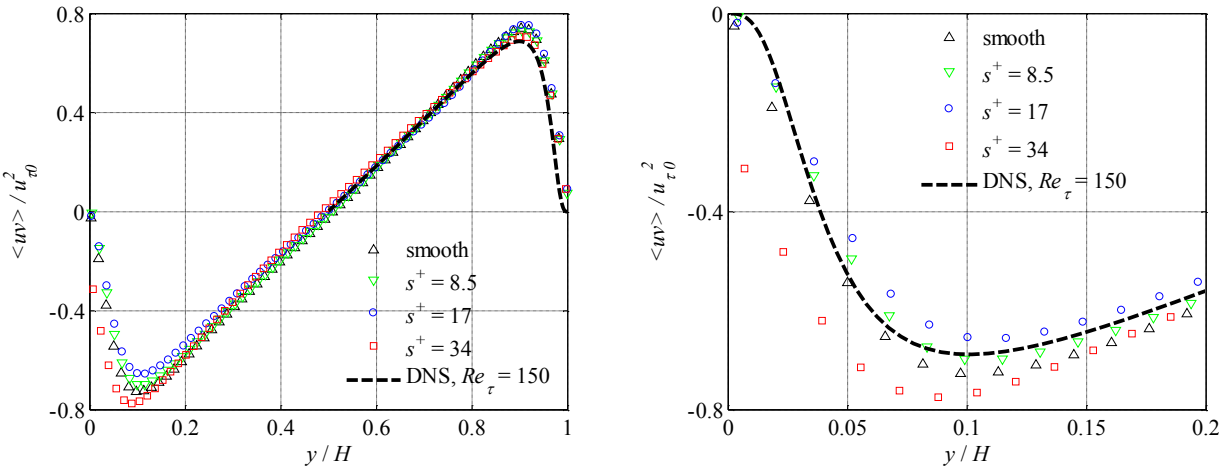

Figure 5.1. Mean velocity profile and turbulence intensities over the riblet surfaces: (a) Normalized velocity with U_b in individual case processed using ensemble of correlation method with 24 × 24 window size and 75% overlap, (b) Magnified view of (a), (c) Streamwise velocity fluctuation ($<u^2>$) normalized using $u_{\tau 0}$ of individual case, (d) Magnified view of (c), (e) Wall-normal velocity fluctuation ($<v^2>$) normalized using $u_{\tau 0}$ of individual case, (f) Magnified view of (e), (g) Reynolds shear stress ($<uv>$) from PIV measurement normalized using $u_{\tau 0}$ of individual case, (h) Magnified view of (g).

The differences between each case reach maximum at the top peak location of $<uv>$, therefore the length-scale of turbulent structures and the ejection and sweep events and are analyzed at this peak location (around $y/H = 0.1$, equals to $y^+ = 28$). The streamwise correlation of the streamwise velocity fluctuation C_{uu} (δx^+) and the wall-normal velocity fluctuation C_{vv} (δx^+) are shown in Figure 5.2. The C_{uu} (δx^+) over the smooth surface and the C_{uu} (δx^+) above the riblet surfaces at $s^+ = 8.5$ and 17 overlap, indicating no change of the length scales at $y^+ = 28$. When $s^+ = 34$, C_{uu} (δx^+) rapidly diminishes possibly with decreased coherence of the low and high speed streak in the streamwise direction. Similar to C_{uu} (δx^+), C_{vv} (δx^+) losts correlations faster at $s^+ = 34$ but doesn't change over the other two riblet surfaces. This is in agreement with the results of the reduction of both C_{uu} (δx^+) and C_{vv} (δx^+) on a SFI riblet wall at $y^+ = 14$ from Suzuki and Kasagi (1994).

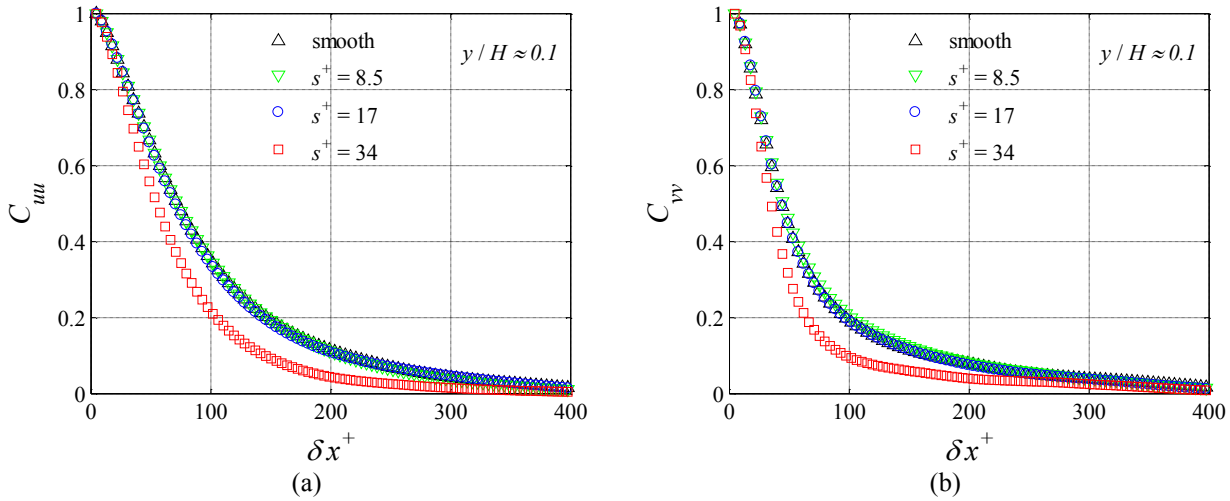

Figure 5.2. Streamwise two-point correlations over the riblet surfaces: (a) correlation of the streamwise velocity fluctuation at $y / H \approx 0.1$, (b) correlation of the wall-normal velocity fluctuation at $y / H \approx 0.1$.

Figure 5.3 shows the quadrant distribution of u and v on the smooth and riblet surfaces. It can be seen clearly that the ejection has the most contributions to the Reynolds shear stress among four events. At $s^+ = 8.5$ in Figure 5.3 (a), the area of the 0.1% contour reduces, indicating decreased strengths of the sweep and ejection events. At $s^+ = 17$ in Figure 5.3 (b), the sweep and the ejection events are even weaker as the area of both the 0.1% and 1.1% contours change smaller. First and third quadrant events are almost not affected by riblets. The increase of the sweep and the ejection events is observed over $s^+ = 34$ with more increase of the sweep event shown in Figure 5.3 (c). However, the quadrant distribution is skewed because of the disturbed viscous sublayer by riblets of large scale at $s^+ = 34$. The suppression and the increase of the sweep and ejection events are also valid in Choi, Moin, and Kim (1993) over riblets at $s^+ = 20$ and riblets at $s^+ = 40$, respectively.

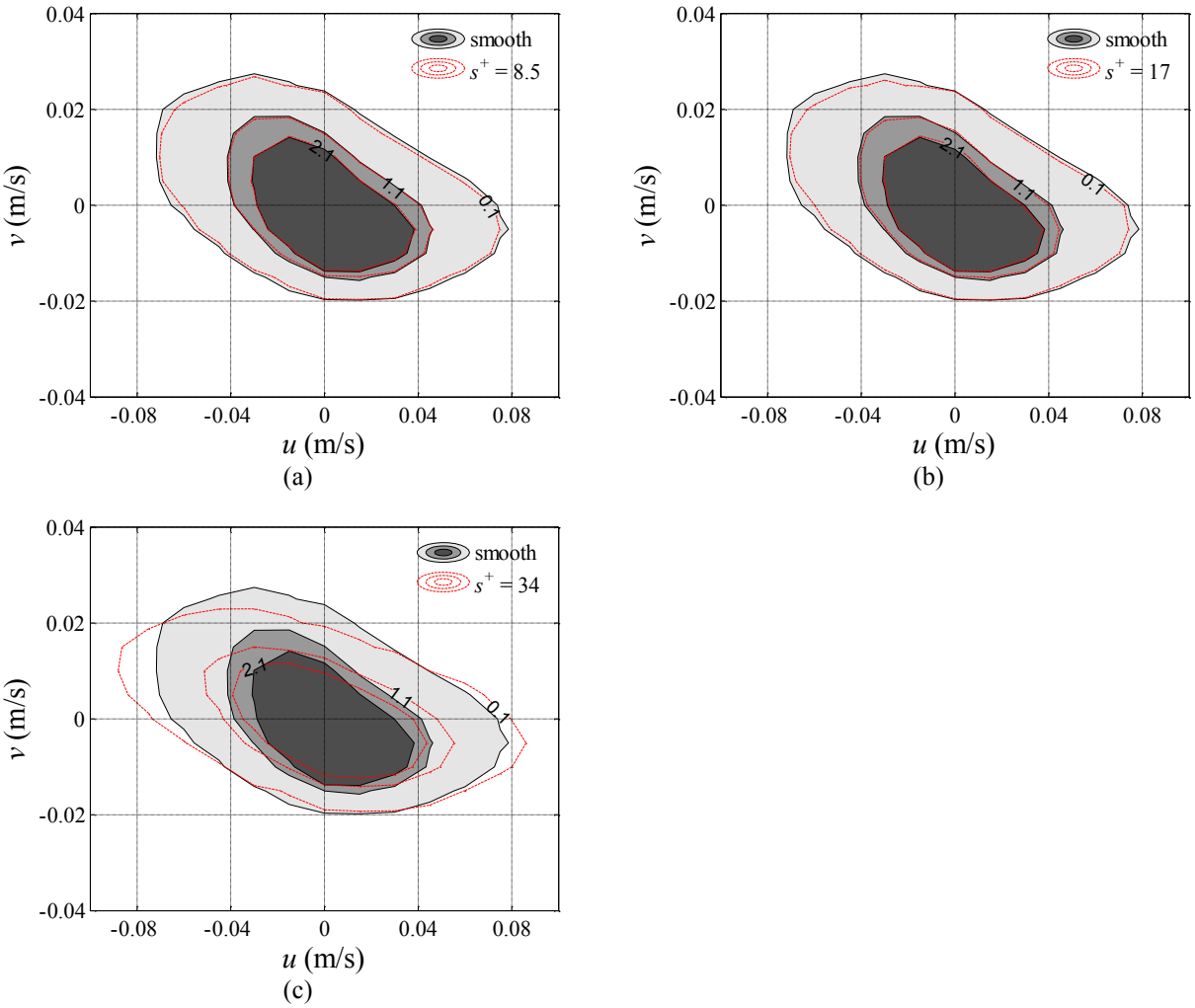

Figure 5.3. Quadrant plot of turbulent streamwise and wall-normal fluctuations at $y / H \approx 0.1$ over the riblet surfaces. The dark gray, medium gray and light gray colors in the filled contours along with the red-line contours near each level of gray denote 2.1%, 1.1% and 0.1% probability density function values.

5.2.2 Smooth surfaces

The experiments were conducted in a time length of 2 months with the tests performed over non-coated surfaces first and then the coated surfaces. During this period, the performance of water channel and the condition of the PIV system are expected to vary a little. The variances include the noise level of the camera sensor, slightly movement of the camera position, the alignment and the position of the two laser pulses due to possible mild movements of the photonic path, and the movement of the test channel resulted from constant water flush during experiments. As a relatively small quantity, $\langle v^2 \rangle$ is more sensitive to these changes than $\langle u^2 \rangle$. To verify the fluctuations of the turbulent statistics during this period, two tests over a smooth surface were employed and compared to each other. One is labelled as smooth and the other is denoted as

smooth$_2$ in the following analysis. The case of smooth was obtained together with the non-coated riblet surfaces and smooth$_2$ was measured along with the coated smooth and riblet surfaces.

The normalized mean velocity profile and the normalized turbulence intensities from the two tests over the smooth surface are shown in Figure 5.4. The $<U>$, $<u^2>$ and $<uv>$ have negligible differences in two cases as shown in Figure 5.4 (a) to (d) and (g) to (h). However, $<v^2>$ as shown in Figure 5.4 (e) has experienced about a change of $0.05u_{\tau 0}^2$. The amount of the variation is reasonable since the $<v^2>$ experiences the same magnitude of fluctuations in the streamwise direction in each test. Figure 5.5 shows the distribution of the normalized $<v^2>$ in the x-y plane. At a fixed wall-normal location, it is valid both in Figure 5.5 (a) and Figure 5.5 (b) that $<v^2>$ along the streamwise direction is fluctuating and the maximum fluctuation reaches $0.05u_{\tau 0}^2$. The value is similar to the variation observed in Figure 5.4 (e). The measurement error is estimated to be 0.18 pixels and 0.21 pixels for wall-normal velocity fluctuations in the case of smooth and smooth$_2$, respectively. Note that the relative magnitude between the top and the bottom peaks in $<v^2>$ in each case is important and will be used as a criterion to characterize the change of the turbulence in the current study. However, to avoid confusion, a new normalization method is employed to eliminate the differences between the values of $<v^2>$ in different cases: $<v^2>$ is first normalized with the bottom peak value in individual case to get $<v^2>_{nor}$:

$$<v^2>_{nor}=<v^2> / <v^2>_{bottom\ peak}, \tag{5.1}$$

and then normalized with the individual friction velocity. As shown in Figure 5.4 (f), after the two-step normalizations, the $<v^2>$ overlap over smooth and smooth$_2$, showing reliable measurement in the symmetric channel.

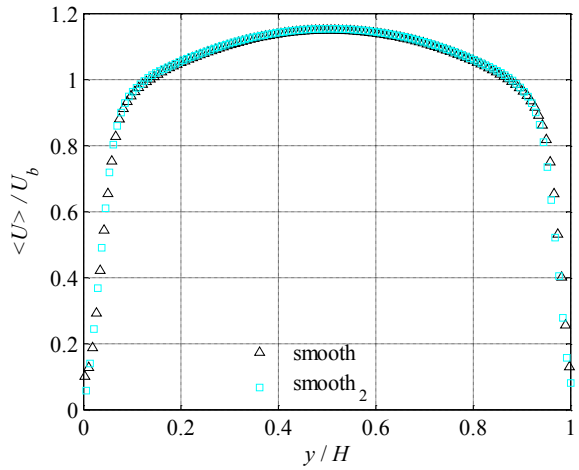
smooth
smooth 2
<U> / U_b
y / H
(a)

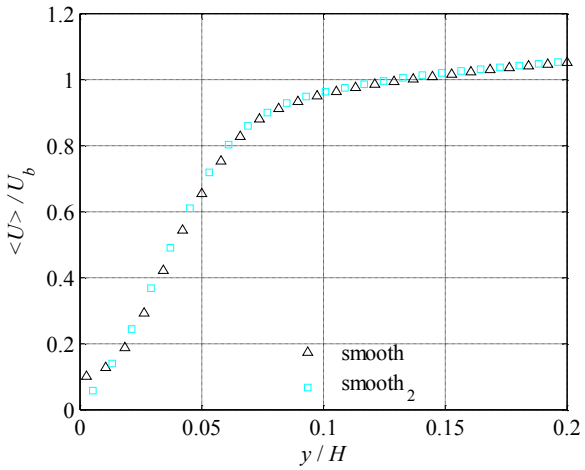
smooth
smooth 2
<U> / U_b
y / H
(b)

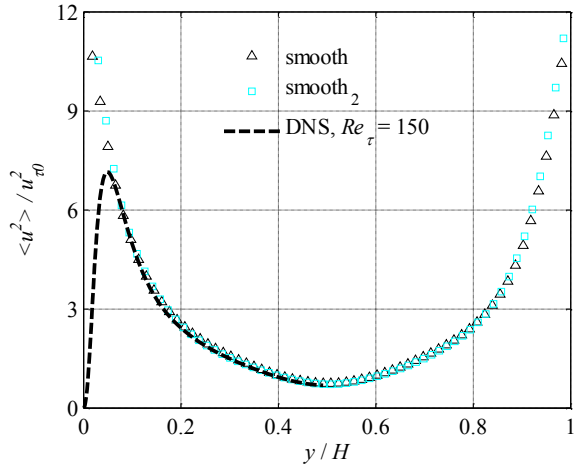
smooth
smooth 2
DNS, Re_τ = 150
<u²> / u²_τ0
y / H
(c)

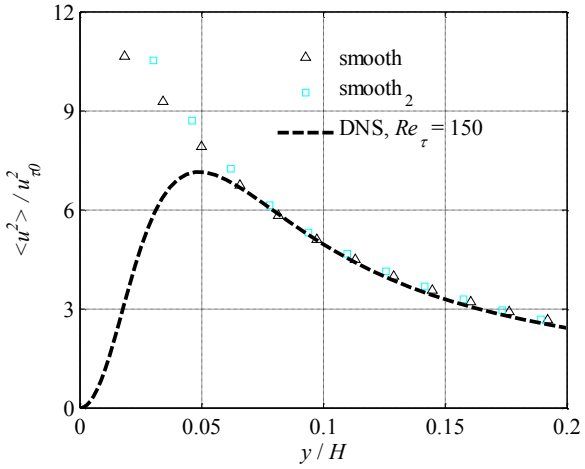
smooth
smooth 2
DNS, Re_τ = 150
<u²> / u²_τ0
y / H
(d)

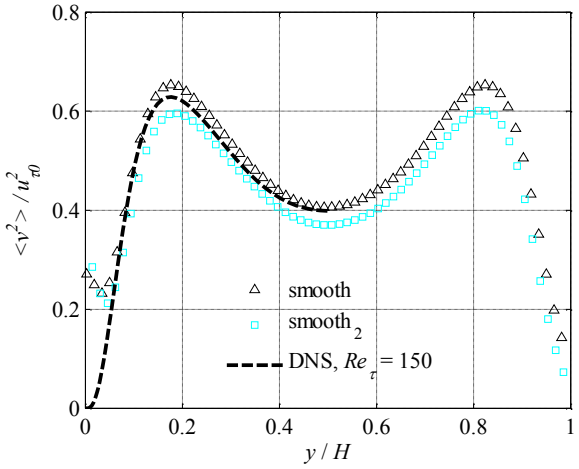
smooth
smooth 2
DNS, Re_τ = 150
<v²> / u²_τ0
y / H
(e)

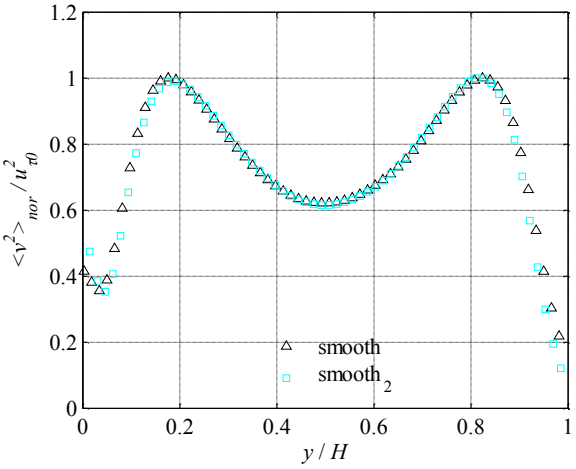
smooth
smooth 2
<v²>_nor / u²_τ0
y / H
(f)

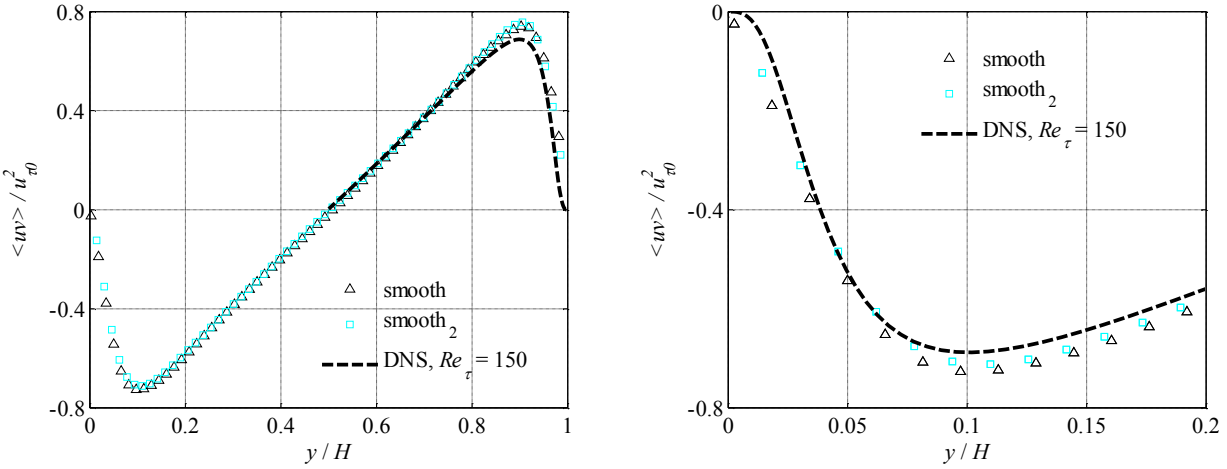

Figure 5.4. Mean velocity profile and turbulence intensities in the smooth surface tests: (a) Normalized velocity with U_b in individual case processed using ensemble of correlation method with 24 × 24 window size and 75% overlap, (b) Magnified view of (a), (c) Streamwise velocity fluctuation ($<u^2>$) normalized using $u_{\tau 0}$ of individual case, (d) Magnified view of (c), (e) Wall-normal velocity fluctuation ($<v^2>$) normalized using $u_{\tau 0}$ of individual case, (f) Normalized wall-normal velocity fluctuation with bottom peak value ($<v^2>_{nor}$) and then normalized using $u_{\tau 0}$ of individual case, (g) Reynolds shear stress ($<uv>$) from PIV measurement normalized using $u_{\tau 0}$ of individual case, (h) Magnified view of (g).

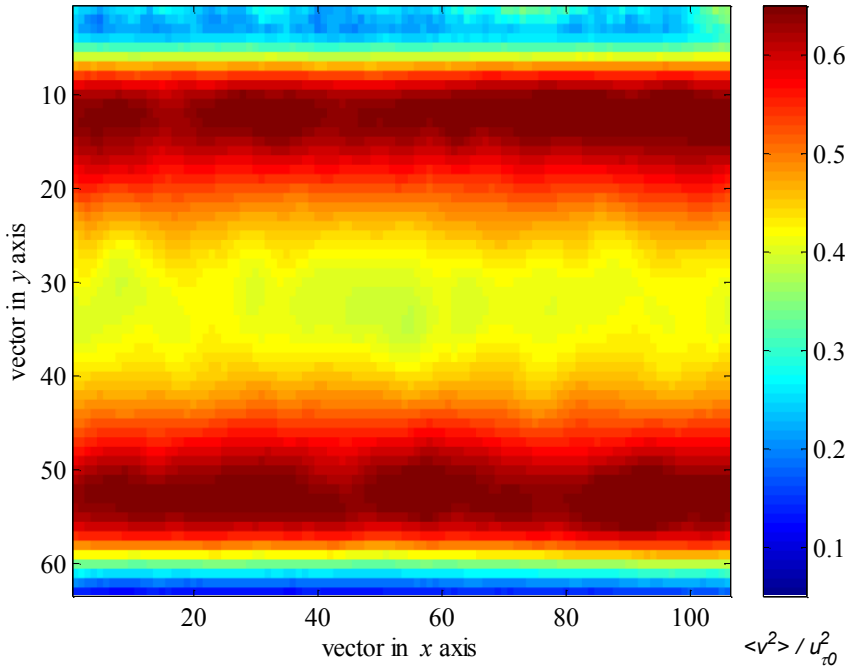

(a)

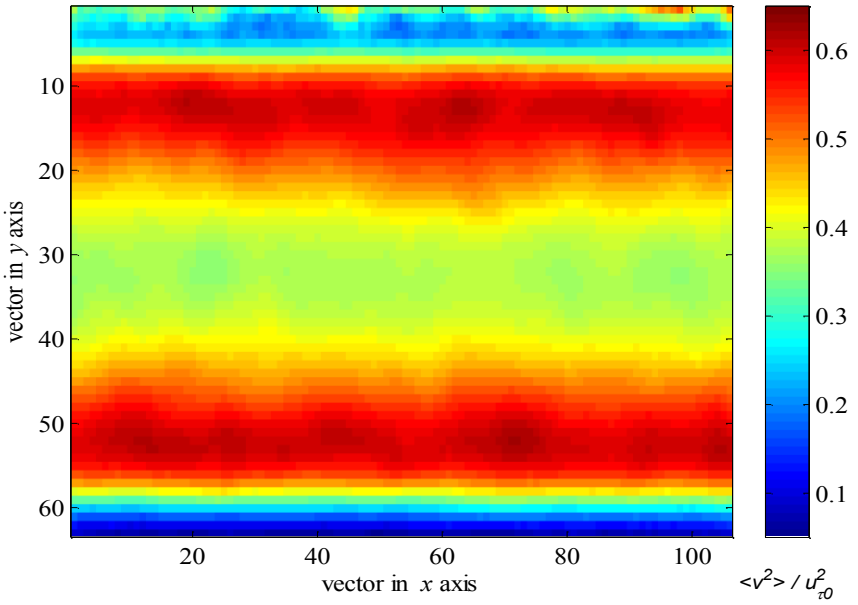

(b)

Figure 5.5. Distriution of normalized wall-normal velocity fluctuation ($<v^2>$) in x-y plane in the smooth surface tests with $u_{\tau 0}$ of individual case. (a) Distribution in smooth case, (b) Distribution in smooth$_2$ case.

The length scales of the turbulent structures and the quadrant analysis over the two smooth surfaces are provided in Figure 5.6 and Figure 5.7. When $C_{uu}(\delta x^+)$ in two cases agree with each other as shown in Figure 5.6 (a), $C_{vv}(\delta x^+)$ in Figure 5.6 (b) are spotted to reduce over smooth$_2$ in the whole data range as a result of the modified levels of the wall-normal fluctuation v. Such reduced level of $C_{vv}(\delta x^+)$ will be brought to all the cases of the coated surfaces since they were measured together. However, the quadrant distribution is not influenced by the change of v in two cases, as seen in the overlapped contours in Figure 5.7.

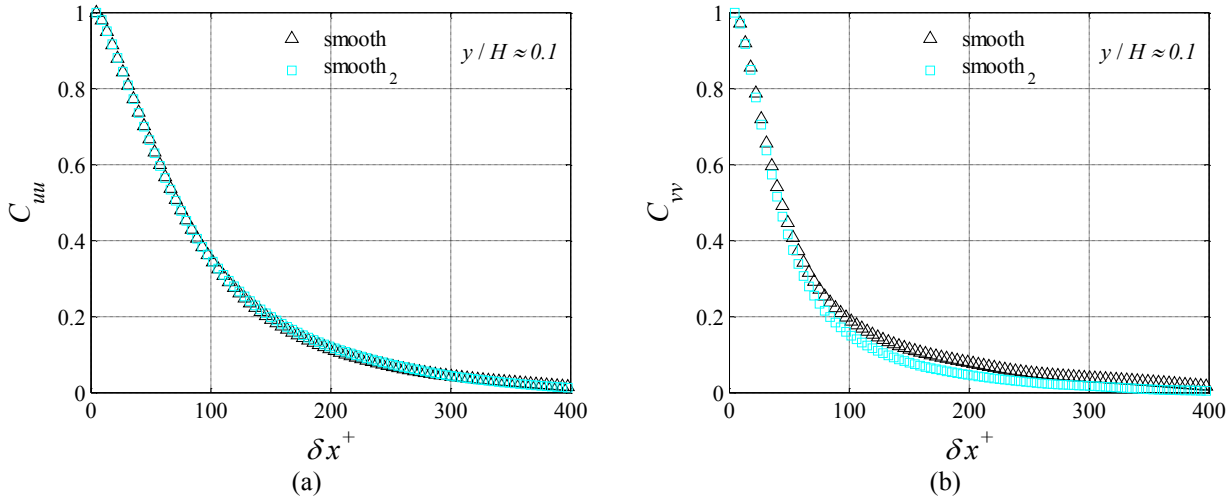

Figure 5.6. Streamwise two-point correlations in the smooth surface tests: (a) correlation of the streamwise velocity fluctuation at $y/H \approx 0.1$, (b) correlation of the wall-normal velocity fluctuation at $y/H \approx 0.1$.

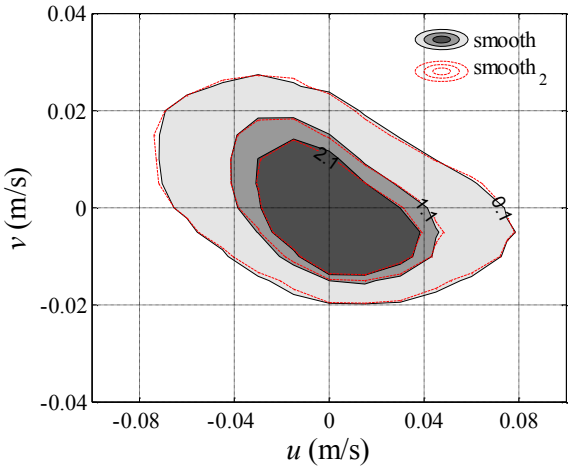

Figure 5.7. Quadrant plot of turbulent streamwise and wall-normal fluctuations at $y/H \approx 0.1$ in the smooth surface tests. The dark gray, medium gray and light gray colors in the filled contours along with the red-line contours near each level of gray denote 2.1%, 1.1% and 0.1% probability density function values.

5.2.3 Performance of the superhydrophobic surfaces

The gradual depletion of the trapped air pockets in the SHSs heavily limits the achievable SFR (Govardhan et al. 2009; Samaha, Tafreshi, and Gad-el-Hak 2012). Oxygen level was measured prior to the experiments to ensure enough air is dissolved in the water (Dilip, Bobji, and Govardhan 2015). The pH level was considered as a measure of the amount of ions that will possibly influence the longevity of SHSs. The temperature, pH level and the oxygen level in the water channel were recorded to be between 21-22˚, 8.0-8.1 and 8.4-8.5 mg/L, respectively. The normalized streamwise mean velocity profiles over non-coated smooth surface and coated smooth surface are shown in Figure 5.8 (a). No discernable change is observed over two surfaces even in the magnified view in Figure 5.8 (b). This is in agreement of the results from PIV measurement by Woolford et al. (2009) and Vajdi Hokmabad and Ghaemi (2016) where similar velocity profiles over the smooth wall and coated smooth wall were obtained. Min and Kim (2004) also showed negligible change of the mean velocity profile when the slip over SHSs is modest. However, great variations in the velocity profiles were recorded over patterned micro ridges and posts in DNS study by Martell, Rothstein, and Perot (2010). It is possible that the applied slip velocity was larger in Martell, Rothstein, and Perot (2010) than that in the current study. In addition, Daniello, Waterhouse, and Rothstein (2009) reported large slip velocities over the micro ridges with the PIV measurement and the slip velocities increase with the increase of the Reynolds number. This might come from the low resolution close to the test surfaces and the difficulty in capturing velocities in steep gradients near the wall in high Reynolds numbers.

The normalized turbulence intensities are shown in Figure 5.8 (c)-(h). As shown in Figure 5.8 (c) and (d), $<u^2>$ over the coated smooth surface is attenuated compared to the $<u^2>$ on the smooth surface and the reduction continually extends to the bottom half of the channel. Woolford et al. (2009) showed the penetration of the effects of SHS to the opposite channel wall. The $<v^2>$ in Figure 5.8 (e) and (f) experience the same changes as $<u^2>$. When the two bottom peaks are similar, the top peak is decreased by 5.3% in the SHS case, as seen in Figure 5.8 (f). The location of the top peak is noticed to shift about $0.008H$ away from the wall. For $<uv>$ in Figure 5.8 (g) and (h), the top peak is attenuated by 5% and the slope in the top half channel in the range of $y/H = 0.2\text{-}0.5$ reduces over the coated smooth surface, suggesting the reduction of

both the Reynolds shear stress and the total shear stress. The top peak of $\langle uv \rangle$ is also displaced away about $0.008H$ as $\langle v^2 \rangle$.

The reduction trends of turbulence intensities over coated smooth surface are in consistent with the observation of the DNS studies by Min and Kim (2004) and Martell, Perot, and Rothstein (2009) and the PIV measurements by Woolford et al. (2009) and Vajdi Hokmabad and Ghaemi (2016). Vajdi Hokmabad and Ghaemi (2016) quantified the reduction of $\langle u^2 \rangle$, $\langle v^2 \rangle$ and $\langle uv \rangle$ to be 12%, 13% and 15%, respectively. The different level of reductions between observations from their random structured SHSs and the current random structured SHSs might be due to different flow conditions and turbulence scales. The mild shift of the peak locations away from the wall has been reported by Min and Kim (2004) over SHSs with a mixed streamwise and spanwise slip. Conversely, Woolford et al. (2009) demonstrate peak displacement towards the wall since the location of $y / H = 0$ was set at the tip of micro-ridges. Similar peak shift towards the wall was shown in Figure 5.1 (f) and (h) over riblets with tips of large scale.

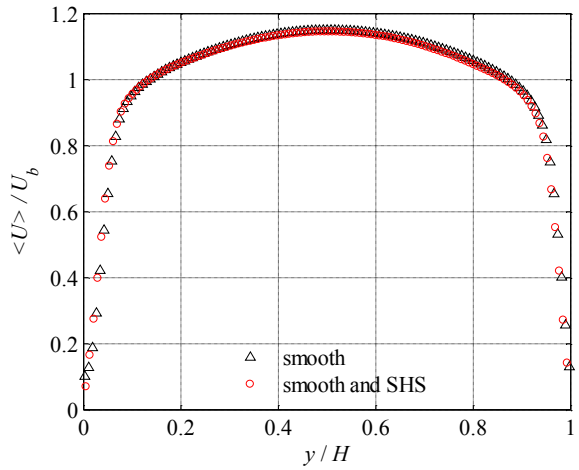
smooth
smooth and SHS
$<U> / U_b$
y / H

(a)

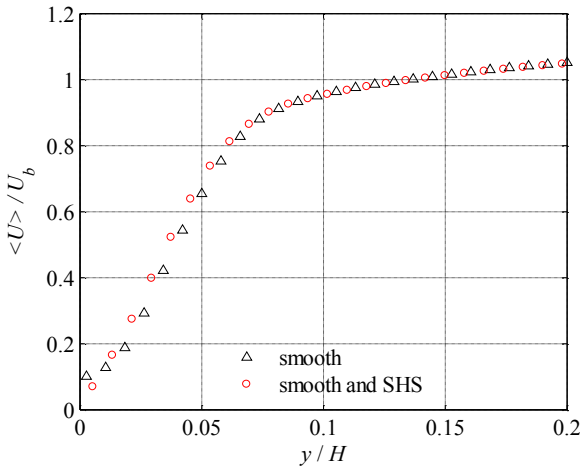
smooth
smooth and SHS
$<U> / U_b$
y / H

(b)

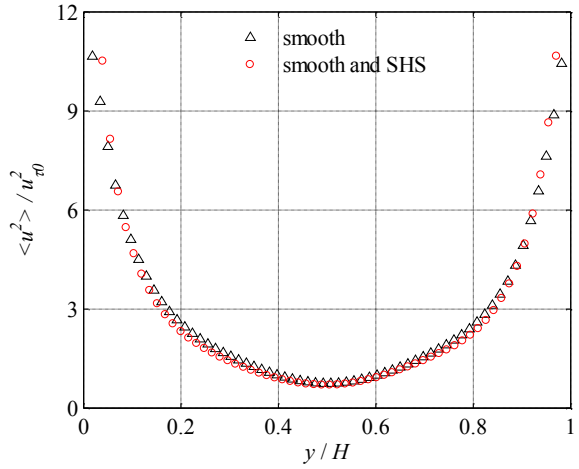
smooth
smooth and SHS
$<u^2> / u_{\tau 0}^2$
y / H

(c)

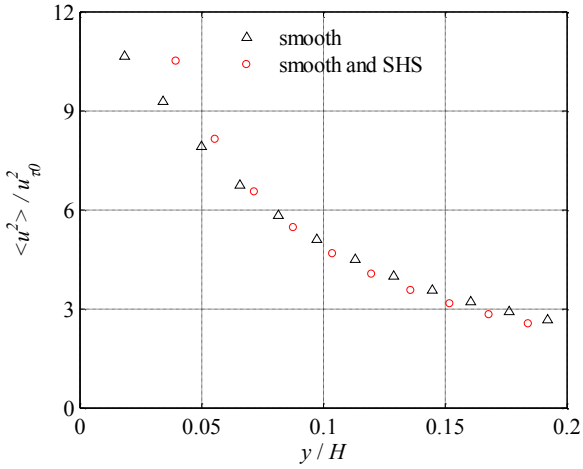
smooth
smooth and SHS
$<u^2> / u_{\tau 0}^2$
y / H

(d)

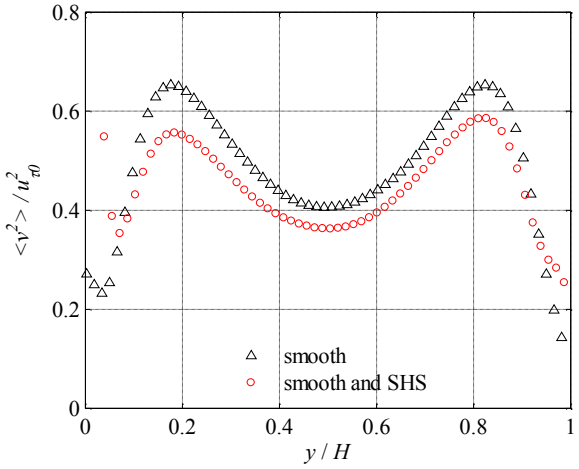
smooth
smooth and SHS
$<v^2> / u_{\tau 0}^2$
y / H

(e)

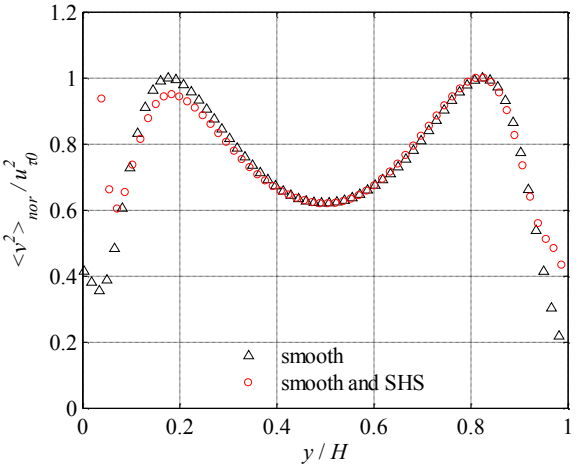
smooth
smooth and SHS
$<v^2>_{nor} / u_{\tau 0}^2$
y / H

(f)

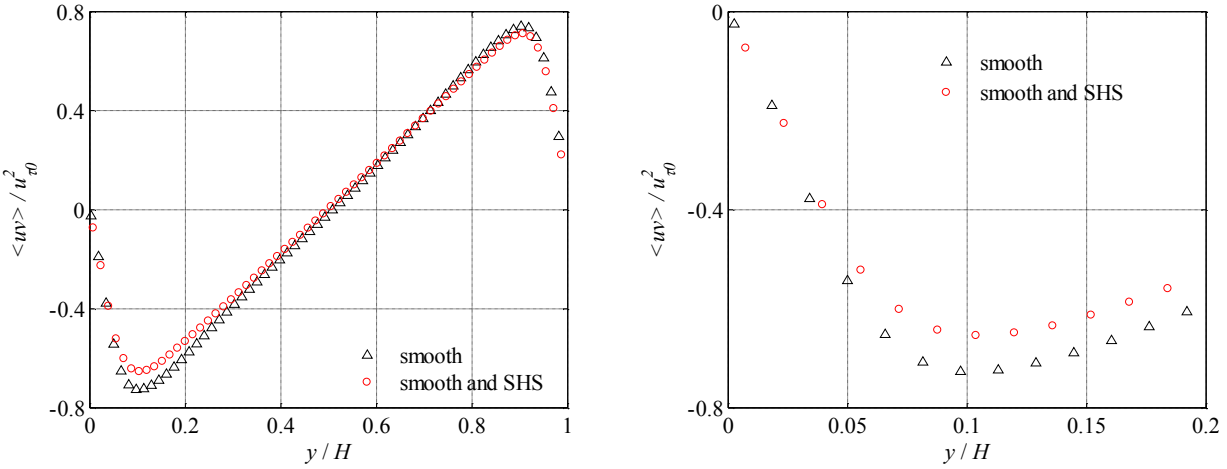

(g) (h)

Figure 5.8. Mean velocity profile and turbulence intensities over the smooth surface with superhydrophobic coatings: (a) Normalized velocity with U_b in individual case processed using ensemble of correlation method with 24 × 24 window size and 75% overlap, (b) Magnified view of (a), (c) Streamwise velocity fluctuation ($<u^2>$) normalized using $u_{\tau 0}$ of individual case, (d) Magnified view of (c), (e) Wall-normal velocity fluctuation ($<v^2>$) normalized using $u_{\tau 0}$ of individual case, (f) Normalized wall-normal velocity fluctuation with bottom peak value ($<v^2>_{nor}$) and then normalized using $u_{\tau 0}$ of individual case, (g) Reynolds shear stress ($<uv>$) from PIV measurement normalized using $u_{\tau 0}$ of individual case, (h) Magnified view of (g).

Same as before, the length-scale of the turbulent structures and the ejection and sweep events are investigated at the top peak location of <*uv*> (around $y/H = 0.1$, equals to $y^+ = 28$). The $C_{uu}(\delta x^+)$ and $C_{vv}(\delta x^+)$ are shown in Figure 5.9. The $C_{uu}(\delta x^+)$ over the coated surface is increased compared to the $C_{uu}(\delta x^+)$ over the smooth surface. This agrees with the change of $C_{uu}(\delta x^+)$ over the riblet wall of $s^+ = 11$ in section 4.2.6. When there is SFR, the streaky structures are more organized (White, Somandepalli, and Mungal 2004) so the correlation will persist longer. Vajdi Hokmabad and Ghaemi (2016) recorded the attenuation of C_{uu} in the range of $10 < y^+ < 40$ at a fixed δx^+ over the coated smooth surface. The change of $C_{vv}(\delta x^+)$ on the coated surface is due to the measurement uncertainty which also showed up in the comparison of two smooth tests in Figure 5.6 (b). No solid conclusion can be draw regarding the adjustment of $C_{vv}(\delta x^+)$ over the coated surface.

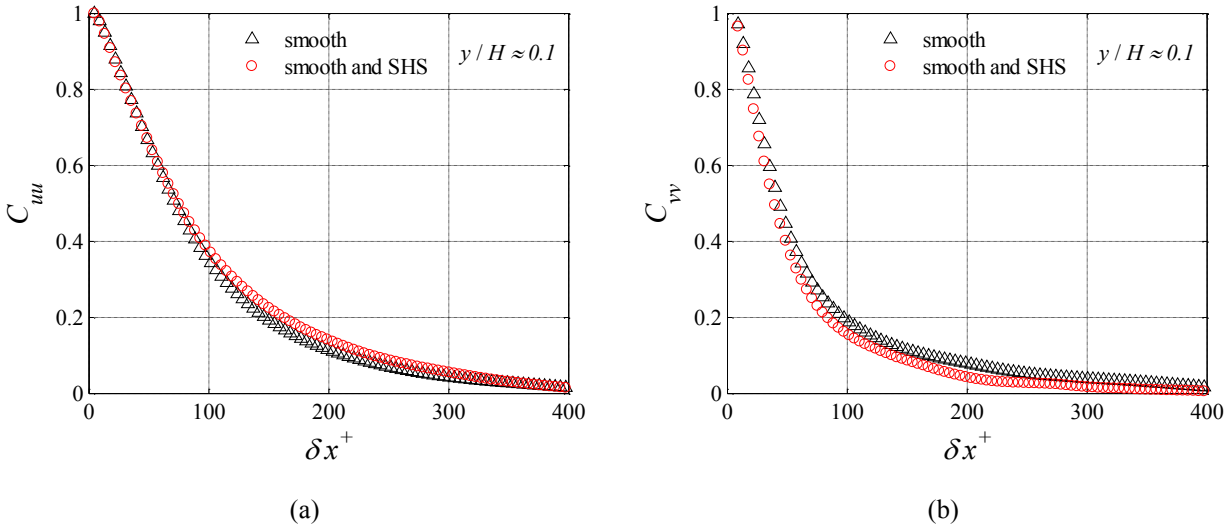

Figure 5.9. Streamwise two-point correlations over the smooth surface with superhydrophobic coatings: (a) correlation of the streamwise velocity fluctuation at $y/H \approx 0.1$, (b) correlation of the wall-normal velocity fluctuation at $y/H \approx 0.1$.

The contour of the quadrant analysis is shown in Figure 5.10. The attenuation of the sweep and ejection events is observed over coated smooth surface but the reduction is expected to be much larger as the reduction of top peak of <*uv*>. The areas of the contour 0.1% and 2.1% reduce in the sweep and ejection events and the contour 1.1% is decreased for the ejection event. Vajdi Hokmabad and Ghaemi (2016) observed an increase of contour 1.4% and a reduction of contour 0.1% for the ejection event at $y^+ = 30$ over the coated surface. The difference of the

quadrant analysis in Figure 5.10 over the smooth surface with SHS and in Figure 5.3 (a) and (b) over surfaces with riblets suggest a distinct SFR mechanism of the two SFR techniques.

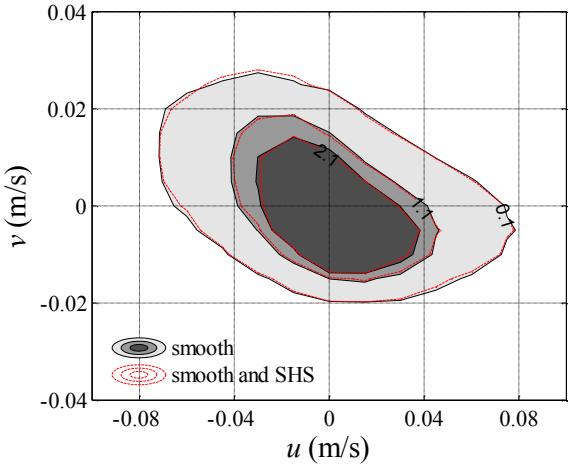

Figure 5.10. Quadrant plot of turbulent streamwise and wall-normal fluctuations at $y / H \approx 0.1$ over the smooth surface with superhydrophobic coatings. The dark gray, medium gray and light gray colors in the filled contours along with the red-line contours near each level of gray denote 2.1%, 1.1% and 0.1% probability density function values.

5.2.4 Measurement over the riblet surfaces with superhydrophobic coatings

In the case of coated riblets at $s^+ = 8.5$, normalized mean velocity profile and turbulence intensities are shown in Figure 5.11. In Figure 5.11 (g) and (h), both slopes and the top peak of $\langle uv \rangle$ over two surfaces overlap, indicating same SFR performance. Other than the regions very close the walls where the data quality is limited by resolution and wall reflection, $\langle U \rangle$ are similar in two cases, as shown in Figure 5.11 (a)-(b). The overlap of $\langle v^2 \rangle_{nor}$ in Figure 5.11 (f) shows the same relative change of the top peak and the bottom peak in two cases. Only $\langle u^2 \rangle$ increases over the coated riblets in Figure 5.11 (d).

Normalized mean velocity profile and turbulence intensities over non-coated and coated riblets at $s^+ = 17$ are shown in Figure 5.12. Similar to the situation in Figure 5.11, $\langle U \rangle$ in Figure 5.12 (a) and (b), and $\langle uv \rangle$ in Figure 5.12 (g) and (h) are similar over the two riblet surfaces. No extra SFR is observed after coating. The $\langle u^2 \rangle$ in Figure 5.12 (d) increases even more and the top peak of $\langle v^2 \rangle$ in Figure 5.12 (f) is slightly attenuated over the after coating.

Regarding the coated riblets at $s^+ = 34$, the normalized mean velocity profile and turbulence intensities, as shown in Figure 5.13, are not following the trends as seen in Figure 5.11 and

Figure 5.12. In Figure 5.13 (a) and (b), $<U>$ is reduced in the range of $0.1 < y / H < 0.3$ over the coated riblet surface. The top peak and the bottom peak of $<uv>$, shown in Figure 5.13 (g), reach the same level since the top peak has been reduced significantly compared to the non-coated riblet case in Figure 5.13 (h). This is the indication of the occurrence of the SFR. The $<v^2>$ over both coated and non-coated riblet surfaces have similar performances regardless of different skin frictions in the two cases. At $y / H < 0.1$, the $<u^2>$ is reduced on the coated riblets.

The increase of $<u^2>$ over coated riblet surfaces at $s^+ = 8.5$ and $s^+ = 17$ is conjectured to be a mixture outcome of different wall reflections in raw PIV images and the slight reduction of tip spacing due to the extra superhydrophobic layers sprayed over riblets. As is shown in Table 3.5, the reflection level over the riblet wall is not the same as that over the coated riblet wall. As for the superhydrophobic coating, though the thickness is only about half of a wall unit (40 μm), it slightly decreases the tip spacing s and valley height h of riblets. Such change is not noticeable in the whole data range, but brings differences at regions very close to the wall ($y / H < 0.05$).

The decrease of $<u^2>$ at coated $s^+ = 34$ riblet wall, however, suggests the occurrence of SFR. It is in consistent with the attenuation of $<u^2>$ shown over coated smooth surface in Figure 5.8 (c) and (d). At the same time, the reduction of $<U>$ in the range of $0.1 < y / H < 0.3$ is possibly an indication of higher velocity due to slip over SHS in the riblet valley.

Rastegari and Akhavan (2015) analytically and numerically showed that the slip velocity over SHSs is the main contributor to the SFR while the alternations of the turbulent structures over the SHSs contribute no more than 20% of the SFR in turbulent flows. The turbulence intensities after coating are found to be the same with those over the non-coated smooth surfaces. Therefore, the negligible changes of turbulence intensities on the coated riblet surfaces in the current study are reasonable. This also explains the phenomena that $<v^2>$ is reduced but $<uv>$ does not change over the coated riblet at $s^+ = 17$: the SFR is possibly attenuated due to slip velocity but the turbulent structures persist to be the same as those over the non-coated riblets.

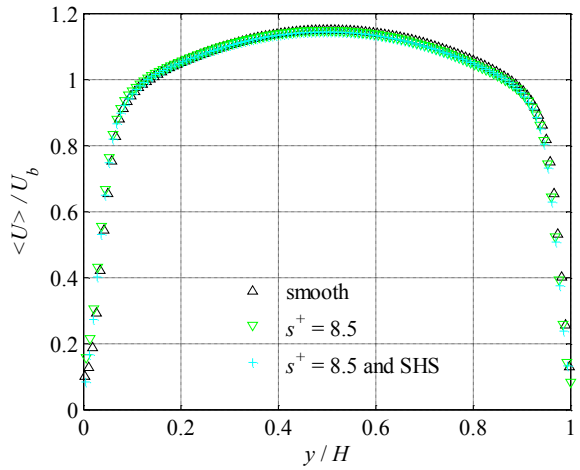
<U> / U_b
y / H
smooth
s+ = 8.5
s+ = 8.5 and SHS

(a)

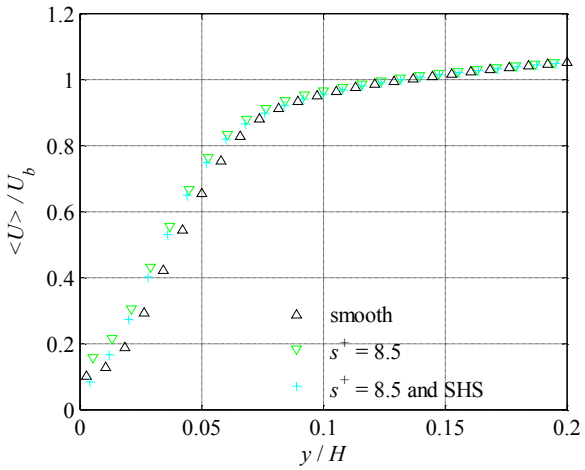
<U> / U_b
y / H
smooth
s+ = 8.5
s+ = 8.5 and SHS

(b)

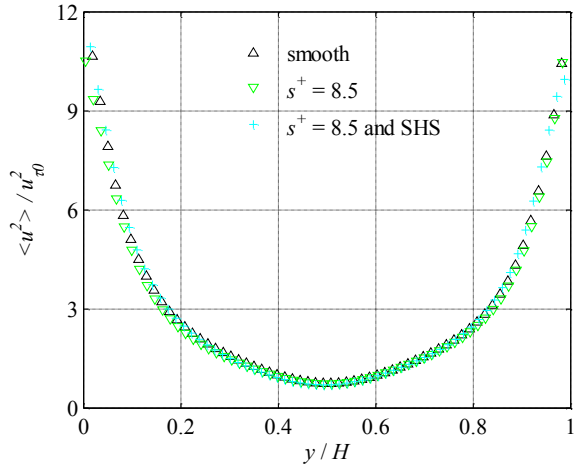
<u2> / u2τ0
y / H
smooth
s+ = 8.5
s+ = 8.5 and SHS

(c)

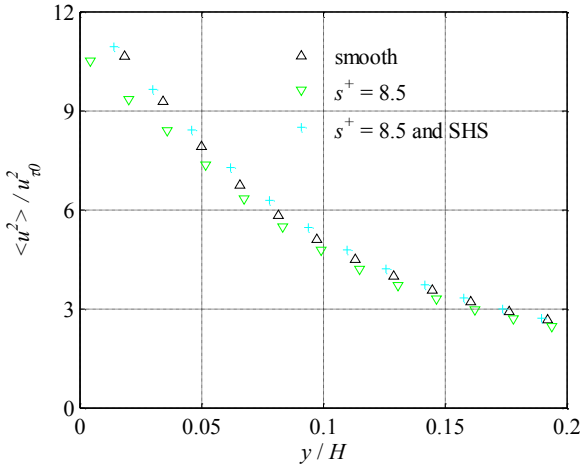
<u2> / u2τ0
y / H
smooth
s+ = 8.5
s+ = 8.5 and SHS

(d)

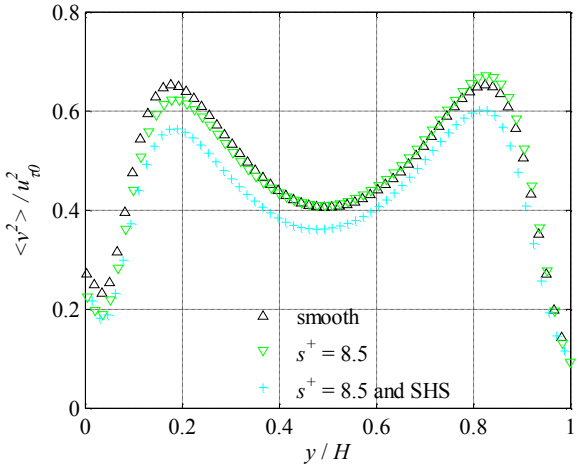
<v2> / u2τ0
y / H
smooth
s+ = 8.5
s+ = 8.5 and SHS

(e)

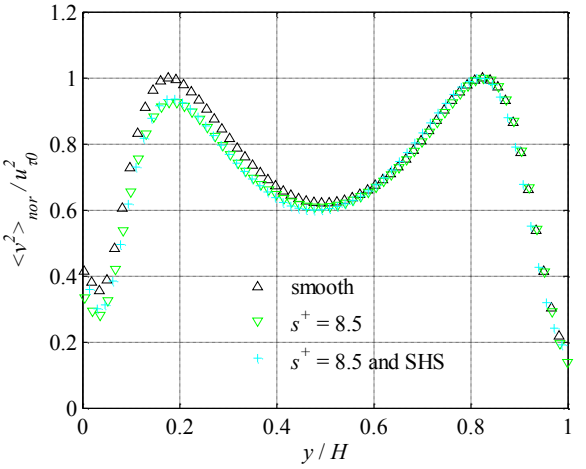
<v2>nor / u2τ0
y / H
smooth
s+ = 8.5
s+ = 8.5 and SHS

(f)

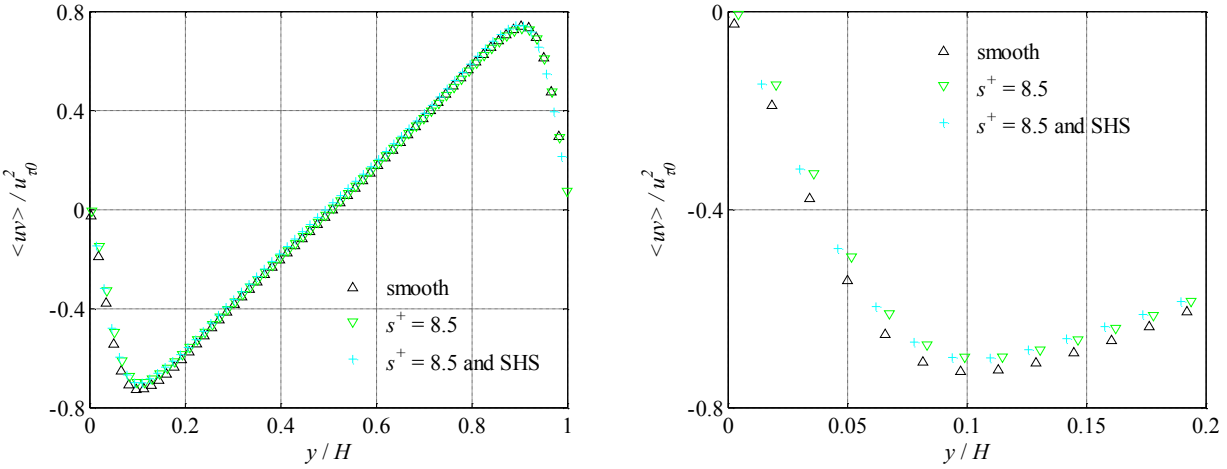

Figure 5.11. Mean velocity profile and turbulence intensities over the riblet surface at $s^+ = 8.5$ with superhydrophobic coatings: (a) Normalized velocity with U_b in individual case processed using ensemble of correlation method with 24 × 24 window size and 75% overlap, (b) Magnified view of (a), (c) Streamwise velocity fluctuation ($<u^2>$) normalized using $u_{\tau 0}$ of individual case, (d) Magnified view of (c), (e) Wall-normal velocity fluctuation ($<v^2>$) normalized using $u_{\tau 0}$ of individual case, (f) Normalized wall-normal velocity fluctuation with bottom peak value ($<v^2>_{nor}$) and then normalized using $u_{\tau 0}$ of individual case, (g) Reynolds shear stress ($<uv>$) from PIV measurement normalized using $u_{\tau 0}$ of individual case, (h) Magnified view of (g).

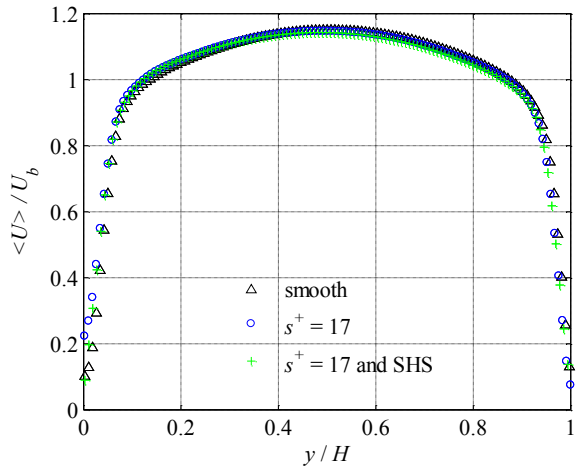
1.2
1
0.8
0.6
0.4
0.2
0
0
0.2
0.4
0.6
0.8
1
<U> / U_b
y / H
smooth
s+ = 17
s+ = 17 and SHS

(a)

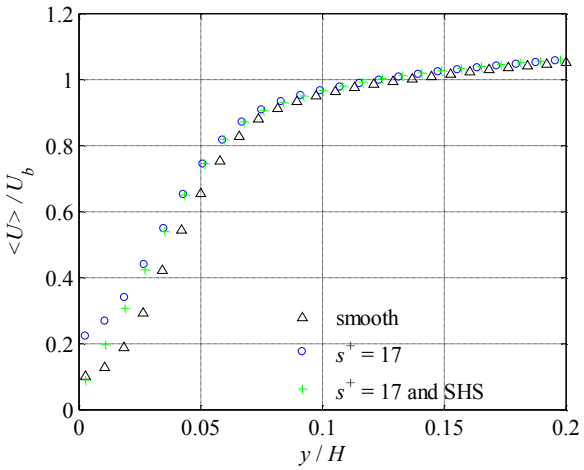
1.2
1
0.8
0.6
0.4
0.2
0
0
0.05
0.1
0.15
0.2
<U> / U_b
y / H
smooth
s+ = 17
s+ = 17 and SHS

(b)

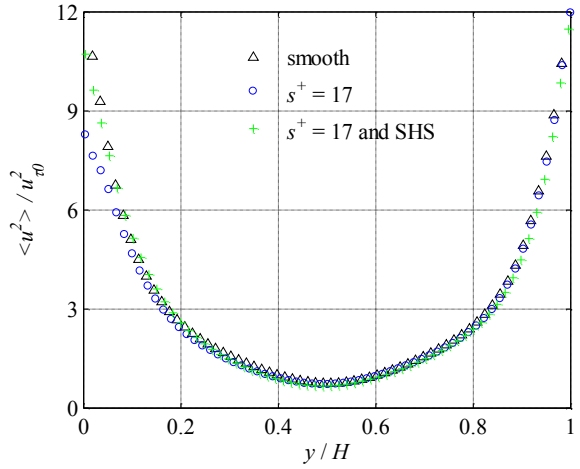
12
9
6
3
0
0
0.2
0.4
0.6
0.8
1
<u2> / u2τ0
y / H
smooth
s+ = 17
s+ = 17 and SHS

(c)

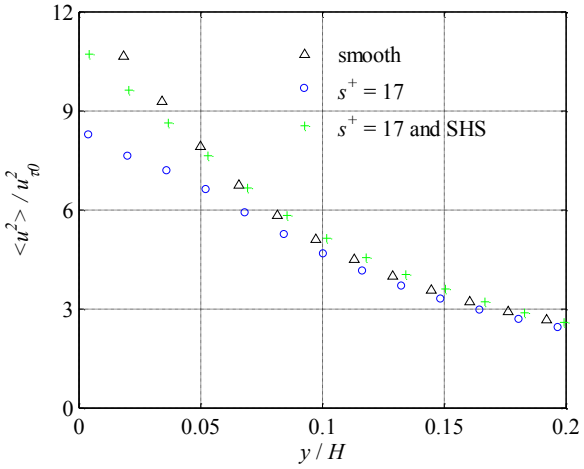
12
9
6
3
0
0
0.05
0.1
0.15
0.2
<u2> / u2τ0
y / H
smooth
s+ = 17
s+ = 17 and SHS

(d)

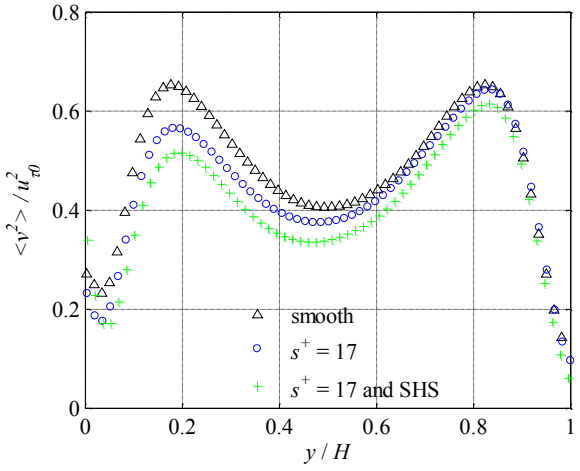
0.8
0.6
0.4
0.2
0
0
0.2
0.4
0.6
0.8
1
<v2> / u2τ0
y / H
smooth
s+ = 17
s+ = 17 and SHS

(e)

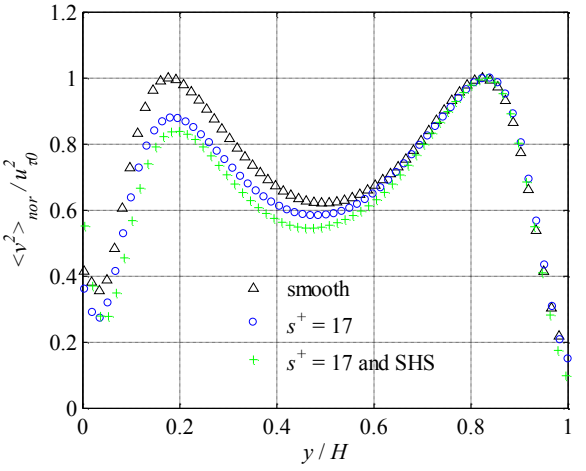
1.2
1
0.8
0.6
0.4
0.2
0
0
0.2
0.4
0.6
0.8
1
<v2>nor / u2τ0
y / H
smooth
s+ = 17
s+ = 17 and SHS

(f)

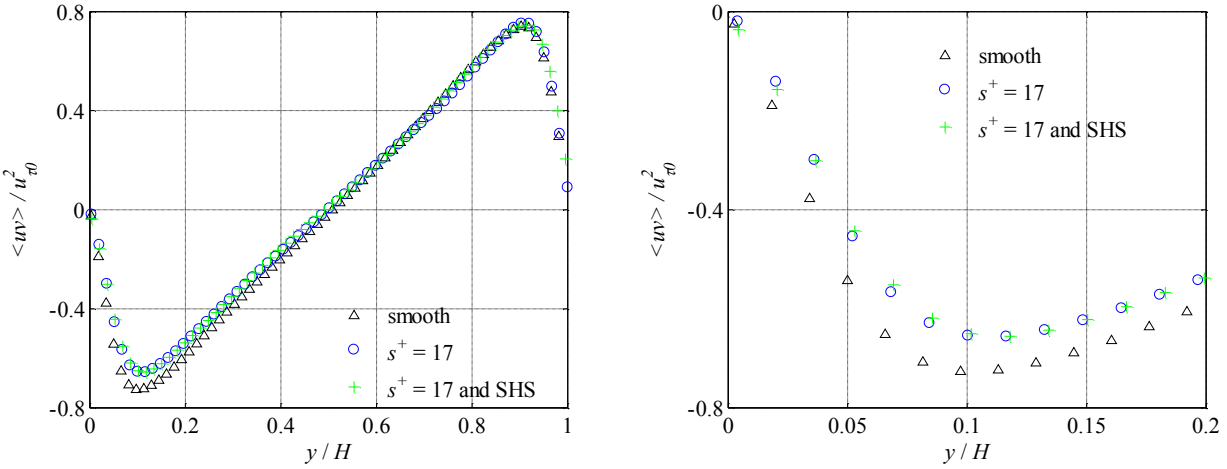

(g) (h)

Figure 5.12. Mean velocity profile and turbulence intensities over the riblet surface at $s^+ = 17$ with superhydrophobic coatings: (a) Normalized velocity with U_b in individual case processed using ensemble of correlation method with 24 × 24 window size and 75% overlap, (b) Magnified view of (a), (c) Streamwise velocity fluctuation ($<u^2>$) normalized using $u_{\tau 0}$ of individual case, (d) Magnified view of (c), (e) Wall-normal velocity fluctuation ($<v^2>$) normalized using $u_{\tau 0}$ of individual case, (f) Normalized wall-normal velocity fluctuation with bottom peak value ($<v^2>_{nor}$) and then normalized using $u_{\tau 0}$ of individual case, (g) Reynolds shear stress ($<uv>$) from PIV measurement normalized using $u_{\tau 0}$ of individual case, (h) Magnified view of (g).

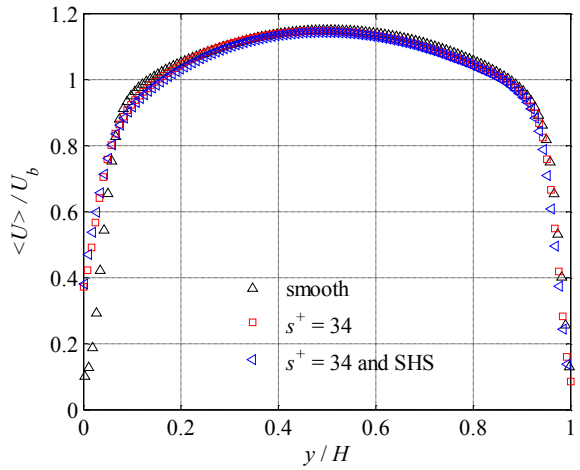
smooth
$s^+ = 34$
$s^+ = 34$ and SHS
$<U> / U_b$
y / H

(a)

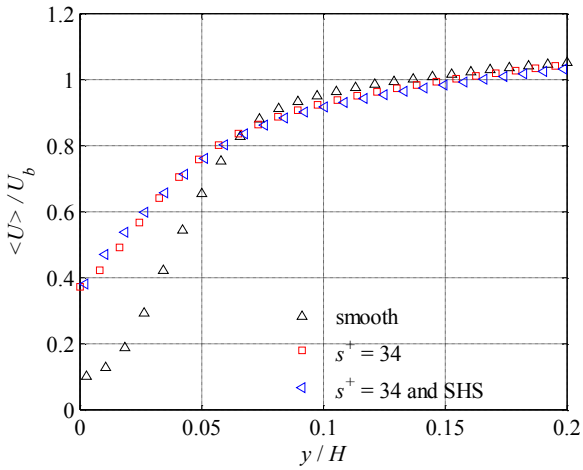
smooth
$s^+ = 34$
$s^+ = 34$ and SHS
$<U> / U_b$
y / H

(b)

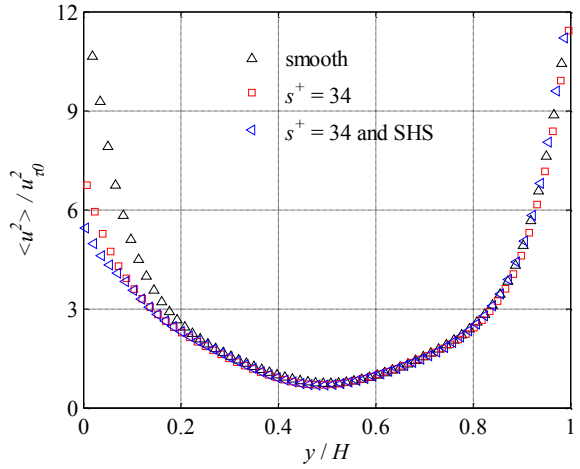
smooth
$s^+ = 34$
$s^+ = 34$ and SHS
$<u^2> / u_{\tau 0}^2$
y / H

(c)

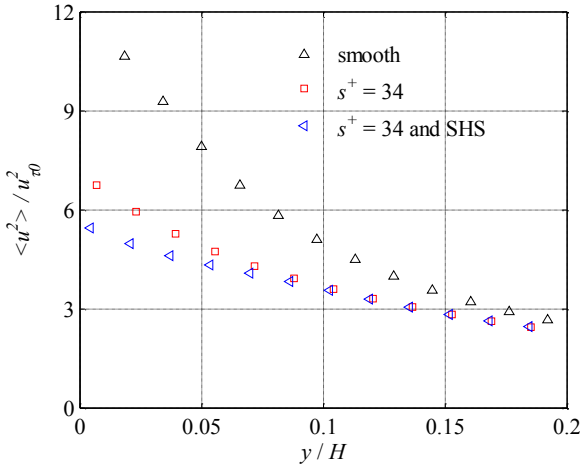
smooth
$s^+ = 34$
$s^+ = 34$ and SHS
$<u^2> / u_{\tau 0}^2$
y / H

(d)

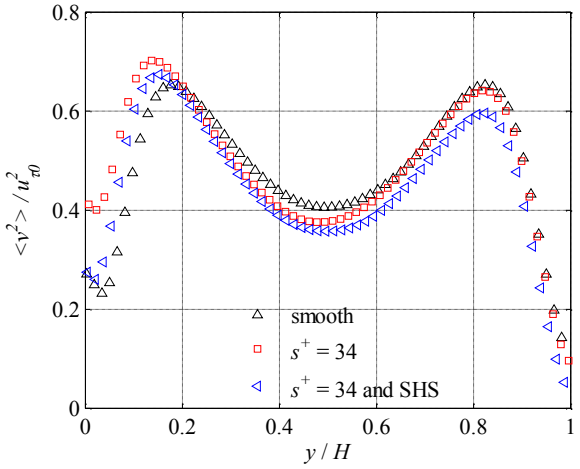
smooth
$s^+ = 34$
$s^+ = 34$ and SHS
$<v^2> / u_{\tau 0}^2$
y / H

(e)

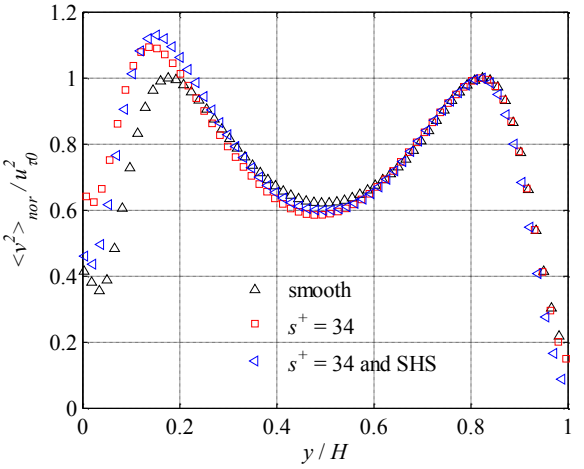
smooth
$s^+ = 34$
$s^+ = 34$ and SHS
$<v^2>_{nor} / u_{\tau 0}^2$
y / H

(f)

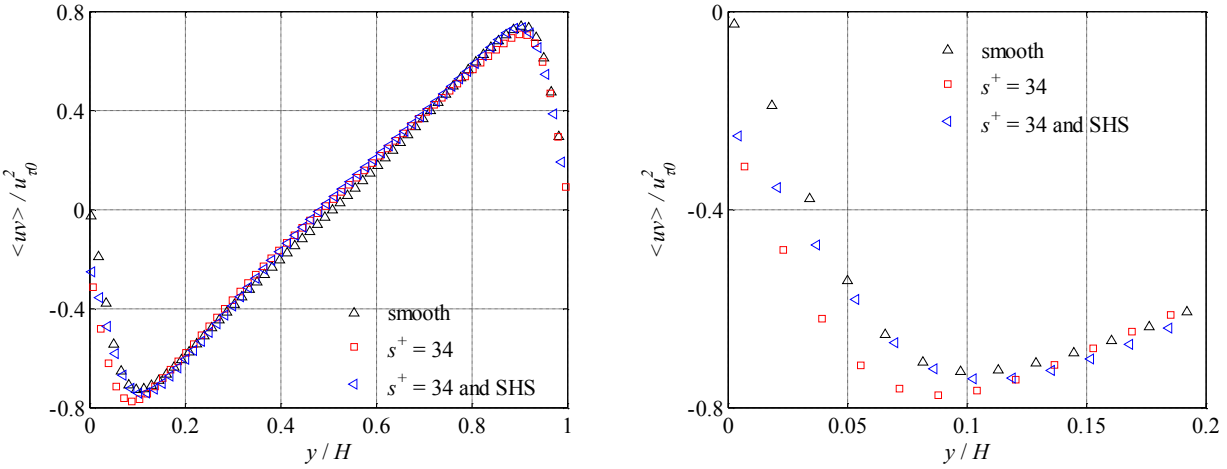

(g) (h)

Figure 5.13. Mean velocity profile and turbulence intensities over the riblet surface at $s^+ = 34$ with superhydrophobic coatings: (a) Normalized velocity with U_b in individual case processed using ensemble of correlation method with 24 × 24 window size and 75% overlap, (b) Magnified view of (a), (c) Streamwise velocity fluctuation ($<u^2>$) normalized using $u_{\tau 0}$ of individual case, (d) Magnified view of (c), (e) Wall-normal velocity fluctuation ($<v^2>$) normalized using $u_{\tau 0}$ of individual case, (f) Normalized wall-normal velocity fluctuation with bottom peak value ($<v^2>_{nor}$) and then normalized using $u_{\tau 0}$ of individual case, (g) Reynolds shear stress ($<uv>$) from PIV measurement normalized using $u_{\tau 0}$ of individual case, (h) Magnified view of (g).

The $C_{uu}(\delta x^+)$ and $C_{vv}(\delta x^+)$ for the coated riblets are shown in Figure 5.14. $C_{uu}(\delta x^+)$ preserves over the coated $s^+ = 8.5$ riblets as the non-coated riblets. In the case of the coated riblets at $s^+ = 17$ and 34, the $C_{uu}(\delta x^+)$ is increased because of their effects on SFR and turbulent structures. On the other hand, the change of $C_{vv}(\delta x^+)$ are in the same level of the differences existing between $C_{vv}(\delta x^+)$ over the two tests over the smooth surface. No additional influence of the coated riblet surfaces is observed.

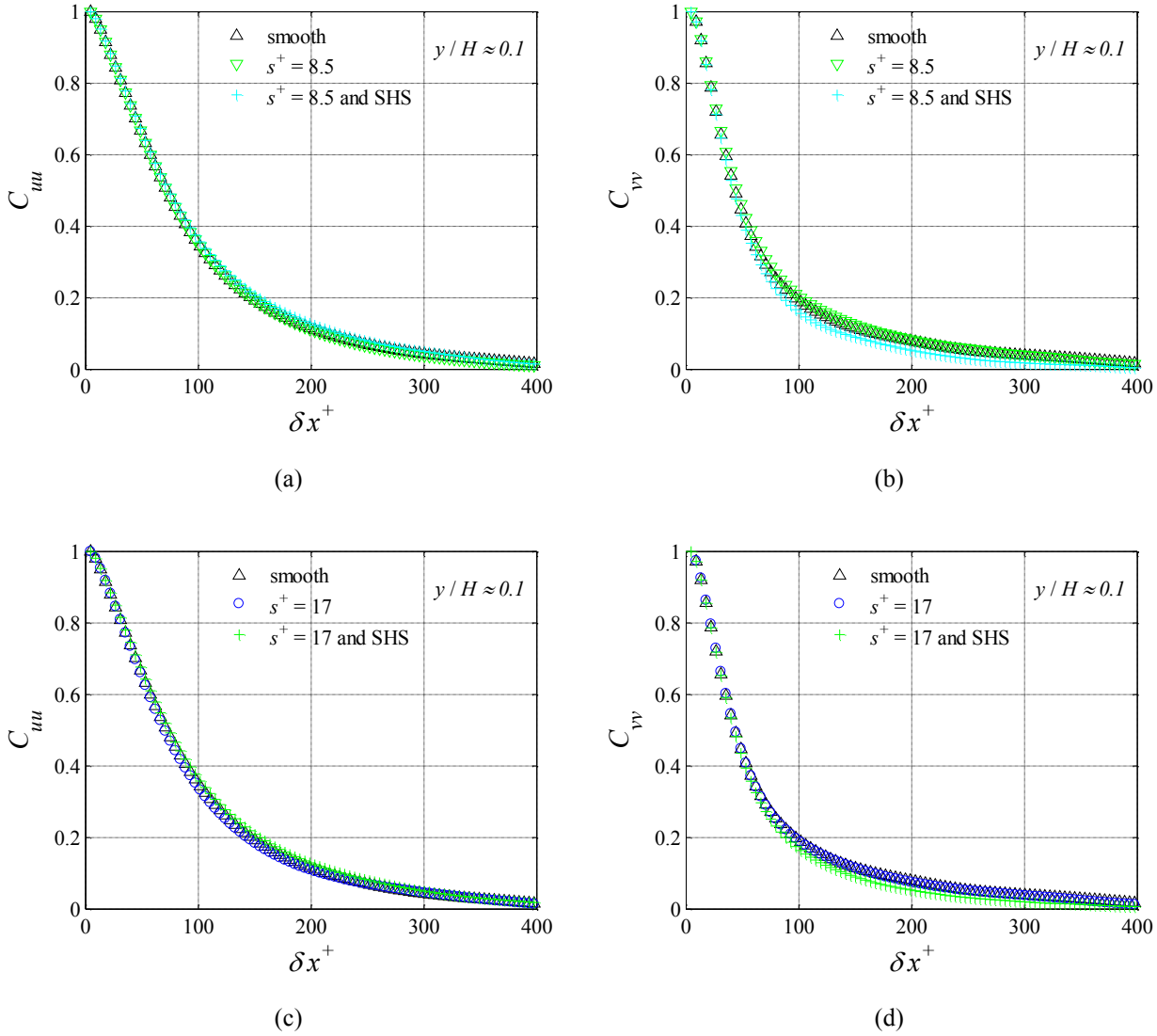

(a) (b)

(c) (d)

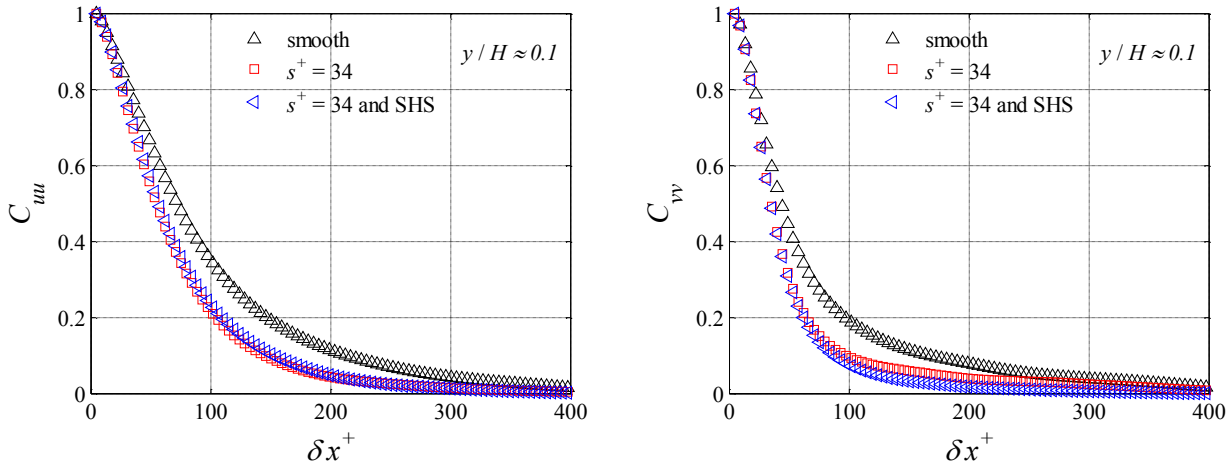

(e) (f)

Figure 5.14. Streamwise two-point correlations over the riblet surfaces with superhydrophobic coatings: (a) (c) (e) correlation of the streamwise velocity fluctuation at $y / H \approx 0.1$, (b) (d) (f) correlation of the wall-normal velocity fluctuation at $y / H \approx 0.1$.

Quadrant plots for coated riblet surfaces are shown in Figure 5.15. In the case of coated riblets of $s^+ = 8.5$ and $s^+ = 17$ shown in Figure 5.15 (a) and (b), the plots are skewed. The area of each level of the contour for the ejection event is maintained the same, while the sweep events are slightly decreased over the non-coated compared to the events over the coated surfaces. The four quadrants stay the same on the riblet surface at $s^+ = 34$ after coating. Such observation is agreement with the quadrant analysis of the coated smooth surface in Figure 5.10. Though <*uv*> is reduced over the coated surfaces, the quadrant plots persist as the plots over the non-coated surfaces.

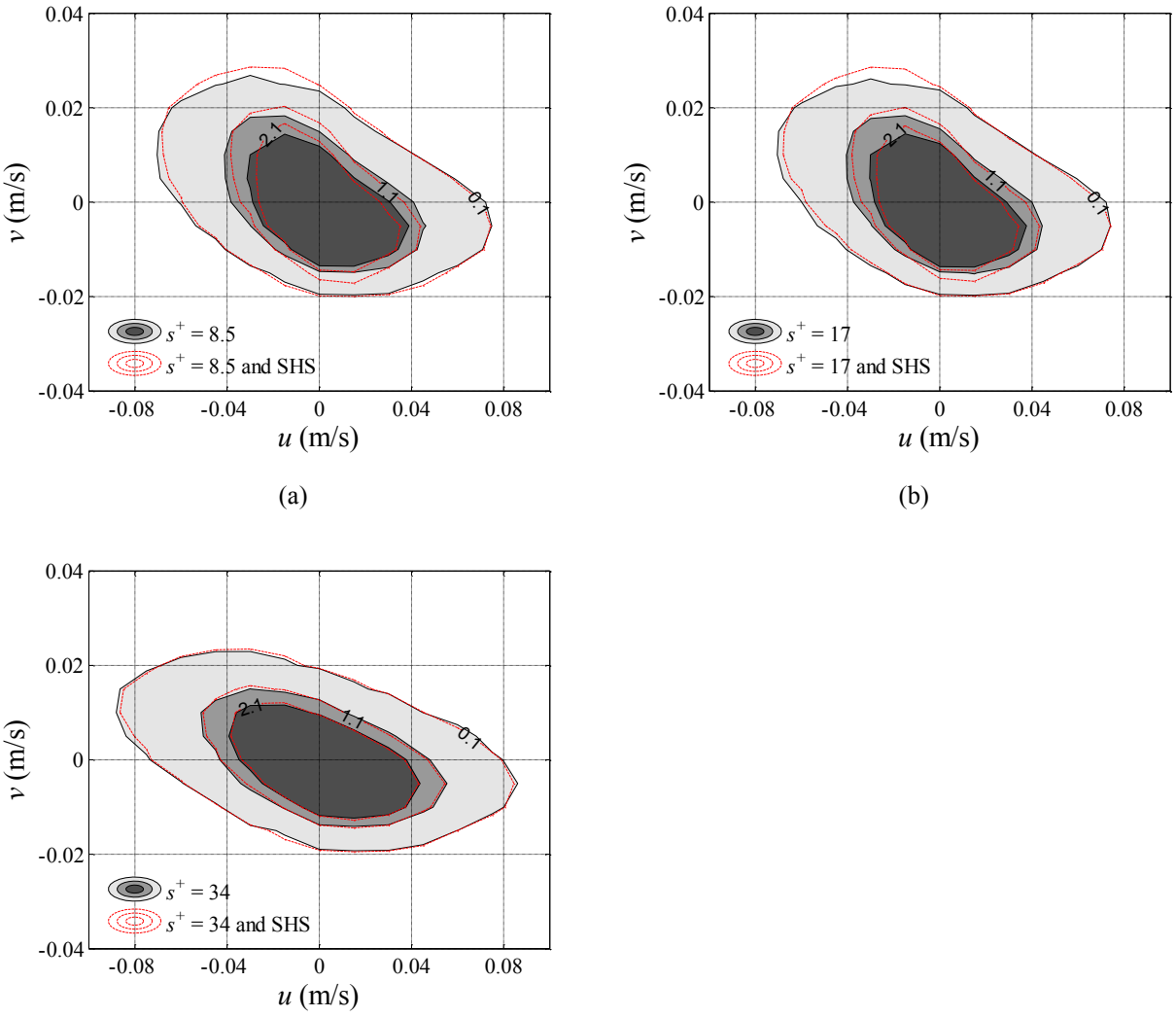

Figure 5.15. Quadrant plot of turbulent streamwise and wall-normal fluctuations at $y / H \approx 0.1$ over the riblet surfaces with superhydrophobic coatings. The dark gray, medium gray and light gray colors in the filled contours along with the red-line contours near each level of gray denote 2.1%, 1.1% and 0.1% probability density function values.

5.3 Longevity of superhydrophobic surfaces

Once the air pockets are depleted, the SHS will not be able to provide the shear-free regions which potentially help reduce the skin-friction. Therefore, the longevity of the SHSs determines the time period over which the SFR can be achieved (Govardhan et al. 2009; Samaha, Tafreshi, and Gad-el-Hak 2012). To investigate the longevity of the SHSs, convergence plots of $\langle u^2 \rangle$, $\langle v^2 \rangle$ and $\langle uv \rangle$ at different wall-normal locations are examined. $\langle u^2 \rangle$ at $y / H \sim 0.05$ is chosen because the alternations of $\langle u^2 \rangle$ in all cases is discernable at this location close to the wall and the measurement is right out of the errorneous range ($y / H < 0.02$). For $\langle v^2 \rangle$, the convergence plot is provided at the top peak location at $y / H \sim 0.2$ where the differences of $\langle v^2 \rangle$ over different surfaces reach maximum. Out of the same reason, Reynolds shear stress $\langle uv \rangle$ is investigated at $y / H \sim 0.1$ which is the peak location of $\langle uv \rangle$. All the chosen points are denoted as $\langle u_{top}^2 \rangle$, $\langle v_{top}^2 \rangle$ and $\langle uv_{top} \rangle$.

The convergence of $\langle u_{top}^2 \rangle$, $\langle v_{top}^2 \rangle$ and $\langle uv_{top} \rangle$ over the non-coated riblet and smooth surfaces are first scrutinized in order to see if there are variations with time, as shown in Figure 5.16 and Figure 5.17. From Figure 5.16 (a) and Figure 5.17 (a), it is seen $\langle u_{top}^2 \rangle$ is stable and statistical convergence is achieved after 200 seconds. Note that the different levels of $\langle u_{top}^2 \rangle$ are due to different wall location in each case. $\langle v_{top}^2 \rangle$ in Figure 5.16 (b) and Figure 5.17 (b) are fluctuating in a large range relative to the magnitude of $\langle v_{top}^2 \rangle$. For $\langle uv_{top} \rangle$, as shown in Figure 5.16 (c) and Figure 5.17 (c), the relative fluctuation is even greater than $\langle v_{top}^2 \rangle$.

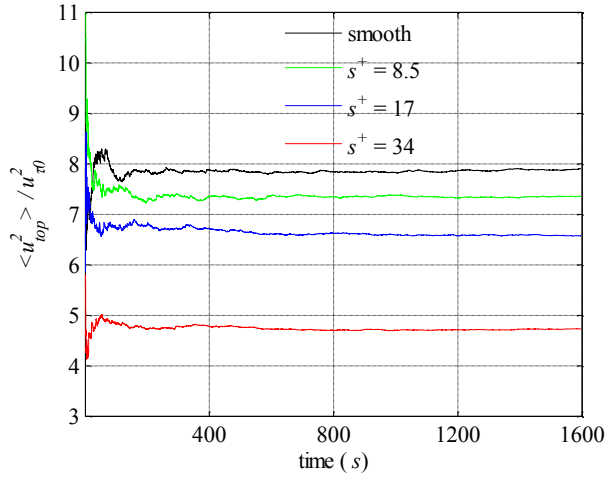

(a)

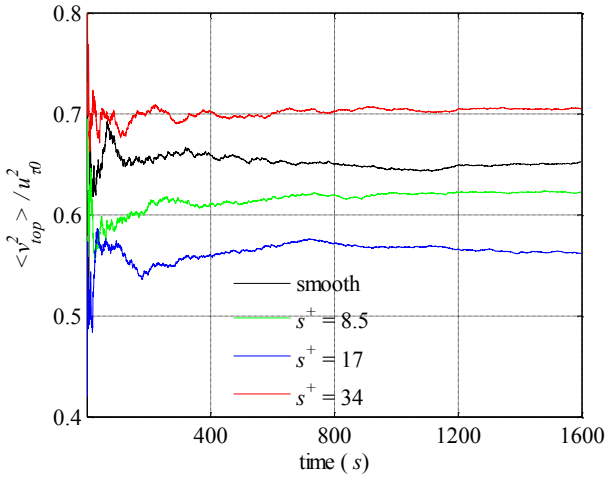

(b)

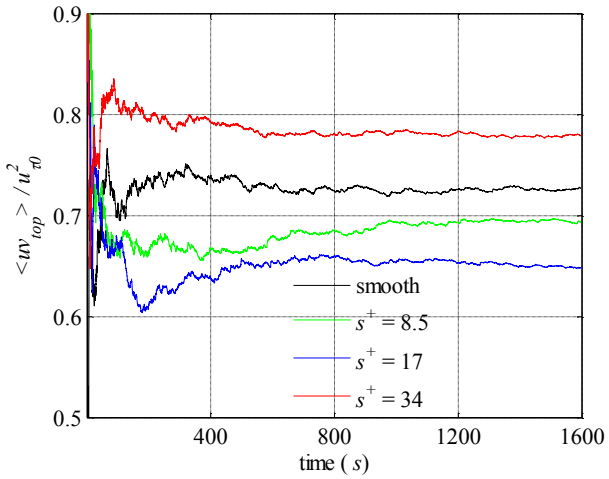

(c)

Figure 5.16. Convergent plots of $<u_{top}^2>$, $<v_{top}^2>$ and $<uv_{top}>$ over the riblet surfaces. (a) $<u_{top}^2>$, (b) $<v_{top}^2>$, (c) $<uv_{top}>$.

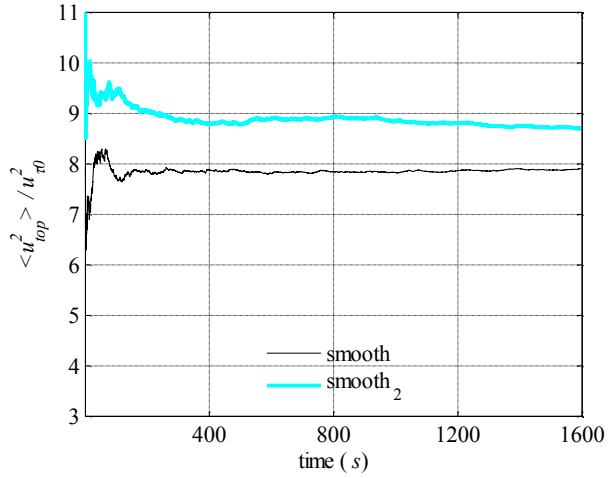

(a)

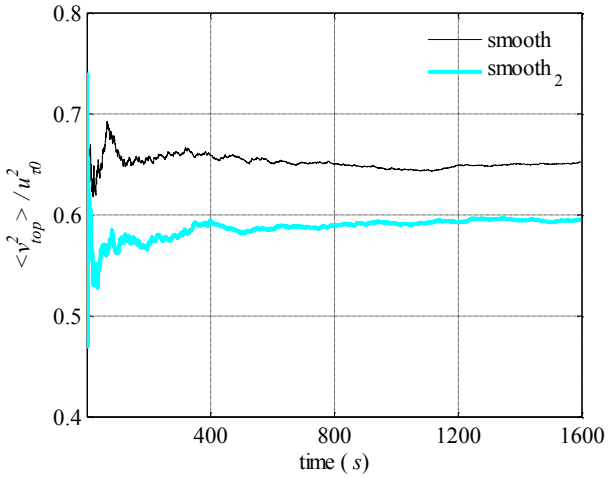

(b)

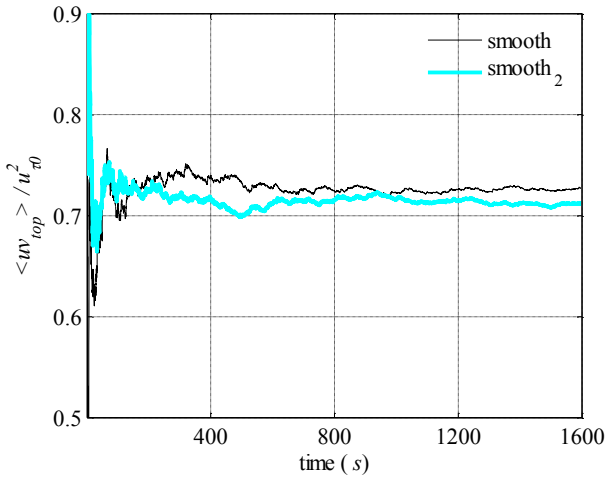

(c)

Figure 5.17. Convergent plots of $<u_{top}^2>$, $<v_{top}^2>$ and $<uv_{top}>$ in the smooth surface tests. (a) $<u_{top}^2>$, (b) $<v_{top}^2>$, (c) $<uv_{top}>$.

The convergence over coated surfaces on the base of smooth surface and riblet surfaces are examined.

For the coated smooth surface, $<u_{top}^2>$ in Figure 5.18 (a) shows an apparent increase till about 500 seconds. This trend does not show up in any of the non-coated surfaces in Figure 5.16 (a) and Figure 5.17 (a) and can be taken as a change of the performance of the SHS. Before 500 seconds in the measurement, the air layers in SHS were working to suppress the turbulence intensities but they gradually depleted, resulting in the increase of $<u^2>$. After 500 seconds, the SHS is not able to continually help reduce the turbulence intensity therefore the magnitude of $<u_{top}^2>$ no longer changed with time. The increase of $<v_{top}^2>$ up to 600 seconds as shown in Figure 5.18 (b) also suggests the longevity of SHS but the sensitive $<v^2>$ and its large fluctuations reduces the reliability of $<v_{top}^2>$ as a measure of longevity, as indicated above in Figure 5.16 (b) and Figure 5.17 (b). Similar to the $<v_{top}^2>$, the fluctuation of $<uv_{top}>$ appears in Figure 5.18 (c) but it lacks confidence in determining the longevity of SHS.

For coated riblet at $s^+ = 8.5$, increase of $<u_{top}^2>$ is spotted until 1200s in Figure 5.19 (a). However, the increase is too small compared to that in Figure 5.18 (a), which can be considered as additional evidence that SHS does not provide additional SFR over this size of riblets. Due to the larger variations with time and the sensitive properties, $<v_{top}^2>$ and $<uv_{top}>$ in Figure 5.19 (b) and (c) are not taken as valid measure as before.

In case of coated riblets at $s^+ = 17$, $<u_{top}^2>$ in Figure 5.20 (a) is noticed to have an increase change till about 800 seconds, indicating the working period of SHSs. Compared to the result in Figure 5.19 (a), the longevity is decreased. This short time is possibly one of the reasons that no discernable SFR change is observed in this case.

As is shown in Figure 5.21 (a), $<u_{top}^2>$ on the coated riblets at $s^+ = 34$ stays flat as that on the smooth surface and non-coated riblets. It is assumed that SFR is achieved because the air pockets in SHS have not been lost during the measurement.

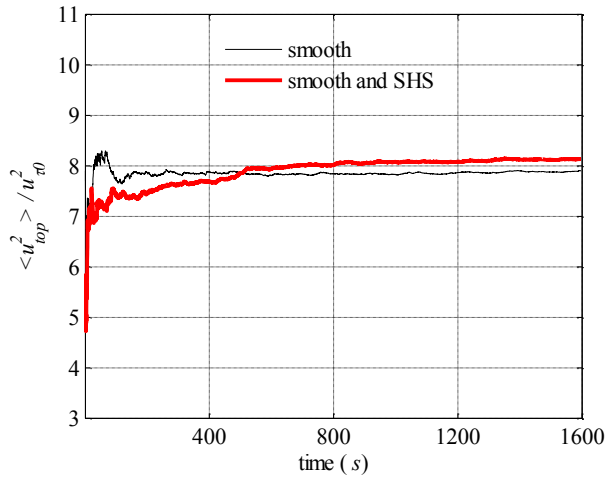

(a)

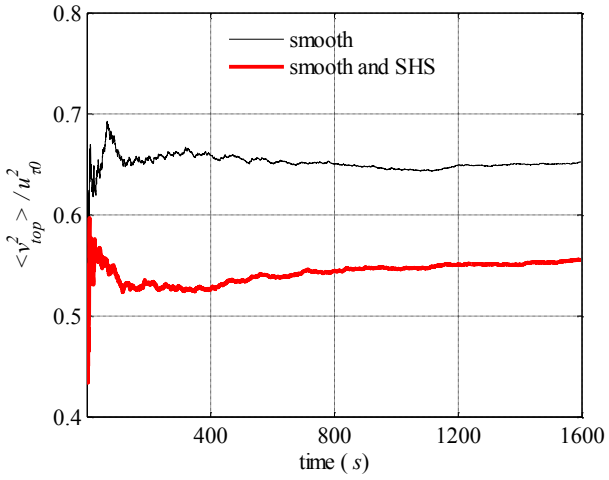

(b)

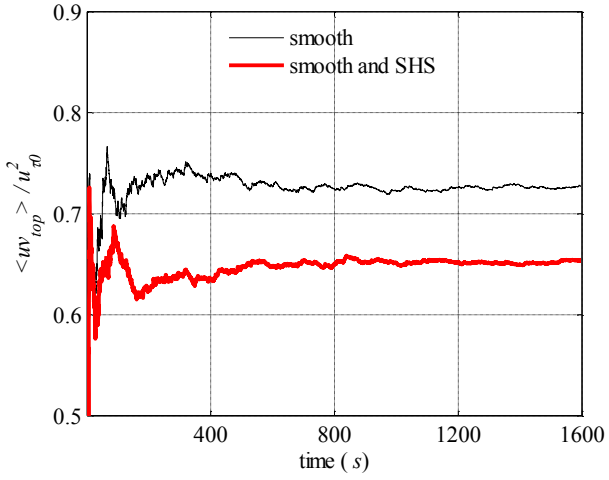

(c)

Figure 5.18. Convergent plots of $<u_{top}^2>$, $<v_{top}^2>$ and $<uv_{top}>$ over the smooth surface with superhydrophobic coatings. (a) $<u_{top}^2>$, (b) $<v_{top}^2>$, (c) $<uv_{top}>$.

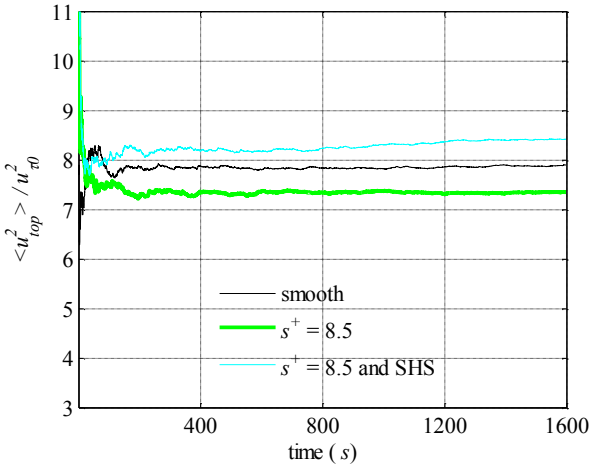

(a)

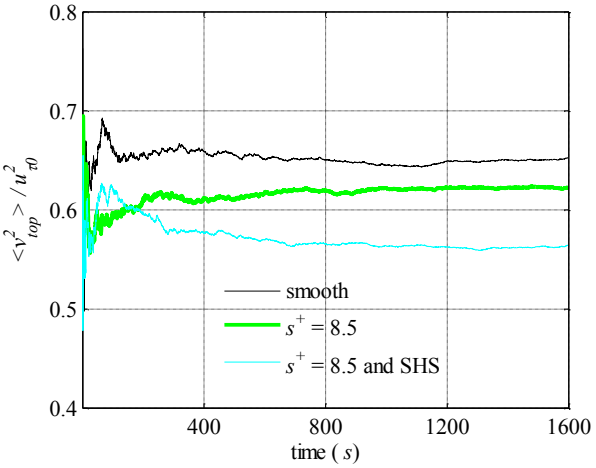

(b)

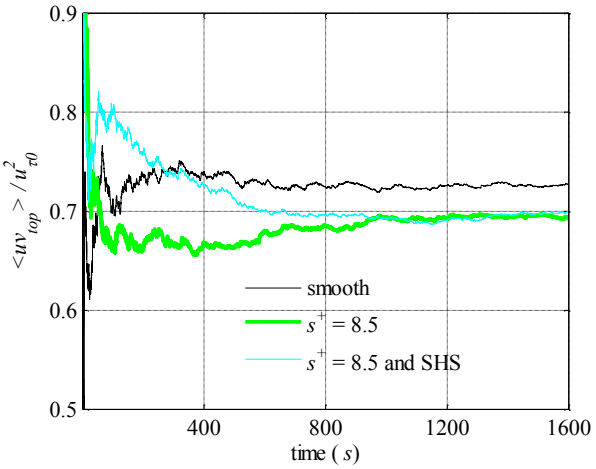

(c)

Figure 5.19. Convergent plots of $<u_{top}^2>$, $<v_{top}^2>$ and $<uv_{top}>$ over the riblet surface at $s^+ = 8.5$ with superhydrophobic coatings. (a) $<u_{top}^2>$, (b) $<v_{top}^2>$, (c) $<uv_{top}>$.

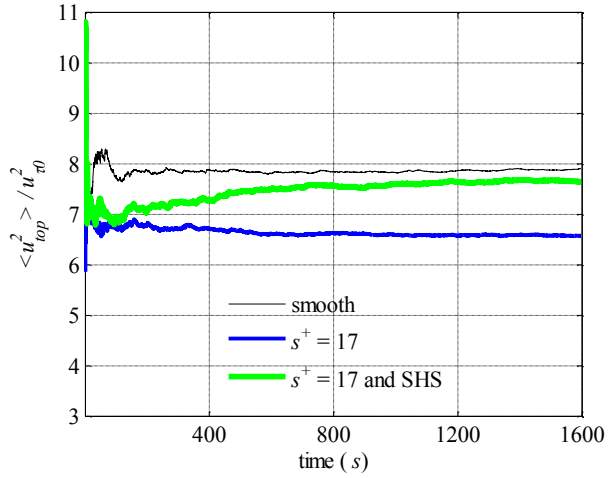

(a)

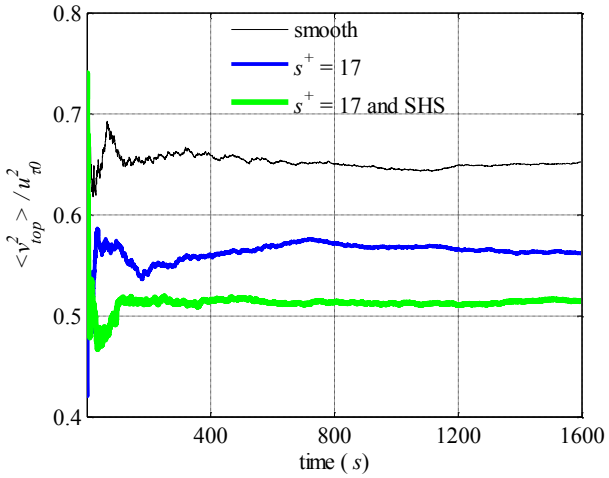

(b)

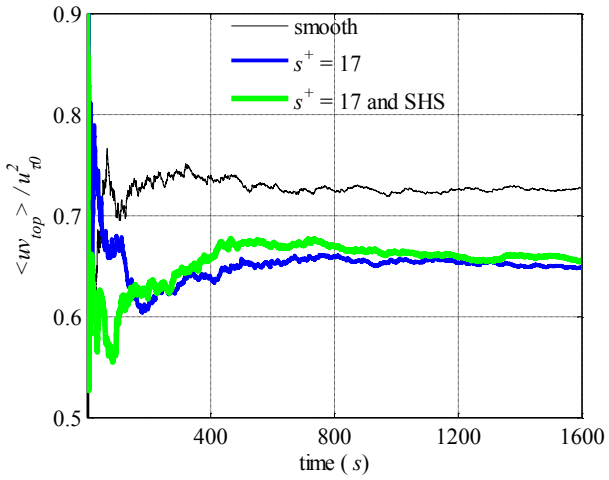

(c)

Figure 5.20. Convergent plots of $<u_{top}^2>$, $<v_{top}^2>$ and $<uv_{top}>$ over the riblet surface at $s^+ = 17$ with superhydrophobic coatings. (a) $<u_{top}^2>$, (b) $<v_{top}^2>$, (c) $<uv_{top}>$.

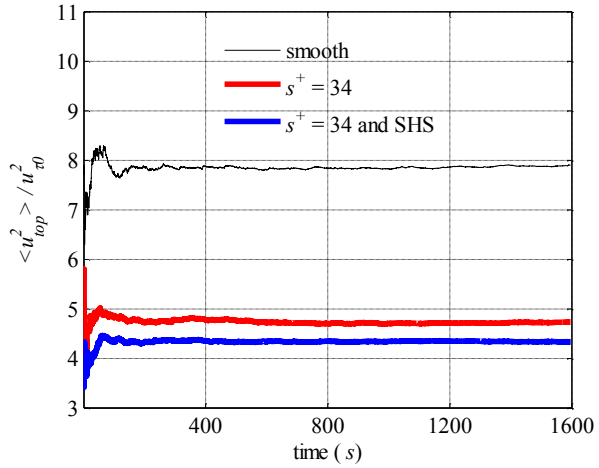

(a)

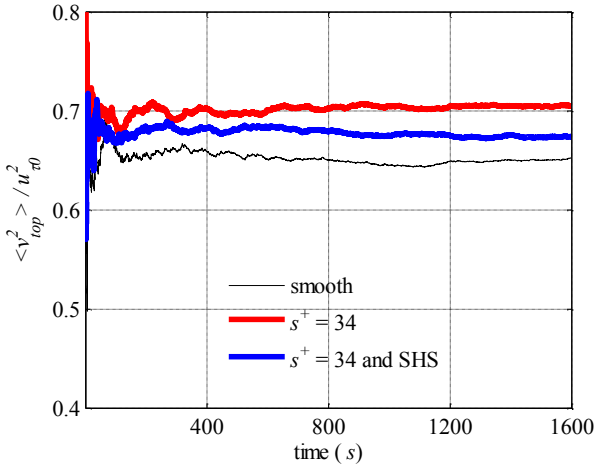

(b)

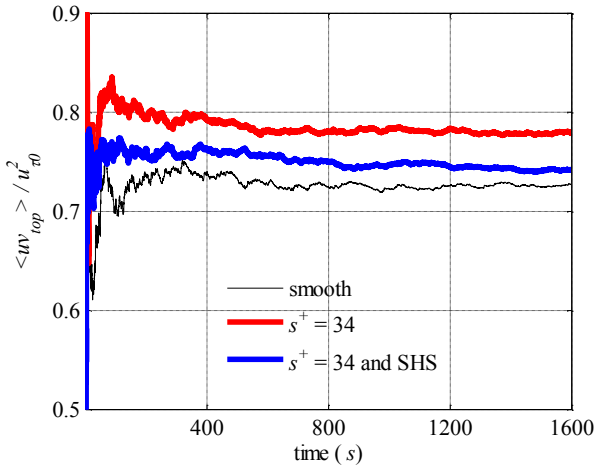

(c)

Figure 5.21. Convergent plots of $<u_{top}^2>$, $<v_{top}^2>$ and $<uv_{top}>$ over the riblet surface at $s^+ = 34$ with superhydrophobic coatings. (a) $<u_{top}^2>$, (b) $<v_{top}^2>$, (c) $<uv_{top}>$.

5.4 Conclusion

In order to observe if skin-friction reduction can be achieved by applying a superhydrophobic layer over a riblet surface, measurements over non-coated riblet surface (at three dimensions of s^+ = 8.5, 17 and 34) and the corresponding coated riblet surfaces, were carried out using planar PIV. The variations of skin-friction are scrutinized by observing changes of Reynolds shear stress.

SHS over the smooth wall provides SFR as both change of turbulence intensities and two-point correlations values follow the same trends as shown in SFR riblet surface. The convergence analysis of the streamwise velocity fluctuation shows a gradual disappearance of air pockets over the surface.

The riblet surfaces at s^+ = 8.5 and 17 are proven to reduce skin-friction while SFI is observed in the case of s^+ = 34. The riblet surfaces with superhydrophobic coatings show limited benefit in comparison with the riblet surfaces. The coated riblet surfaces at s^+ = 8.5 and 17 provide no extra SFR. For the coated riblets at s^+ = 34, Reynolds shear stress is suppressed relative to the non-coated surface, showing the potential of SFR in over-sized riblets coated with a superhydrophobic layer. At the same time, reduction of the streamwise turbulence intensity and increase of the mean velocity in the near wall region over this coated surface also suggest reduction of skin-friction. The observation is in agreement with the conjecture that the performance of riblets at SFI regime can be improved with the superhydrophobic coatings. The longevity analysis shows a longer persistence of SHSs over all the riblets, which is possibly a result of weaker flows in the riblet regions.

Chapter 6. Conclusion

The performances of the two dimensional and three dimensional PIV and PTV in measuring turbulent flows over a riblet surface have been evaluated. SFR has been calculated to be 6.1% from the velocity measurement in the viscous sublayer and to be 7.4% from the profiles of the Reynolds shear stress for trapezoidal riblet of $s^+ = 11$, $h / s = 0.5$ and $\alpha = 30^\circ$. The reduction is compatible with the 6% SFR reported by Bechert et al. (1997) over the surface with same riblets. The attenuations of the turbulence intensities above the riblets are observed to be 5.9%, 9.4% and 9.4% for streamwise, wall-normal and spanwise components. Measurement errors are calculated to be 0.24 pixels for wall-normal velocity fluctuation by planar PIV and 0.34 pixels for spanwise velocity fluctuation by 3D-PTV. Three components of vorticity over the riblet surface are first shown with tomo-PIV measurement in experimental riblet study but no change is spotted compared to the vorticities over the smooth surface due to the large measurement errors in the calculation of the velocity gradients fields. The divergence of the velocity field is calculated from tomo-PIV to be 0.04 voxel/voxel (Scarano et al. 2006). The detailed quadrant analysis from 2D-PIV is able to capture the attenuation of ejection and sweep. The streamwise two-point correlations are available from planar PIV showing the increase of organization of the high speed and low speed streaks over the riblets wall.

In order to observe if the skin-friction reduction can be achieved by coating superhydrophobic layers over riblets, measurements over non-coated riblet surface at three dimensions ($s^+ = 8.5$, 17 and 34) and the corresponding coated riblet surfaces were carried out with a planar PIV. The alternations of skin-friction are scrutinized by observing changes of Reynolds shear stress.

Superhydrophobic coating over the smooth wall provides SFR as both change of turbulence intensities and two-point correlations values follow the same trends as shown in SFR riblet surface. The convergence analysis of the streamwise velocity fluctuation shows a gradual disappearance of air pockets over the surface.

The riblet surfaces at $s^+ = 8.5$ and 17 are proven to reduce skin-friction and SFI is observed in the case of $s^+ = 34$. The riblet surfaces with superhydrophobic coatings show limited benefit in comparison with the riblet surfaces. The coated riblet surfaces at $s^+ = 8.5$ and 17 provide no extra

SFR. For the coated riblets at $s^+ = 34$, Reynolds shear stress is suppressed relative to the non-coated surface, showing the potential of SFR in large scale riblets combined with SHSs. At the same time, reduction of the streamwise turbulence intensity and increase of the mean velocity in the near wall region over this coated surface also suggest reduction of skin-friction. The observation is in agreement with the conjecture that the performance of riblets at SFI regime can be improved with the superhydrophobic coatings. The longevity analysis shows a longer persistence of SHSs over all the riblets, which is possibly a result of weaker flows in the riblet regions.

Recommendations for future research

Based on the literature and studies in this thesis, the following three aspects can be considered in future works:

-Carry out pressure drop measurement along with PIV and PTV measurements in SFR studies. In this way, skin-friction can be calculated directly from pressure drop to avoid the uncertainty brought in when calculating the velocity gradients in the viscous sublayer and the slopes of the Reynolds shear stress profile, as mentioned in section 4.2.

-Apply PIV measurement in streamwise and spanwise plane over riblet surfaces to learn about the changes of length-scales and streamwise vorticity. Since riblets are known to alter the spanwise motions to reduce drag, it is worth observing turbulent statistics in spanwise direction.

-Employ high-speed camera in studies involving SHSs. The longevity of SHSs is a critical factor that determines their SFR performances. To decrease the effect of gradual loss of SHS, a shorter period of measurement will help to have less biased results.

Bibliography

Abdulbari, H. A., R. M. Yunus, N. H. Abdurahman, and A. Charles. 2013. "Going against the flow—A Review of Non-Additive Means of Drag Reduction." *Journal of Industrial and Engineering Chemistry* 19 (1). The Korean Society of Industrial and Engineering Chemistry: 27–36. doi:10.1016/j.jiec.2012.07.023.

Baek, S. J., and S. J. Lee. 1996. "A New Two-Frame Particle Tracking Algorithm Using Match Probability." *Experiments in Fluids* 22 (1): 23–32. doi:10.1007/BF01893303.

Barbier, C., E. Jenner, and B. D'Urso. 2012. "Drag Reduction With Superhydrophobic Riblets." In *ASME 2012 International Mechanical Engineering Congress and Exposition*, 199–205. Houston: ASME. doi:10.1115/IMECE2012-86029.

Bechert, D. W., and M. Bartenwerfer. 1989. "The Viscous Flow on Surfaces with Longitudinal Ribs." *Journal of Fluid Mechanics* 206 (September): 105–29. doi:10.1017/S0022112089002247.

Bechert, D. W., M. Bruse, W. Hage, J. G. T. Van Der Hoeven, and G. Hoppe. 1997. "Experiments on Drag-Reducing Surfaces and Their Optimization with an Adjustable Geometry." *Journal of Fluid Mechanics* 338 (May): 59–87. doi:10.1017/S0022112096004673.

Bidkar, R. A., L. Leblanc, A. J. Kulkarni, V. Bahadur, S. L. Ceccio, and M. Perlin. 2014. "Skin-Friction Drag Reduction in the Turbulent Regime Using Random-Textured Hydrophobic Surfaces." *Physics of Fluids* 26 (8): 85108. doi:10.1063/1.4892902.

Blackwelder, R. F., and H. Eckelmann. 1979. "Streamwise Vortices Associated with the Bursting Phenomenon." *Journal of Fluid Mechanics* 94 (3): 577–94. doi:10.1017/S0022112079001191.

Byun, D., J. Kim, H. S. Ko, and H. C. Park. 2008. "Direct Measurement of Slip Flows in Superhydrophobic Microchannels with Transverse Grooves." *Physics of Fluids* 20 (11): 113601. doi:10.1063/1.3026609.

Chen, H., F. Rao, Xi. Shang, D. Zhang, and I. Hagiwara. 2014. “Flow over Bio-Inspired 3D Herringbone Wall Riblets.” *Experiments in Fluids* 55 (3): 1698. doi:10.1007/s00348-014-1698-4.

Choi, H., P. Moin, and J. Kim. 1991. “On the Effect of Riblets in Fully Developed Laminar Channel Flows.” *Physics of Fluids A: Fluid Dynamics* 3 (8): 1892. doi:10.1063/1.857918.

Choi, H., P. Moin, and J. Kim. 1993. “Direct Numerical Simulation of Turbulent Flow over Riblets.” *Journal of Fluid Mechanics* 255 (October): 503–39. doi:10.1017/S0022112093002575.

Choi, K. 1989. “Near-Wall Structure of a Turbulent Boundary Layer with Riblets.” *Journal of Fluid Mechanics* 208 (November): 417–58. doi:10.1017/S0022112089002892.

Chu, D. C., and G. E. Karniadakis. 1993. “A Direct Numerical Simulation of Laminar and Turbulent Flow over Riblet-Mounted Surfaces.” *Journal of Fluid Mechanics* 250 (May): 1–42. doi:10.1017/S0022112093001363.

Daniello, R. J., N. E. Waterhouse, and J. P. Rothstein. 2009. “Drag Reduction in Turbulent Flows over Superhydrophobic Surfaces.” *Physics of Fluids* 21 (8): 85103. doi:10.1063/1.3207885.

Davies, J., D. Maynes, B. W. Webb, and B. Woolford. 2006. “Laminar Flow in a Microchannel with Superhydrophobic Walls Exhibiting Transverse Ribs.” *Physics of Fluids* 18 (8): 87110. doi:10.1063/1.2336453.

Dean, R. B. 1978. “Reynolds Number Dependence of Skin Friction and Other Bulk Flow Variables in Two-Dimensional Rectangular Duct Flow.” *Journal of Fluids Engineering* 100 (2): 215–23. doi:10.1115/1.3448633.

Den Toonder, J. M. J., M. A. Hulsen, G. D. C. Kuiken, and F. T. M. Nieuwstadt. 1997. “Drag Reduction by Polymer Additives in a Turbulent Pipe Flow: Numerical and Laboratory Experiments.” *Journal of Fluid Mechanics* 337 (April): 193–231. doi:10.1017/S0022112097004850.

Deutsch, S., M. Moeny, A. A. Fontaine, and H. Petrie. 2004. “Microbubble Drag Reduction in

Rough Walled Turbulent Boundary Layers with Comparison against Polymer Drag Reduction." *Experiments in Fluids* 37 (5): 731–44. doi:10.1007/s00348-004-0863-6.

Dilip, D., M. S. Bobji, and R. N. Govardhan. 2015. "Effect of Absolute Pressure on Flow through a Textured Hydrophobic Microchannel." *Microfluidics and Nanofluidics* 19 (6). Springer Berlin Heidelberg: 1409–27. doi:10.1007/s10404-015-1655-4.

Duan, L., and M. Choudhari. 2012. "Effects of Riblets on Skin Friction and Heat Transfer in High-Speed Turbulent Boundary Layers." In *50th AIAA Aerospace Sciences Meeting Including the New Horizons Forum and Aerospace Exposition*, 1–15. Reston, Virigina: American Institute of Aeronautics and Astronautics. doi:10.2514/6.2012-1108.

El-Samni, O. A., H. H. Chun, and H. S. Yoon. 2007. "Drag Reduction of Turbulent Flow over Thin Rectangular Riblets." *International Journal of Engineering Science* 45 (2–8): 436–54. doi:10.1016/j.ijengsci.2007.03.002.

Elsinga, G. E., R. J. Adrian, B. W. Van Oudheusden, and F. Scarano. 2010. "Three-Dimensional Vortex Organization in a High-Reynolds-Number Supersonic Turbulent Boundary Layer." *Journal of Fluid Mechanics* 644 (February): 35–60. doi:10.1017/S0022112009992047.

Elsinga, G. E., F. Scarano, B. Wieneke, and B. W. van Oudheusden. 2006. "Tomographic Particle Image Velocimetry." *Experiments in Fluids* 41 (6): 933–47. doi:10.1007/s00348-006-0212-z.

Fazle Hussain, A. K. M. 1986. "Coherent Structures and Turbulence." *Journal of Fluid Mechanics* 173: 303–56. doi:10.1017/S0022112086001192.

Fiedler, H. E. 1988. "Coherent Structures in Turbulent Flows." *Progress in Aerospace Sciences* 25 (3): 231–69. doi:10.1016/0376-0421(88)90001-2.

Fukagata, K., N. Kasagi, and P. Koumoutsakos. 2006. "Erratum: 'A Theoretical Prediction of Friction Drag Reduction in Turbulent Flow by Superhydrophobic Surfaces.'" *Physics of Fluids* 18 (8): 89901. doi:10.1063/1.2337090.

Gad-el-Hak, M. 2013. "Comment on 'Experimental Study of Skin Friction Drag Reduction on Superhydrophobic Flat Plates in High Reynolds Number Boundary Layer Flow' [Phys.

Fluids 25, 025103 (2013)].” *Physics of Fluids* 25 (7): 79101. doi:10.1063/1.4816362.

Garcia-Mayoral, R., and J. Jimenez. 2011. “Drag Reduction by Riblets.” *Philosophical Transactions of the Royal Society A: Mathematical, Physical and Engineering Sciences* 369 (1940): 1412–27. doi:10.1098/rsta.2010.0359.

Goldstein, D., R. Handler, and L. Sirovich. 1995. “Direct Numerical Simulation of Turbulent Flow over a Modeled Riblet Covered Surface.” *Journal of Fluid Mechanics* 302 (November): 333–76. doi:10.1017/S0022112095004125.

Golovin, K. B., J. W. Gose, M. Perlin, S. L. Ceccio, and A. Tuteja. 2016. “Bioinspired Surfaces for Turbulent Drag Reduction.” *Philosophical Transactions of the Royal Society A: Mathematical, Physical and Engineering Sciences* 374 (2073): 20160189. doi:10.1098/rsta.2016.0189.

Govardhan, R. N., G. S. Srinivas, A. Asthana, and M. S. Bobji. 2009. “Time Dependence of Effective Slip on Textured Hydrophobic Surfaces.” *Physics of Fluids* 21 (5): 52001. doi:10.1063/1.3127123.

Grüneberger, R., and W. Hage. 2011. “Drag Characteristics of Longitudinal and Transverse Riblets at Low Dimensionless Spacings.” *Experiments in Fluids* 50 (2): 363–73. doi:10.1007/s00348-010-0936-7.

Guezennec, Y. G., U. Piomelli, and J. Kim. 1989. “On the Shape and Dynamics of Wall Structures in Turbulent Channel Flow.” *Physics of Fluids A: Fluid Dynamics* 1 (4): 764. doi:10.1063/1.857373.

Harris, J. 2012. “Investigation of Relative Importance of Some Error Sources in Particle Image Velocimetry.” Utah State University.

Hooshmand, A., R. Youngs, J. M. Wallace, and J. L. Balint. 1983. “An Experimental Study of Changes in the Structure of a Turbulent Boundary Layer due to Surface Geometry Changes.” In *21st Aerospace Sciences Meeting*, 230. Reston, Virigina: American Institute of Aeronautics and Astronautics. doi:10.2514/6.1983-230.

Isaev, S A, A I Leontiev, and N A Kudryavtsev. 2005. “Numerical Simulation of Unsteady-State

Heat Transfer under Conditions of Laminar Transverse Flow Past a Circular Cylinder - Isaev, Leontiev, Kudryavtsev, Baranova, Lysenko.pdf." *High Temperature* 43 (5): 746–59.

Jahanmiri, M. 2011. "Particle Image Velocimetry: Fundamentals and Its Applications." Göteborg. http://publications.lib.chalmers.se/records/fulltext/138219.pdf\npapers2://publication/uuid/94E7A75B-9FE1-4D7A-984D-897C3E5AD24E.

Jelly, T. O., S. Y. Jung, and T. A. Zaki. 2014. "Turbulence and Skin Friction Modification in Channel Flow with Streamwise-Aligned Superhydrophobic Surface Texture." *Physics of Fluids* 26 (9): 95102. doi:10.1063/1.4894064.

Jimenez, J. 1992. "Wall Friction and the Structure of near-Wall Turbulence." In *11th Australasian Fluid Mechanics Conference*, edited by M.R.Davis and G.J.Walker, 813–16. Hobart.

Jimenez, J. 2004. "Turbulent Flows over Rough Walls." *Annual Review of Fluid Mechanics* 36 (1): 173–96. doi:10.1146/annurev.fluid.36.050802.122103.

Joseph, P., C. Cottin-Bizonne, J. M. Benoît, C. Ybert, C. Journet, P. Tabeling, and L. Bocquet. 2006. "Slippage of Water Past Superhydrophobic Carbon Nanotube Forests in Microchannels." *Physical Review Letters* 97 (15): 156104. doi:10.1103/PhysRevLett.97.156104.

Kähler, Ch. J., S. Scharnowski, and C. Cierpka. 2012. "On the Uncertainty of Digital PIV and PTV near Walls." *Experiments in Fluids* 52 (6): 1641–56. doi:10.1007/s00348-012-1307-3.

Kasagi, N., Y. Sumitani, Y. Suzuki, and O. Iida. 1995. "Kinematics of the Quasi-Coherent Vortical Structure in near-Wall Turbulence." *International Journal of Heat and Fluid Flow* 16 (1): 2–10. doi:10.1016/0142-727X(94)00006-X.

Kim, H., M. Moon, and K. Kim. 2011. "Multi-Objective Optimization of a Cooling Channel with Staggered Elliptic Dimples." *Energy* 36 (5). Elsevier Ltd: 3419–28. doi:10.1016/j.energy.2011.03.043.

Kim, J., P. Moin, and R. Moser. 1987. "Turbulence Statistics in Fully Developed Channel Flow at Low Reynolds Number." *Journal of Fluid Mechanics* 177: 133–66.

doi:10.1017/S0022112087000892.

Kim, S. H. 2008. “Fabrication of Superhydrophobic Surfaces.” *Journal of Adhesion Science and Technology* 22 (3–4): 235–50. doi:10.1163/156856108X305156.

Kline, S. J., W. C. Reynolds, F. A. Schraub, and P. W. Runstadler. 1967. “The Structure of Turbulent Boundary Layers.” *Journal of Fluid Mechanics* 30 (4): 741–73. doi:10.1017/S0022112067001740.

Kolehmainen, Jari, Jouni Elfvengren, Markku Ylönen, and Pentti Saarenrinne. 2014. “PTV and PIV Based Dispersed Phase Velocity Measurements in a Pseudo - 2D Turbulent Fluidized Bed.” *Proceedings of the International Conference on Heat Transfer and Fluid Flow*, no. 70: 70 1-9.

Kramer, F., R. Grueneberger, F. Thiele, E. Wassen, W. Hage, and R. Meyer. 2010. “Wavy Riblets for Turbulent Drag Reduction.” In *5th Flow Control Conference*, 1–10. Reston, Virigina: American Institute of Aeronautics and Astronautics. doi:10.2514/6.2010-4583.

Lam, L. S., C. Melnick, M. Hodes, G. Ziskind, and R. Enright. 2014. “Nusselt Numbers for Thermally Developing Couette Flow With Hydrodynamic and Thermal Slip.” *Journal of Heat Transfer* 136 (5): 51703. doi:10.1115/1.4026305.

Latthe, S., C. Terashima, K. Nakata, and A. Fujishima. 2014. “Superhydrophobic Surfaces Developed by Mimicking Hierarchical Surface Morphology of Lotus Leaf.” *Molecules* 19 (4): 4256–83. doi:10.3390/molecules19044256.

Lauga, E., and H. A. Stone. 2003. “Effective Slip in Pressure-Driven Stokes Flow.” *Journal of Fluid Mechanics* 489 (July): 55–77. doi:10.1017/S0022112003004695.

Lee, S., and Y. Choi. 2008. “Decrement of Spanwise Vortices by a Drag-Reducing Riblet Surface.” *Journal of Turbulence* 9 (April 2013): 1–15. doi:10.1080/14685240802251517.

Lee, S. J., and S. H. Lee. 2001. “Flow Field Analysis of a Turbulent Boundary Layer over a Riblet Surface.” *Experiments in Fluids* 30 (2): 153–66. doi:10.1007/s003480000150.

Lienhart, H., M. Breuer, and C. Köksoy. 2008. “Drag Reduction by Dimples? – A

Complementary Experimental/numerical Investigation." *International Journal of Heat and Fluid Flow* 29 (3): 783–91. doi:10.1016/j.ijheatfluidflow.2008.02.001.

Lumley, J. L. 1973. "Drag Reduction in Turbulent Flow by Polymer Additives." *Macromolecular Reviews* 7 (1969): 263–90.

Maali, A., Y. Pan, B. Bhushan, and E. Charlaix. 2012. "Hydrodynamic Drag-Force Measurement and Slip Length on Microstructured Surfaces." *Physical Review E* 85 (6): 66310. doi:10.1103/PhysRevE.85.066310.

Maas, H. G., A. Gruen, and D. Papantoniou. 1993. "Particle Tracking Velocimetry in Three-Dimensional Flows." *Experiments in Fluids* 15 (2): 133–46. doi:10.1007/BF00190953.

Martell, M. B., J. B. Perot, and J. P. Rothstein. 2009. "Direct Numerical Simulations of Turbulent Flows over Superhydrophobic Surfaces." *Journal of Fluid Mechanics* 620 (February): 31–41. doi:10.1017/S0022112008004916.

Martell, M. B., J. P. Rothstein, and J. B. Perot. 2010. "An Analysis of Superhydrophobic Turbulent Drag Reduction Mechanisms Using Direct Numerical Simulation." *Physics of Fluids* 22 (6): 65102. doi:10.1063/1.3432514.

Maynes, D., K. Jeffs, B. Woolford, and B. W. Webb. 2007. "Laminar Flow in a Microchannel with Hydrophobic Surface Patterned Microribs Oriented Parallel to the Flow Direction." *Physics of Fluids* 19 (9): 93603. doi:10.1063/1.2772880.

McCormick, M. E., and R. Bhattacharyya. 1973. "DRAG REDUCTION OF A SUBMERSIBLE HULL BY ELECTROLYSIS." *Naval Engineers Journal* 85 (2): 11–16. doi:10.1111/j.1559-3584.1973.tb04788.x.

Meinhart, C. D., S. T. Wereley, and J. G. Santiago. 2000. "A PIV Algorithm for Estimating Time-Averaged Velocity Fields." *Journal of Fluids Engineering* 122 (2): 285–89. doi:10.1115/1.483256.

Min, T., and J. Kim. 2004. "Effects of Hydrophobic Surface on Skin-Friction Drag." *Physics of Fluids* 16 (7): 0–3. doi:10.1063/1.1755723.

Min, T., J. Yul Yoo, H. Choi, and D. D. Joseph. 2003. “Drag Reduction by Polymer Additives in a Turbulent Channel Flow.” *Journal of Fluid Mechanics* 486 (June): 213–38. doi:10.1017/S0022112003004610.

Moin, P., and J. Kim. 1985. “The Structure of the Vorticity Field in Turbulent Channel Flow. Part 1. Analysis of Instantaneous Fields and Statistical Correlations.” *Journal of Fluid Mechanics* 155 (June): 441–64. doi:10.1017/S0022112085001896.

Navitar. 2016. “12X Zoom Performance Specifications | Navitar.” https://navitar.com/products/imaging-optics/high-magnification-imaging/12x-zoom/.

Norconk, M. P. 2011. “A Comprehensive Review and Application of Particle Image Velocimetry.” Michigan Technological University. http://digitalcommons.mtu.edu/etds/392.

Ou, J., B. Perot, and J. P. Rothstein. 2004. “Laminar Drag Reduction in Microchannels Using Ultrahydrophobic Surfaces.” *Physics of Fluids* 16 (12): 4635. doi:10.1063/1.1812011.

Ou, J., and J. P. Rothstein. 2005. “Direct Velocity Measurements of the Flow Past Drag-Reducing Ultrahydrophobic Surfaces.” *Physics of Fluids* 17 (10): 103606. doi:10.1063/1.2109867.

Pal, S., C. L. Merkle, and S. Deutsch. 1988. “Bubble Characteristics and Trajectories in a Microbubble Boundary Layer.” *Physics of Fluids* 31 (4): 744. doi:10.1063/1.866810.

Park, H., G. Sun, and C. Kim. 2014. “Superhydrophobic Turbulent Drag Reduction as a Function of Surface Grating Parameters.” *Journal of Fluid Mechanics* 747 (May): 722–34. doi:10.1017/jfm.2014.151.

Park, S., and J. M. Wallace. 1994. “Flow Alteration and Drag Reduction by Riblets in a Turbulent Boundary Layer.” *AIAA Journal* 32 (1): 31–38. doi:10.2514/3.11947.

Peguero, C., and K. Breuer. 2009. “On Drag Reduction in Turbulent Channel Flow over Superhydrophobic Surfaces.” In *Springer Proceedings in Physics*, 132:233–36. doi:10.1007/978-3-642-03085-7_57.

Perry, A. E., and P. N. Joubert. 1963. “Rough-Wall Boundary Layers in Adverse Pressure

Gradients." *Journal of Fluid Mechanics* 17 (2): 193–211. doi:10.1017/S0022112063001245.

Pope, S. B. 2000. *Turbulent Flows*. Cambridge University Press.

Prasad, A. K. 2000a. *Particle Image Velocimetry*. *Current Science*. Vol. 79. Berlin, Heidelberg. doi:10.1007/978-3-540-72308-0.

Prasad, A. K. 2000b. "Stereoscopic Particle Image Velocimetry." *Experiments in Fluids* 29 (2): 103–16. doi:10.1007/s003480000143.

Prince, J. F., D. Maynes, and J. Crockett. 2014. "Pressure Drop Measurements in Turbulent Channel Flow Over Superhydrophobic Surfaces With Riblets." In *ASME 2014 12th International Conference on Nanochannels, Microchannels and Minichannels*, V001T08A004. Chicago: ASME. doi:10.1115/ICNMM2014-21690.

Raffel, M., C. E. Willert, S. T. Wereley, and J. Kompenhans. 2007. *Particle Image Velocimetry*. *Springer*. Experimental Fluid Mechanics. Berlin, Heidelberg: Springer Berlin Heidelberg. doi:10.1007/978-3-540-72308-0.

Rastegari, A., and R. Akhavan. 2015. "On the Mechanism of Turbulent Drag Reduction with Super-Hydrophobic Surfaces." *Journal of Fluid Mechanics* 773 (June): R4. doi:10.1017/jfm.2015.266.

Robinson, S. K. 1991. "Coherent Motions in the Turbulent Boundary Layer." *Annual Review of Fluid Mechanics* 23 (1): 601–39. doi:10.1146/annurev.fl.23.010191.003125.

Roggenkamp, D., W. Li, P. Meysonnat, M. Klaas, and W. Schröder. 2015. "Experimental Analysis of Turbulent Friction Drag Reduction Due To Spanwise Transversal Surface Waves." In *International Symposium on Turbulence and Shear Flow Phenomena (TSFP-9)*. Melbourne.

Samaha, M. A., H. V. Tafreshi, and M. Gad-el-Hak. 2012. "Superhydrophobic Surfaces: From the Lotus Leaf to the Submarine." *Comptes Rendus Mécanique* 340 (1–2). Elsevier Masson SAS: 18–34. doi:10.1016/j.crme.2011.11.002.

Sareen, A., R. W. Deters, S. P. Henry, and M. S. Selig. 2014. "Drag Reduction Using Riblet Film

Applied to Airfoils for Wind Turbines." *Journal of Solar Energy Engineering* 136 (2). Reston, Virigina: American Institute of Aeronautics and Astronautics: 21007. doi:10.1115/1.4024982.

Sasamori, M., H. Mamori, K. Iwamoto, and A. Murata. 2014. "Experimental Study on Drag-Reduction Effect due to Sinusoidal Riblets in Turbulent Channel Flow." *Experiments in Fluids* 55 (10): 1828. doi:10.1007/s00348-014-1828-z.

Savins, J. G. 1964. "Drag Reduction Characteristics of Solutions of Macromolecules In Turbulent Pipe Flow." *Society of Petroleum Engineers Journal* 4 (3): 203–14. doi:10.2118/867-PA.

Scarano, F. 2013. "Tomographic PIV: Principles and Practice." *Measurement Science and Technology* 24 (1): 12001. doi:10.1088/0957-0233/24/1/012001.

Scarano, F., G. E. Elsinga, E. Bocci, and B. W. van Oudheusden. 2006. "Investigation of 3-D Coherent Structures in the Turbulent Cylinder Wake Using Tomo-PIV." In *13th International Symposium on Applications of Laser Techniques to Fluid Mechanics*. Lisbon.

Schlichting, H., and K. Gersten. 2000. *Boundary-Layer Theory*. 8thed. Springer-Verlag Berlin Heidelberg.

Schoppa, W., and F. Hussain. 2002. "Coherent Structure Generation in near-Wall Turbulence." *Journal of Fluid Mechanics* 453 (February): 57–108. doi:10.1017/S002211200100667X.

Smith, C. R., and S. P. Metzler. 1983. "The Characteristics of Low-Speed Streaks in the near-Wall Region of a Turbulent Boundary Layer." *Journal of Fluid Mechanics* 129 (April): 27–54. doi:10.1017/S0022112083000634.

Suzuki, Y., and N. Kasagi. 1994. "Turbulent Drag Reduction Mechanism above a Riblet Surface." *AIAA Journal* 32 (9): 1781–90. doi:10.2514/3.12174.

Toms, B. A. 1948. "Some Observations on the Flow of Linear Polymer Solutions through Straight Tubes at Large Reynolds Numbers." *Proceedings of the 1st International Congress on Rheology* 2: 135–41.

Tsukahara, T., Y. Seki, H. Kawamura, and D. Tochio. 2005. “DNS of Turbulent Channel Flow at Very Low Reynolds Numbers.” In *International Symposium on Turbulence and Shear Flow Phenomena (TSFP-4)*, 935–40. Williamsburg.

Vajdi Hokmabad, B., and S. Ghaemi. 2016. “Turbulent Flow over Wetted and Non-Wetted Superhydrophobic Counterparts with Random Structure.” *Physics of Fluids* 28 (1): 15112. doi:10.1063/1.4940325.

Virk, P. S. 1975. “Drag Reduction Fundamentals.” *AIChE Journal* 21 (4): 625–56. doi:10.1002/aic.690210402.

Vukoslavcevic, P., J. M. Wallace, and J. L. Balint. 1992. “Viscous Drag Reduction Using Streamwise-Aligned Riblets.” *AIAA Journal* 30 (4): 1119–22. doi:10.2514/3.11035.

Wallace, J. M., H. Eckelmann, and R. S. Brodkey. 1972. “The Wall Region in Turbulent Shear Flow.” *Journal of Fluid Mechanics* 54 (1): 39–48. doi:10.1017/S0022112072000515.

Walsh, M. J. 1979. “Drag Characteristics of V-Groove and Transverse Curvature Riblets.” In *Symposium on Viscous Flow Drag Reduction*, 168–84. Dallas.

Walsh, M. J. 1983. “Riblets as a Viscous Drag Reduction Technique.” *AIAA Journal* 21 (4): 485–86. doi:10.2514/3.60126.

Walsh, M., and A. Lindemann. 1984. “Optimization and Application of Riblets for Turbulent Drag Reduction.” In *22nd Aerospace Sciences Meeting*, 1–10. Reston, Virigina: American Institute of Aeronautics and Astronautics. doi:10.2514/6.1984-347.

Warholic, M. D., H. Massah, and T. J. Hanratty. 1999. “Influence of Drag-Reducing Polymers on Turbulence: Effects of Reynolds Number, Concentration and Mixing.” *Experiments in Fluids* 27 (5): 461–72. doi:10.1007/s003480050371.

Weiss, M. H. 1997. “Implementation of Drag Reduction Techniques in Natural Gas Pipelines.” In *10th European Drag Reduction Working Meeting*. Berlin, Heidelberg.

Westerweel, J., and F. Scarano. 2005. “Universal Outlier Detection for PIV Data.” *Experiments in Fluids* 39 (6): 1096–1100. doi:10.1007/s00348-005-0016-6.

White, C. M., and M. G. Mungal. 2008. “Mechanics and Prediction of Turbulent Drag Reduction with Polymer Additives.” *Annual Review of Fluid Mechanics* 40 (1): 235–56. doi:10.1146/annurev.fluid.40.111406.102156.

White, C. M., V. S. R. Somandepalli, and M. G. Mungal. 2004. “The Turbulence Structure of Drag-Reduced Boundary Layer Flow.” *Experiments in Fluids* 36 (1): 62–69. doi:10.1007/s00348-003-0630-0.

Wieneke, B. 2008. “Volume Self-Calibration for 3D Particle Image Velocimetry.” *Experiments in Fluids* 45 (4): 549–56. doi:10.1007/s00348-008-0521-5.

Willert, C. 1997. “Stereoscopic Digital Particle Image Velocimetry for Application in Wind Tunnel Flows.” *Measurement Science and Technology* 8 (12): 1465–79. doi:10.1088/0957-0233/8/12/010.

Willmarth, W. W., and S. S. Lu. 1972. “Structure of the Reynolds Stress near the Wall.” *Journal of Fluid Mechanics* 55 (1): 65–92. doi:10.1017/S002211207200165X.

Woolford, B., J. Prince, D. Maynes, and B. W. Webb. 2009. “Particle Image Velocimetry Characterization of Turbulent Channel Flow with Rib Patterned Superhydrophobic Walls.” *Physics of Fluids* 21 (8). doi:10.1063/1.3213607.

Worth, N. A., T. B. Nickels, and N. Swaminathan. 2010. “A Tomographic PIV Resolution Study Based on Homogeneous Isotropic Turbulence DNS Data.” *Experiments in Fluids* 49 (3): 637–56. doi:10.1007/s00348-010-0840-1.

Yamaguchi, K., M. Sasamori, H. Mamori, K. Iwamoto, and A. Murata. 2014. “Analysis of Vortical Structure over a Sinusoidal Riblet by Dual-Plane Stereoscopic PIV.” In *17th International Symposium on Applications of Laser Techniques to Fluid Mechanics*. Lisbon.

Yan, Y. Y., N. Gao, and W. Barthlott. 2011. “Mimicking Natural Superhydrophobic Surfaces and Grasping the Wetting Process: A Review on Recent Progress in Preparing Superhydrophobic Surfaces.” *Advances in Colloid and Interface Science* 169 (2). Elsevier B.V.: 80–105. doi:10.1016/j.cis.2011.08.005.

Yang, S., S. Li, H. Tian, Qi. Wang, and N. Jiang. 2015. “Coherent Spanwise Structures in

Turbulent Boundary Layer over Drag-Reducing Riblets." *Transactions of Tianjin University* 21 (4): 317–23. doi:10.1007/s12209-015-2526-5.

Young, I. T., R. Zagers, L. J. van Vliet, J. Mullikin, F. Boddeke, and H. Netten. 1993. "Depth-of-Focus in Microscopy." In *Proceedings of the 8th Scandinavian Conference on Image Analysis*, 493–98. Tromso.